EFFECT OF HIGH TEMPERATURE EXTRUSION CONDITIONS ON THE MICROSTRUCTURE OF AA3003 ALUMINUM ALLOY

by

Lina Marcela Grajales

B.A.Sc., The University of British Columbia, 2009

A THESIS SUBMITTED IN PARTIAL FULFILLMENT OF
THE REQUIREMENTS FOR THE DEGREE OF

MASTER OF APPLIED SCIENCE

in

The Faculty of Graduate Studies

(Materials Engineering)

THE UNIVERSITY OF BRITISH COLUMBIA

(Vancouver)

April 2013

Abstract

The effect of high temperature extrusion conditions on the microstructure of AA3003 aluminum alloys has been investigated. The extrusion trials were conducted using a laboratory scale fully instrumented extrusion press at Rio Tinto Alcan's Arvida Research and Development Centre (ARDC). Direct Chill (DC) cast billets were homogenized using one of three different treatments (e.g. 8 h at 500°C, 8h at 550°C, and 24 h at 600°C) prior to extrusion. Extrusions were conducted using a range of extrusion temperatures (e.g. 350°C to 500°C), ram speeds (e.g. 2 mm/s to 32 mm/s), and extrusion ratios (e.g. 17:1 ER to 280:1 ER). This provided a full range of as-extruded microstructures from recrystallized to unrecrystallized, with a wide range of final grain sizes.

The microstructure of the extrudates was examined using optical microscopy and Electron Backscatter Microscopy (EBSD). The extrudate microstructures have been rationalized in comparison with the processing conditions from the extrusion trails. It was found that the extent of recrystallization is related to the homogenization treatment (i.e. dispersoid number density), and the ram speed (i.e. the temperature profile). It was also found that the 'unrecrystallized' deformed grain thickness could be approximated using a simple mass balance approach. The stability of 'unrecrystallized' as-extruded samples was investigated in post-extrusion annealing experiments, using a range of temperatures (e.g. 500°C to 550°C) and times (e.g. 10 min. at 550°C). It was found that most of the structures had enough stored energy to recrystallize.

In addition, high temperature compression tests were conducted using a Gleeble® 3500 Thermo-mechanical Simulator. These tests were conducted to further investigate the constituent behavior of the aluminum alloy with regards to transient strain rates. Tests were conducted at a temperature of 500°C using a constant strain of 1 s^{-1} and 10 s^{-1}, and transient strain rates. The yield stress, flow stress and work hardening were fit to a physically based flow stress model developed by Kocks and Chen. It was found that the strain rate history had an effect on the flow stress of the material, and that the model could not fully capture the behavior.

Table of Contents

List of Tables

List of Figures

Acknowledgements

This work could not have been completed without the guidance, wisdom and encouragement from a great network of supportive individuals. I would like to take this opportunity to recognize some of my mentors, colleagues, friends and family. Thank you for all you have done.

First and foremost, I would like to extend my gratitude to my supervisor, Dr. Warren J. Poole for his continued support and wealth of knowledge.

Next, I would like to extend my thanks to Dr. Nick Parson (Rio Tinto Alcan research liaison), Dr. Marry Wells (Waterloo), and Dr. Qiang Du for their guidance and direction.

Many thanks go out to the faculty and staff of the Department of Materials Engineering, in particular the machine shop staff (Ross Mcleod, Carl Ng, and David Torok), Wongsang Kim, the office staff (Fiona Webster, Mary Jansepar, and Michelle Tierney), and Jacob Kabel

I would like to recognize Annabel Geng, Hamid Azizi-alizamini, Payman Babaghorbani, Yahya Mahmoodkhani, Chenglu Liu, and Jingqi Chen for all of their support in the lab and for their participation, comments and suggestions during our aluminum group meetings. Thank you to Thomas Garcin for assisting me with the high temperature compression tests.

Next I want to thank Beth Sterling, Millie Kwan, Victor Leung, and Kevin Hsaio for their continued friendship and emotional support.

To my Mom, Dad, Laura, Adriana, Steve, and the Fabris Family thank you for your encouragement and love. Sean, thank you for everything you have done for me and continue to do. Your support means so much to me.

Lastly, I would also like to thank Rio Tinto Alcan and NSERC Canada for their contributions.

Thank you all!

To my family

1 Introduction

There is significant interest in the microstructural development of AA3xxx aluminum alloys during extrusion. AA3xxx alloys are important commercial alloys containing manganese, iron and silicon as the main alloy additions. These alloys are widely used in the automotive market for heat exchanger tubing [1] [2]. One of the key requirements for heat exchanger tubing is a fine equiaxed grain size; which provides good strength and ductility. A main challenge for the industry has been producing the fine grain structure at the highest possible productivity [2]. Alloys such as AA3003 undergo a process route that includes Direct Chill casting, homogenization, extrusion and brazing (Figure 1.1). One of the main goals of such manufacturing operations is to be able to tailor process parameters such that the desired material properties can be designed. Therefore, the ability to control deformation conditions allows for the design of the microstructure so that the material microstructure properties can be tailored to the final component. This is leading many aluminum producers to push for through process modeling. This study is a part of a larger project to develop a through process model for the processing of aluminum heat exchangers [3]. These models look to characterize the microstructure evolution of the alloy during the thermo-mechanical process as every step of the process impacts the microstructure and mechanical properties of the end product. In this study the process steps from homogenization to extrusion are examined.
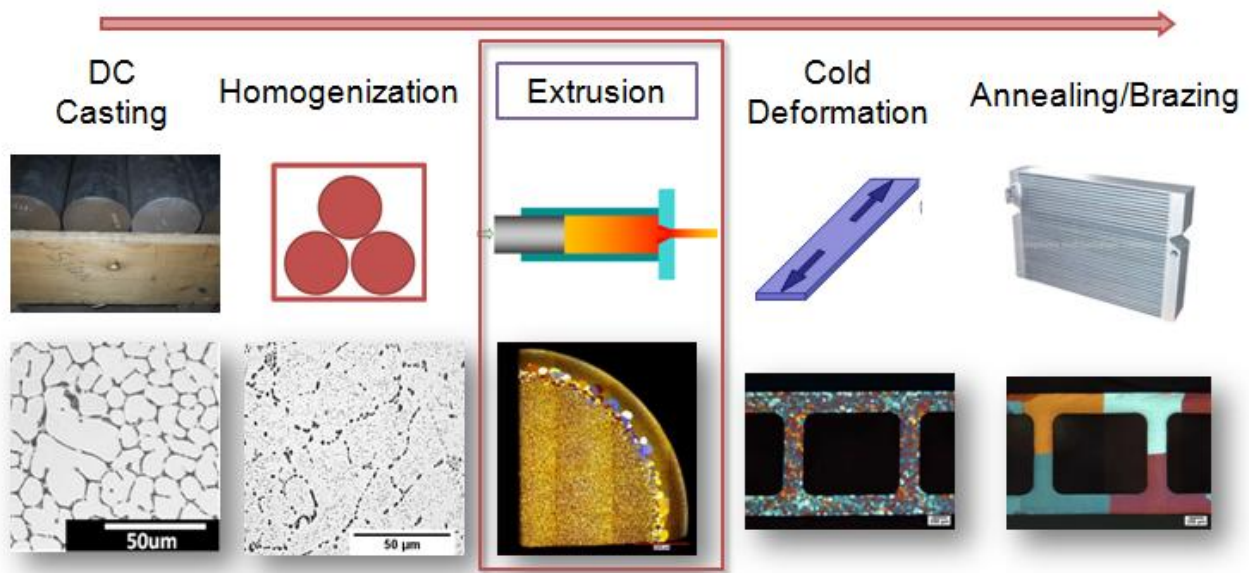
Figure 1.1 – Industrial manufacturing process of AA3xxx for heat exchanger application. (Figure produced using some images from [3] [4] [5]).

1.1 Homogenization

As-cast billets are homogenized to decrease the extrusion pressures, improve the surface quality of the extrudate, reduce micro-segregation introduced during casting and decrease the die bearing and exit temperatures [2] [5]. The homogenization treatment is typically conducted as a 3 step process which includes heating, soaking (i.e. holding), and cooling. For typical industrial homogenization treatments the heating rate is conducted at a rate of 50 to 250°C/hr [6] to the soak temperature. The billet is then held at the soak temperature for several hours and then cooled to room temperature. During heating the as-cast microstructure evolves, with the morphology of the constituent particles changing and the precipitation of a fine precipitate phase, termed dispersoids. The composition of these manganese rich precipitates has been determined to be $Al_6(Mn,Fe)$ and α-$Al(Mn,Fe)Si$ [7] [4] [8] [9] [10]. The number density of the dispersoids, in the as-homogenized state, has been related to the homogenization treatment (i.e. combination of soak temperature and soak time). A longer soak temperature at higher temperatures results in a low dispersoid number density while a shorter soak at a lower temperature results in a high dispersoid number density [11].

1.2 Extrusion

Extrusion is a thermo-mechanical process in which pressure is applied to the back of a billet, by a ram, causing it to upset and deform as it exits through the die (Figure 1.2). Direct non-lubricated hot extrusion was used for this study to produce rods of various diameters.

Prior to extrusion the homogenized billets are rapidly heated (50 - 60 s) in an induction furnace to the extrusion temperature [2]. The billet is then placed in the heated extruder container along with a dummy block. As the ram starts to exert force on the billet, the billet starts to deform by first filling the volume of the container by increasing in size radially and decreasing in size laterally (i.e. upset). After upset the force needed to extrude the material increases -this is termed the breakthrough pressure. The material that flows through the die is water quenched and then air cooled down to room temperature.
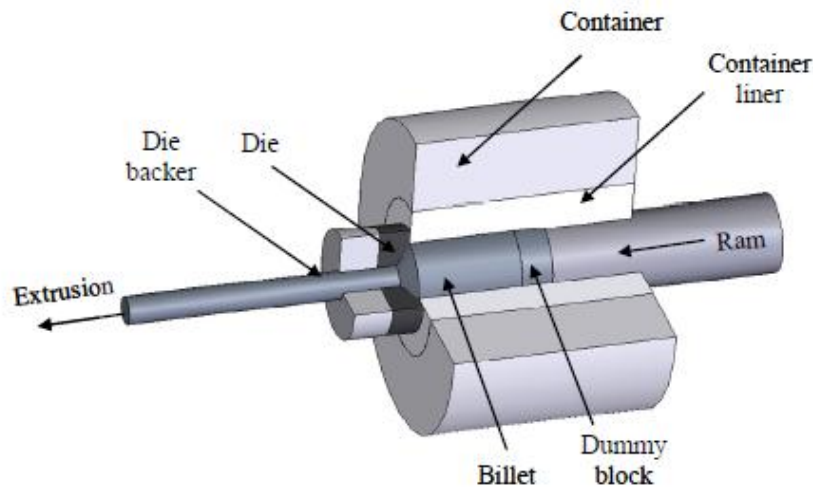
Figure 1.2 – Internal component of a typical direct extrusion press. Reproduced with the permission of Kubiak [5].

During extrusion the centre of the extrudate and the surface undergo different strain rate and temperature histories. The surface layer of the extrudate undergoes more severe deformation and experiences higher temperatures (due to temperature generated during extrusion from the friction between the billet and the die) [12]. As a result there is a through-thickness (i.e. centre to surface) variation in the as-extruded microstructure.

1.3   Project Objective

Previous and current work on the through process model being developed in conjunction by Rio Tinto Alcan, the Materials Engineering department at the University of British Columbia and the Mechanical Engineering department at the University of Waterloo, for the processing of AA3xxx aluminum alloys for heat exchanger applications has consisted of:

- a solidification and homogenization model developed by Du et al. [13],
- a constitutive model to describe the steady-state flow stress during high temperature compression for AA3xxx by Kubiak [5],
- process microstructure characterization of extrudates by Geng [4],
- an FEM model for simulation of extrusion and microstructural predictions by Mahmoodkhani et al. [12] [14],
- and the recrystallization kinetics for cold worked extrudates and the influence of the initial microstructure on the recrystallization behaviour by Babaghorbani et al. [15].

The high temperature extrusion of AA3xxx aluminum alloys has proved to be another complicated piece of the puzzle with many variables affecting the as-extruded microstructure. This study looks to help to fill some of the gaps in the knowledge required to build an increasingly robust through process model by i) providing new insight regarding the effect of the extrusion process conditions on the microstructure and ii) providing experimental data for the validation of the FEM model being developed by Mahmoodkhani et al. [14]. Therefore some of the objectives of this study are then to quantify the deformed state of the microstructure of AA3003 during high temperature extrusion using standard metallographic techniques and to investigate the stability of unrecrystallized as-extruded microstructures. To meet the proposed objectives this study focuses on the characterization of the as-cast, as-extruded, and post-extrusion annealed samples. This study also continues work on a physically based flow stress model previously investigated by Kubiak [5] [11] and Geng [4], using data from high temperature compression tests, to study the constitutive behavior of AA3xxx aluminum alloys where transient deformation is considered, i.e. conditions found during industrial extrusion.

Chapter 2 provides a summary of some of the literature available on the as-cast microstructure, homogenized microstructure and high temperature deformation of AA3xxx aluminum alloys, with specifics to AA3003. Chapter 3 describes the scope and objectives of this study and Chapter 4 provides details on the experimental methodology used for i) the characterization of the microstructure in the as-cast and as-extruded states, ii) the post-extrusion annealing tests and iii) the high temperature compression tests. Chapter 5 and 6 present the results and discussion of the study, respectively. Chapter 7 provides a summary of the findings of the study and some recommendations for future work.

2 Literature Review

3xxx aluminum alloys are widely used in the automotive, construction and beverage container markets [1]. A market with large potential growth for aluminum alloys is expected to be in the automotive industry due to emissions and fuel economy targets set by government. Lightweighting is expected to play an important role in achieving these targets as a 5.5% decrease in fuel consumption can be obtained for a corresponding weight reduction of 10% [1]. The average aluminum content in motor vehicles, manufactured in the United States, has risen from 8 kg in 1947, 90 kg in 1994 to 130 kg in 2004 and is continuously growing [1]. More specifically AA3003 aluminum alloys are being used for heat exchanger applications [16] due to their favourable cost and performance compared to copper which has been traditionally used. The ideal materials for heat exchangers have a high thermal conductivity, moderate yield strength [17] and are highly corrosion resistant. The yield strength and corrosion behavior are strongly dependent on microstructure. Hence, there is significant interest in the microstructural development of AA3003 aluminum alloys during extrusion as these products are widely used in heat exchanger applications.

The following chapter provides a review of i) AA3xxx alloys with an emphasis on AA3003 (i.e. the alloy used in the investigation), ii) the process steps taken, from homogenization to extrusion, to produce extruded aluminum, iii) the relevant metallurgical processes such as the evolution of constituent particles and dispersoids during homogenization,

the deformation of grains during extrusion and the stability of the as-extruded microstructure and finally iv) the constitutive behavior of AA3003 during high temperature deformation.

2.1 A Brief Review of AA3xxx Aluminum Alloys

AA3xxx contains manganese (Mn), iron (Fe) and silicon (Si) as alloying additions. Commercial non-heat treatable AA3xxx aluminum alloys have the following composition range of 0.3 – 1.5 wt% Mn, 0.1 – 0.7 wt% Fe, 0.1- 0.6 wt% Si, 0.05 – 0.30 wt% Cu, 0.1 wt% Ti and may contain other additions such as Mg, Cr and Zn [1] [18]. These alloys are considered as non-heat treatable alloys since their mechanical properties do not change significantly with heat treatment even though we shall see that precipitation does occur during processing [19] [20]. In general the strength of these alloys is quite low (yield stress of 20 - 60 MPa), although Mn can be effective at solid solution strengthening [21]. The non-heat treatable alloy AA3003 is considered to have a good combination of workability, corrosion resistance and a high melting point, which allows it to be easily deep drawn, extruded, and brazed [19] [21] [2] [7], i.e. a good choice for automotive radiators and air conditioners.

Iron and silicon have very low solubility in aluminum. The reason for the Fe alloy addition is due to the role that the Fe intermetallics play in promoting a fine recrystallized grain size after cold drawing and annealing [2]. The solid solubility for Fe at 655°C is 0.05 wt% [1] and less than 5×10^{-10} wt% at 20°C (calculated using ThermoCalc software with TTAl6 database). The solid solubility for Si is 1.65 wt% and less than 0.1 wt% at 577°C and 20°C, respectively [1] [20] [22]. When Mn is present as an alloying element along with Fe and Si, the solid solubility of Mn decreases, as they form the complex quaternary-phase Al-Fe-Mn-Si (e.g. $Al_{12}(Fe,Mn)_3Si$, $Al_{15}(Fe,Mn)_3Si_2$, α-Al(Fe,Mn)Si) [20] [23].

2.2 AA3xxx As-cast Microstructure

AA3xxx alloys used for extruded products are usually cast into extrusion billets using Direct Chill casting (DC casting). DC casting is a semi-continuous process, in which solidification is accomplished in two stages. The first is the formation of solid metal at the chilled mould wall, and second is the solidification of the remainder of the billet cross-section by the removal of heat by spray cooling [1]. A faster solidification rate and inoculation with Ti grain refiners (TiB_2) results in relatively fine as cast grain structure of 50 - 150 μm and a primary aluminum dendrite arm spacing 5 - 20 μm [23], with several percent of inter-granular second phases known as constituent particles. The constituent particles (~1 to 5 μm) have been identified as a mix of $Al_6(Mn,Fe)$ and α-Al(Mn,Fe)Si [13]. An example of the as-cast

7

microstructure for AA3003 taken from the Master's thesis of Geng [4] is shown in Figure 2.1. In this case the grain size through the cross-section of the billet (diameter of 101.6 mm) was found to be relatively consistent, although a thin layer of grains on the surface was observed due to inverse segregation [4]. However, at the grain level, the micro-scale composition is inhomogeneous. The dendrites have cored structure from solidification and are supersaturated in the alloying additions, particularly Mn. The as-cast materials are considered to have a high degree of micro-segregation [24].
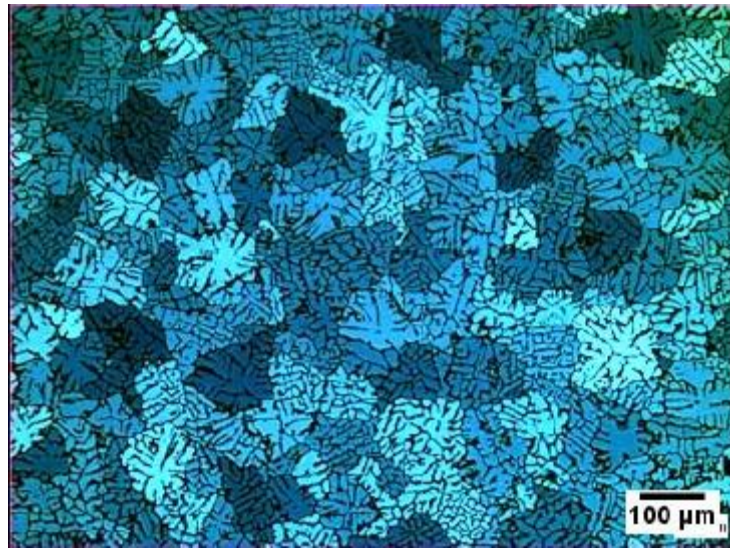
Figure 2.1 - Optical micrograph of anodized as-cast AA3003. Reproduced with permission from Geng [4].

2.3 AA3003 Homogenized Microstructure

Cast billets typically undergo a homogenization heat treatment before extrusion for a variety of reasons. Some of the reasons are related to the microstructure while others are related to commercial concerns. There is a balance between the final desired microstructure and the throughput required for profitability (i.e. time and energy considerations). The following are some of the reasons why homogenization treatments are employed [2] [5]:

- Reduce micro-segregation.
- Lower the break through pressure.
- Decrease the die and exit temperatures.

Homogenization for AA3003 has been conducted at temperature ranging from 400°C to 630°C using soak times of 4 h to 24 h [21] [2] [4] [11]. Typical industrial homogenization heating rates are in the range of 50 to 250°C/hr [6]. The decrease in the break through pressure in homogenized billets has been associated with a decrease in the level of Mn in solid solution, as the Mn is precipitated as dispersoids or diffuses to constituent particles[2]. For example, comparing two 101.6 mm diameter billets, one as-cast and one homogenized for 8 h at 550°C. The billets are extruded at a temperature of 400°C, using a ram speed of 14 mm/s. The as-cast billet requires an extrusion force of approximately 5.4 MN and the homogenized billet requires a force of approximately 4.6 MN [5] [11]. The difference was attributed to the amount of Mn is solid solution after the homogenization treatment. A lower break through force allows for an increase in throughput as the ram speed can be increased. The decrease in the break through force pressure also leads to a decrease in the exit temperature of the extrudate. This helps to improve the surface quality of the extrudate as high exit temperatures have been found to correlate with poor surface quality -such as high roughness, die lines and pick-ups [2] [25].

The phase transformations in the AA3xxx alloy system which occur during the heating, soaking and cooling segments of the homogenization treatment have been investigated by a number of authors, see references [2] [7] [4] [5] [12] [14] [8] [9] [26] [27] [28]. Along with experimental investigations a number of attempts have been made to ([7] [13] [29] [30] [31]) model the transformations occurring during homogenization. The goal of all has been to gain a deeper understanding of the evolution of the constituent particles and the formation/dissolution of dispersoids as these affect the subsequent recrystallization behavior, texture, grain size, and mechanical properties of the extrudate [8] [26]. The dispersoid particles are partially coherent with the Al matrix [9] [26] and their transformation during homogenization is complex and chemistry dependent (i.e. particularly to the Si level). The transformation has been described as going from $Al_6(Mn,Fe)$ plus Si to an α-Al(Mn,Fe)Si phase (various stoichiometries have been reported) and Al [9] [27] [29].

Furthermore, there is a significant change in the morphology of the constituent particles. These changes start occurring during the ramp when the temperature reaches approximately 300 to 400°C, when the eutectic structure begins to break-up. Furthermore, starting at a temperature of 300°C some of the $Al_6(Mn,Fe)$ phase may begin to transform to α-Al(Mn,Fe)Si [7] [4] [8] [9] [10] (depending on the Si content), and the precipitation of Mn rich dispersoids ($Al_6(Mn,Fe)$ or α-Al(Mn,Fe)Si) is initiated in the primary aluminum dendrites. Precipitation of dispersoids has been found to begin at Mn-rich areas, with nucleation occurring on dislocations and subgrain boundaries [9]. As the temperature increases, the number density of dispersoids and the Mn solid solubility both increase. The number density of dispersoids reaches a maximum at approximately 470°C [13]. As the temperature continues to increases, the dispersoids begin to dissolve back into the matrix (at approximately 530°C) since the

equilibrium solubility of Mn increases with temperature. However, at this point the rate of Mn diffusion increases to a level where long range diffusion of Mn from the Mn-rich zones to the Fe-rich constituent particles starts to occur [9].

During the soak spheriodization of constituent particles occurs and the ratio of α-Al(Mn,Fe)Si to Al_6(Mn,Fe) increases with time, depending on the Si wt% in the alloy [8]. At a temperature of 560°C the constituent particles start to break-up into smaller particles [4] [27]. As the soaking time progresses the constituent particles spheriodize and coarsen, resulting in a decrease in the number density of constituent particles [8]. The corresponding change in Mn and Fe in solid solution, especially within the first hour of the soak, is due to the rapid dissolution of fine dispersoids [4] [8]. Kubiak [5] reported that the number density of dispersoids decreased with an increase in soaking temperature and soaking time (Figure 2.2). Kubiak [5] and Geng [4] reported the highest number density of dispersoids for a treatment of 8 h at 500°C, and few to no dispersoids after a homogenization treatment of 24 h at 600° (Figure 2.2).
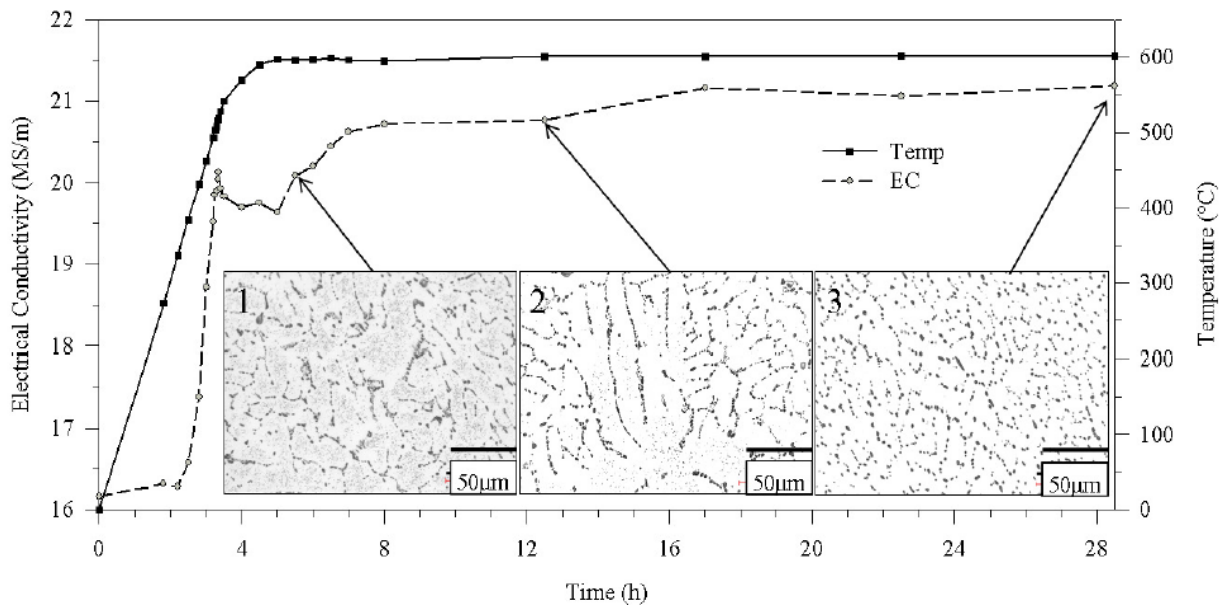
Figure 2.2 – AA3003 conductivity curve for a 600°C homogenization. Microstructure at: (1) 1 h, (2) 8 h, and (3) 24 h soak times. Reproduced with permission from [5]. (EC = Electrical conductivity)

Geng [4] conducted an analysis on the composition of the constituent particles in the same AA3003 alloy (1.27wt%Mn, 0.54wt%Fe, 0.10wt%Si) used in this work. Geng found from EDX results and due to the low concentration of Si present in this alloy that the dominant composition of constituent particles found in the system is Al_6(Mn,Fe).

Depending on the homogenization treatment (i.e. temperature and soak time) various spatial distribution of dispersoids can be produced. At a temperature of approximately 470°C, dispersoids are not uniformly distributed, but have a high density near the interdendritic regions. At higher soaking temperatures (e.g. 600°C) the dispersoids near the interdendritic regions disappear creating areas free of dispersoids. These are often referred to as either precipitate free zones (PFZ) or dispersoid free zones (DFZ) and can be found within the interior of the dendrites [7] [13]. Further increase in the temperature results in a decrease in size of the PFZ as the dispersoids number density and volume fraction increase. Prolonged soaking (e.g. 24 h) allows for an increase in size of the PFZ, as enough time is allowed for long-range diffusion of Mn and Fe and thereby complete dissolution of the dispersoids [7] [9].

2.4   Electrical Conductivity and Resistivity

Previous work by Kubiak [5], Geng [4], and Li et al. [8] has tracked the evolution of the structure of AA3xxx, during homogenization and extrusion, through electrical conductivity (conductivity). Eddy current inspection is a non-destructive test based on the principles of electromagnetic induction [32] and is often used to differentiate physical, structural and metallurgical conditions. The inspection method is extremely versatile and effective but should be used with caution as it is sensitive to many inherent material properties and characteristics, such as voids, inclusions, grain size, and solid solubility [32] [33].

Conductivity data and optical micrographs have been used in the past to evaluate the solid solution content in an alloy, and thereby determine the degree of precipitation. Figure 2.2, from Kubiak, shows the plot of temperature and conductivity versus treatment time. Due to the low amounts of Fe (0.54 wt%) and Si (0.1 wt%) in the alloy, the evolution of electrical conductivity is often taken only as the Mn (1.27 wt%) variation in solid solution [5] [8]. The conductivity increases during the ramp-up can be linked to a decrease in the solid solution of Mn. With the largest increase occurring after 300°C, when the Mn in the supersaturated solid solution starts to precipitate, and a local maximum occurring at around 450°C to 560°C (depending on the composition) [5] [8]. This peak is an indication of a shift in the solid solubility of the system, as it increases as temperature increases. This increase in solid solubility results in the dissolution of some of the previously precipitated dispersoids and a drop in the conductivity at the beginning of the soak. As the soak time progresses (1 h to 24 h) the conductivity slowly increases until it levels out. This increase has been attributed to Mn precipitation during the soak [5].

The contributions to the resistivity of a material have often been taken into account using Matthiessen's rule (equation (2.1)), where the total electrical resistivity of a metal is equal to the sum of the contributions from temperature (ρ_t), impurities (ρ_i), and deformation (ρ_d) [34].

$$\rho_{Total} = \rho_t + \rho_i + \rho_d$$

(2.1)

The dependence of the temperature component of the resistivity increases with temperature as thermal vibrations and lattice irregularities such as vacancies serve as electron-scattering centers. The influence of the alloying elements is related to the alloy concentration and the contributions for each alloy can be added using the rule-of-mixtures. The resistivity of aluminum at room temperature is approximately 26.5 nΩm [22] [34] [35]. Hatch has reported the resistivity contributions by Mn to resistivity as 29.4 nΩm and 3.4 nΩm per wt % in solution and out of solution, respectively [22] or alternatively 31.1 nΩm per wt% from Lok [35]. The amount of plastic deformation increases the resistivity as a result of an increase in the number of electron-scattering dislocations. The contribution to the resistivity from deformation is often ignored as its influence is much weaker than that of increasing temperature or alloying content [34].

2.5   Deformation Conditions During High Temperature Extrusion

The deformation conditions during high temperature extrusion are extreme (i.e. high temperatures and high strain rates) and inhomogeneous. Strain rates vary in the range of 0.001 s^{-1} to 60 s^{-1}, and surface strains can be more than 10 times greater than at the centre line [12] [36] [37]. During the high temperature extrusion, inhomogeneity of deformation can result from redundant deformation and the effects of friction at the extrudate/die wall interface [14]. This can lead to significant through profile effects in the extrudate. These effects can manifest in significant microstructure inhomogeneity. The extrudate may recrystallize to different extents through the profile, i.e. the centre may be unrecrystallized while the surface may have fully recrystallized [12] [36] [38].

In aluminum the plastic deformation behavior is controlled by different mechanisms [39]: low-temperature plasticity by dislocation glide, power-law creep by dislocation glide or glide-plus climb, or diffusional flow. More than one of these mechanisms can control the deformation, but there is usually one dominant mechanism. Typically the dominant mechanism is tied to the stress, strain rate and temperature [39]. In order to model the thermo-mechanical process experienced by the material it is necessary to determine the deformation mechanisms taking place and the stability of the microstructure after undergoing high temperature

deformation. It is important to characterize the deformation state (i.e. dislocation density, arrangement of dislocations, grain shape and nuclei for recrystallization) and the restorative mechanisms involved (i.e. recovery and recrystallization).

2.6 Microstructure Evolution

The recrystallization behavior of extruded aluminum is complicated, and the detailed mechanisms have been debated for a long time. This has centered around static/dynamic recrystallization and continuous/discontinuous recrystallization [40]. Recrystallization can also be impeded by small particles such as dispersoids. This section will cover restorative mechanisms (e.g. recovery and recrystallization) and geometric dynamic recrystallization, followed by Zener pinning, and post-extrusion annealing.

2.6.1 Restorative Mechanisms

Changes in the microstructure of aluminum alloys (and other metals) occur during and after the process of high temperature deformation (e.g. extrusion). Recovery and recrystallization are two competing restorative (softening) mechanisms in deformed materials driven by the stored energy of the deformed state [40]. Recovery usually involves a partial restoration of the material properties as the dislocation structure is not completely removed, but instead reaches a metastable state. Recrystallization may occur within the deformed or recovered structure and is characterized by the formation of new, low dislocation density grains [40]. The new grains then grow and consume old grains; achieving a new structure with a low dislocation density. Both phenomena are competitive, with complete recrystallization eliminating recovery from occurring, and the presence of recovery lowering the driving force for recrystallization.

Recrystallization may occur as a discontinuous or continuous process. Discontinuous (or heterogeneous) is used to describe processes that have nucleation and growth stages while continuous (or uniform) is used to describe processes in which the microstructures evolve gradually with no identifiable nucleation and growth stages. The 'continuous' description is extended to include recovery by subgrain growth, continuous recrystallization and normal grain growth and 'discontinuous' to include discontinuous subgrain growth and primary recrystallization [40]. If the restorative mechanisms occur during deformation at high temperatures, such as in high temperature extrusion, they are called dynamic recovery and dynamic recrystallization. In extrusion these mechanisms play an important role as they affect the flow stress, texture and grain size of the deformed material [41].

Recovery:

Recovery occurs prior to recrystallization, in any crystal with high non-equilibrium concentrations of point or line defects, and may occur during the deformation as dynamic recovery [40]. The steps in recovery typically involve the following: cell formation, annihilation of dislocations within cells, subgrain formation and subgrain growth. Evidence of recovery is rarely observed by optical microscopy as the microstructural changes in the material are subtle and occur on a small scale. This is why recovery is typically measured indirectly through physical (e.g. Electrical resistivity) changes, mechanical property (e.g. yield stress or hardness) changes or through the use of higher resolution microscopy. Annihilation of dislocations and the rearrangement of dislocations are two of the primary processes that result in lower energy configurations of a recovered system [40] [42]. The annihilation of dislocations during recovery may be inhibited by the presence of constituent particles and dispersoids as they may pin individual dislocations and may limit the subgrain size [40]. Dynamic recovery during deformation at high temperatures is rapid in aluminum alloys as the high stacking fault energy of the material allows for easy dislocation climb and cross-slip. At high enough temperatures, the annihilation and dislocation accumulation processes (which are responsible for work hardening at lower temperatures) can reach a dynamic equilibrium resulting in a steady-state flow stress being obtained [40].

Recrystallization:

Static recrystallization has been found to occur when subsequent annealing is conducted after high temperature deformation. In static recrystallization strain-free grains grow and "consume" deformed grains [40]. Recrystallization of the annealed structure is dependent on the stored energy of the deformed material. Where the stored energy (assumed to come from dislocation accumulation during deformation) is often defined as shown in equation (2.2) [40], where α is a constant of order of 0.5, ρ is the dislocation density, G is the shear modulus, and b is the magnitude of the Burger's vector. This is one of the simplest approaches as other approaches for determining the stored energy include subgrain size and subgrain misorientation.

$$E_{\perp} = \alpha \rho G b^2 \tag{2.2}$$

Dynamic recrystallization in not a well understood recovery mechanisms due to its complexity and difficulty to separate and analyze. It is believed to be similar to static recrystallization. Dynamic recrystallization is a restorative mechanism which occurs during

plastic deformation (e.g. during high temperature deformation) [40] [43] [44]. Both nucleation and growth take place during deformation in dynamic recrystallization. Softening of the material during high temperature deformation has been attributed to dynamic recrystallization [45]. Aluminum's high stacking fault energy leads the system to favor dislocation annihilation, dynamic recovery and subgrain formation [40]. Nevertheless, many have hypothesized that dynamic recrystallization occurs in aluminum under large strains (>3) and elevated temperatures [44] [45] [46].

Continuous dynamic recrystallization is promoted by an increase in the grain boundary area, as in large strain deformations at low and high temperatures [44]. Therefore the extent of deformation has an effect on recrystallization, with regards to the dislocation density and distribution and size of second phase particles. The later may increase the driving pressure for recrystallization. The state of the deformed structure determines whether or not particle-stimulated nucleation (PSN) of recrystallization is possible [40]. If PSN is possible recrystallization is found to originate at pre-existing subgrains, with nucleation occurring by rapid sub-boundary migration. The grain may then stop growing once the deformation zone is consumed. In general second phase particles may increase the stored energy and increase the driving pressure for recrystallization. Larger particles can act as nucleation sites and if the particles are closely spaced they may exert a pinning effect on grain boundaries. The increase in stored energy and the increase in nucleation sites, both help promote recrystallization, while the finely-dispersed particles inhibit recrystallization. Therefore the recrystallization behavior is closely tied to the microstructure [40].

The acceleration of recrystallization can be attributed to increased driving pressure from dislocations generated during deformation and PSN. This acceleration of recrystallization is not common in aluminum alloys with small particles possibly due to the large amount of dynamic recovery that occurs in most aluminum alloys, which removes many of the geometrically necessary dislocations created at the particles [40].

If a material is deformed to large strains at elevated temperatures, the resultant structure is one consisting predominantly of high angle grain boundaries (HAGBs) [44]. This type of structure then evolves to a fine-grained microstructure consisting mainly of high angle boundaries. This microstructure is similar to one resulting from conventional recrystallization (i.e. nucleation and growth). This microstructure evolves homogeneously and is therefore classified as continuous recrystallization and more specifically referred to as geometric dynamic recrystallization [40] [44]. This will be discussed in further detail in the next section.

2.6.2   Geometric Dynamic Recrystallization

Geometric dynamic recrystallization (GDRX) has been reported in studies on high temperature deformation of aluminum alloys deformed to large strains [14] [36] [40] [44] [45].

The occurrence of GDRX is both dependent on the original grain size and the deformation conditions [41]. During dynamic recovery grain boundaries develop serrations with a wavelength similar to that of the subgrain size. When the structure is deformed and the grains become flattened the fraction of HAGBs increases with increasing strain [44], until the size of the boundary serrations become comparable to the grain thickness. This is followed by interpenetration of the scalloped boundaries resulting in a microstructure of small equiaxed grains equivalent in size to the subgrain structure. This type of equiaxed microstructure evolves without the nucleation of new grains, making it different from discontinuous dynamic recrystallization. Another difference between GDRX and discontinuous recrystallization is the resultant crystallographic texture. When discontinuous recrystallization has occurred the final texture is often very different from the deformation texture, where as with GDRX there is little change in the texture as the HAGB migration is minimal. This is why GDRX is more closely associated with continuous recrystallization. Sweet et al. [38] and Van Geertruyden et al. [36] have reported the presence of a fine-grained microstructure near the surface of the extrudate, where the temperature and strain rate are higher, believed to be formed by GDRX. These HAGB structures may undergo continuous recrystallization on annealing [40].

2.6.3   Zener Pinning

The dispersoid particles present in the microstructure exert a retarding force on low and high angle grain boundaries. The exerted force on the grain boundary may have an effect on the restorative mechanisms (i.e. recovery, recrystallization and grain growth). This is known as Zener pinning (or Zener drag), and the extent of the effect depends on the nature of the particle and interface interaction, the shape, size, spacing and volume fraction of the particles [40] [47]. The distribution also plays a role on the force imposed on the boundary [47]. Zenner pinning pressure (P_Z) is often expressed as shown in equation (2.3) [40], where γ_{gb}, F_V and r represent the grain boundary energy, the precipitate volume fraction and the average precipitate radius, respectively.

$$P_Z = \frac{3\gamma_{gb}F_V}{2r} \tag{2.3}$$

As the volume fraction increases and the radius of the particles increases, there is a certain Fv/r ratio in which the Zener pinning pressure is at a maximum; therefore recrystallization growth is suppressed when *Fv/r* is greater than a critical value [40], and as a result Zener pinning has been found to play a major role in retarding discontinuous recrystallization [46] [47].

Recrystallization will only occur when there is a positive driving pressure for recrystallization (P), this balance is often expressed as a combination of equation (2.2) and (2.3) (equation (2.4)) [40].

$$P = E_\perp - P_Z = \alpha\rho Gb^2 - \frac{3\gamma_{gb}F_V}{2r} \tag{2.4}$$

where $E_\perp$ is the energy of dislocation line length per unit volume of material.

2.7 Characterization of the Microstructure

The simplest microstructural feature that is used to characterize the deformed state is the grain shape. Information on the grain and subgrain structures is important as grain size strongly affects the mechanical properties and influences the physical properties, surface properties, phase transformation and annealing behavior [48]. When deformed, the grains of polycrystalline metals change in manner that corresponds to the macroscopic shape change [40]. Electron Backscatter Diffraction (EBSD) measurements can provide data on highly deformed polycrystalline materials, if the boundaries and not the dislocations are of primary interest, with a high degree of statistical reliability [41] [49]. The grain size has traditionally been measured by optical microscopy but the characterization of grain size and related parameters is difficult on highly deformed structures. Transmission electron microscopy (TEM) has also been used to gain information on the smallest grain size and subgrain structures, although the sample preparation is difficult, and the volume that can be studied is small [40].

The use of EBSD in the characterization of highly deformed grain and subgrain structures is increasing. The main advantage being that dimensional information may be correlated with orientation data [48]. Two methods used for characterizing the microstructure are the linear intercept method and the grain reconstruction method. Both techniques require that the sample be tilted by 70° to the optic axis, caution must be taken to make sure that the sample alignment is accurate. The other parameters which affect the quantity and quality of the data are the material, pattern acquisition time, effective spatial resolution and relative angular [40] [48]. The most significant error is the incorrect alignment of the sample. If the top surface of the specimen is incorrectly aligned to the horizontal about the tilt axis the specimen tilt during the scan is no longer 70°. This results in large errors for small misalignments. A misalignment of 1° and 5° correspond to an error of 5% and 35%, respectively [40].

2.8 Constitutive Model

During high temperature processing, aluminum is subjected to a wide range of strains and temperature [50]. There is a need to characterize the material's response over such a range. Many approaches have been applied to aluminum alloys for the prediction of yield stress and steady-state flow stress within a set temperature and strain rate regime. Simple empirical approaches and physically based approaches have been proposed in the literature. The following provides a review of the relevant approaches for AA3xxx.

2.8.1 Empirical Constitutive Models

A popular model is the Zener-Holloman equation. This is because it is convenient and has been applied to various aluminum alloys [51] [52] (e.g. AA356, AA107 [53], AA2024, AA5083, AA6061, AA7050 [54] and AA7075). The Zener-Holloman equation uses the Arrhenius rate law to incorporate the plastic strain as a rate process. The Zener-Holloman parameter and an exponential-type equation are often expressed as shown in equations (2.5) to (2.7).

$$Z = \dot{\varepsilon} \, exp \left(\frac{Q}{RT}\right) \tag{2.5}$$

$$\dot{\varepsilon} = A_1 f(\sigma) \, exp \left(\frac{Q}{RT}\right) \tag{2.6}$$

where,

$$f(\sigma) = \begin{cases} \sigma^{n'} & \alpha\sigma < 0.8 \\ exp(\beta\sigma) & \alpha\sigma > 1.2 \\ [\sinh(\alpha\sigma)]^n & for \; all \; \sigma \end{cases} \tag{2.7}$$

and σ is the flow stress, T is the temperature, R is the gas constant, Q is the deformation activation energy and A_1, n', n, β and α ($\alpha = \beta/n'$) are material constants. The Zener-Holloman has good applicability at high temperatures and takes into account strain rate and temperature effects. A disadvantage to the Zener-Holloman is that it does not take into account the microstructure or work hardening of the material.

The Hardening-Sellars-Tegart (HST) equation is a combined Sellars-Tegart (or Garofalo) and hardening law approach [55] that extends the temperature range in which the Sellars-Tegart equation could be applied. The Sellars-Tegart equation uses parameters which are independent of temperature, along with the Zener-Hollomon parameter to describe the steady-state deformation behavior of materials at elevated temperatures [52] [55]. It is applicable to

high deformation temperatures (400°C to 600°C) where no strain hardening occurs. The Sellars-Tegart equation is given in equation (2.8).

$$\dot{\varepsilon} = A_i \left[sinh \left(\frac{\sigma_{flow}}{\sigma_o} \right) \right]^n exp \left(-\frac{Q}{RT} \right) \tag{2.8}$$

where A_i, σ_o and n are material constants, σ_{flow} is the steady-state flow stress, Q is the activation energy, R is the gas constant, and T is the deformation temperature. The parameters are independent of temperature. The HST is often described as the combination of the following 3 equations [55]. Equation (2.9), uses σ_H instead of σ_{flow} along with a simple hardening law to extend the validity of the Sellars-Tegart equation to lower temperatures.

$$\sigma_H = (\sigma_o + k \sqrt{\alpha_1(T)\varepsilon}) \cdot f(Z) \tag{2.9}$$

Where k is a constant, and α_1 is a hardening parameter, and the function $f(Z)$ is defined shown in equation (2.10).

$$f(Z) = min \left(1, arcsinh \left(\left(\frac{Z}{A_1} \right)^{m_H} \right) \right) \tag{2.10}$$

where Z is the Zener-Holloman parameter (equation (2.5)), A_1 is a material constant and m_H is the inverse of the stress exponent (n). The last part of the HST equation corresponds to the hardening parameter, α_1, which represents the percentage of hardening occurring at a specific temperature compared to the hardening at room temperature, under the same load. At temperatures between 250°C to 400°C, α_1 changes from 1 to 0. Equation (2.11) provides a smooth transition between hardening dominated behavior to steady-state behavior, by describing the temperature dependence of the hardening parameter.

$$\alpha_1 = \frac{1}{1 + exp(a_1 + a_2 T)} \tag{2.11}$$

where a_1 and a_2 are fitting parameters.

The HST is able to predict constitutive behavior from room temperature all the way up to the solidus temperature. Disadvantages of the HST are that it has difficulty describing a regime of intermediate temperature in which the material experiences strain hardening and strain rate dependence and it does not incorporate knowledge of the microstructure.

2.8.2 Physically-Based Constitutive Model

Kocks and Chen's physically based constitutive model aims to predict the yield stress and steady-state flow stress of a system in temperature and strain rate regimes where the solute drag mechanism dominates. The Kocks and Chen model has been used on compression tests for AA5182 and AA3xxx conducted in a temperature range of 200°C to 600°C using a strain rate of 0.001 s^{-1} to 1 s^{-1} [11] [56]. The Kocks and Chen model has been applied to conditions with no work-hardening ("Class A"), indicating a regime where solute drag mechanism dominates [56] [57]. The stress exponent found using the model describes the dominant deformation mechanism, for which the stress exponent was found to be approximately 3, in work by [56]. In general the model may be used to study the stress-strain response of a material, as well as the effects of temperature, strain rate and homogenization [11].

Kocks and Chen's kinetic law, equation (2.12), captures the temperature and strain rate dependence of a material's flow stress [56]:

$$\dot{\varepsilon} = A \left(\frac{\sigma}{\mu}\right)^n \frac{\mu b^3}{kT} exp\left(-\frac{Q_D}{RT}\right) \qquad (2.12)$$

where A is a pre-exponential constant, σ is the applied stress, μ is the temperature dependent shear modulus, n is the stress exponent, b is the magnitude of the temperature dependent Burger's vector, k is the Boltzmann's constant, T is the deformation temperature, Q_D is the activation energy for diffusion, and R is the gas constant.

Work by Kubiak et al. [11], on AA3003, has shown limitations to the applicability of the Kock's and Chen kinetic law at low deformation temperatures (e.g. 400°C) and high strain rates (e.g. 1 s^{-1}). Figure 2.3 shows semi-log plots for flow stress data. These types of plots are used to determine the fit of the Kocks and Chen kinetic law to a specific data set. The kinetic law is rearranged to give a y-axis of the flow stress over the temperature dependent shear stress, and the x-axis is a rearrangement of equation (2.12). Figure 2.3 (a) shows the linear fit of the steady-state flow stress values to the Kocks and Chen model for a homogenization treatment of 8 hr at 500°C. The Kocks and Chen model is able to accurately describe this data. Figure 2.3 (b), shows the fit of the steady-state flow stress data for samples homogenized for 8 hr at 630°C. The Kocks and Chen data is able to describe the data with an x-value less than 16 well, but is limited at values greater than 16. This is a region of low deformation temperature and high strain rate. The kinetic law is limited in this region as this is a region of work hardening.

In summary, empirically based constitutive models such as the Zener-Holloman equations, Sellar-Tegart equation and HST have been investigated for modeling the effects of processing conditions on the flow stress of AA3003, but the advantages of further developing a physically-based flow stress model have pushed the investigation towards using the Kocks and

Chen model. The Kocks and Chen model links microstructure to constitutive behavior as A and n can be made functions of microstructure. The results from Kubiak [5] and Geng [4] showed that such a model could describe the constant strain rate data well, but the physical basis of the model was lost as the derived stress exponent values were much larger, approximately 8 using $A=1.06 \times 10^{36}$ s^{-1}, than the theoretical value of 3, making the model only empirically successful.

$$\log\left(\frac{\dot{\varepsilon}}{s^{-1}}\frac{kT}{\mu b^3}\exp\frac{Q_D}{RT}\right)$$

(a)

$$\log\left(\frac{\dot{\varepsilon}}{s^{-1}}\frac{kT}{\mu b^3}\exp\frac{Q_D}{RT}\right)$$

(b)
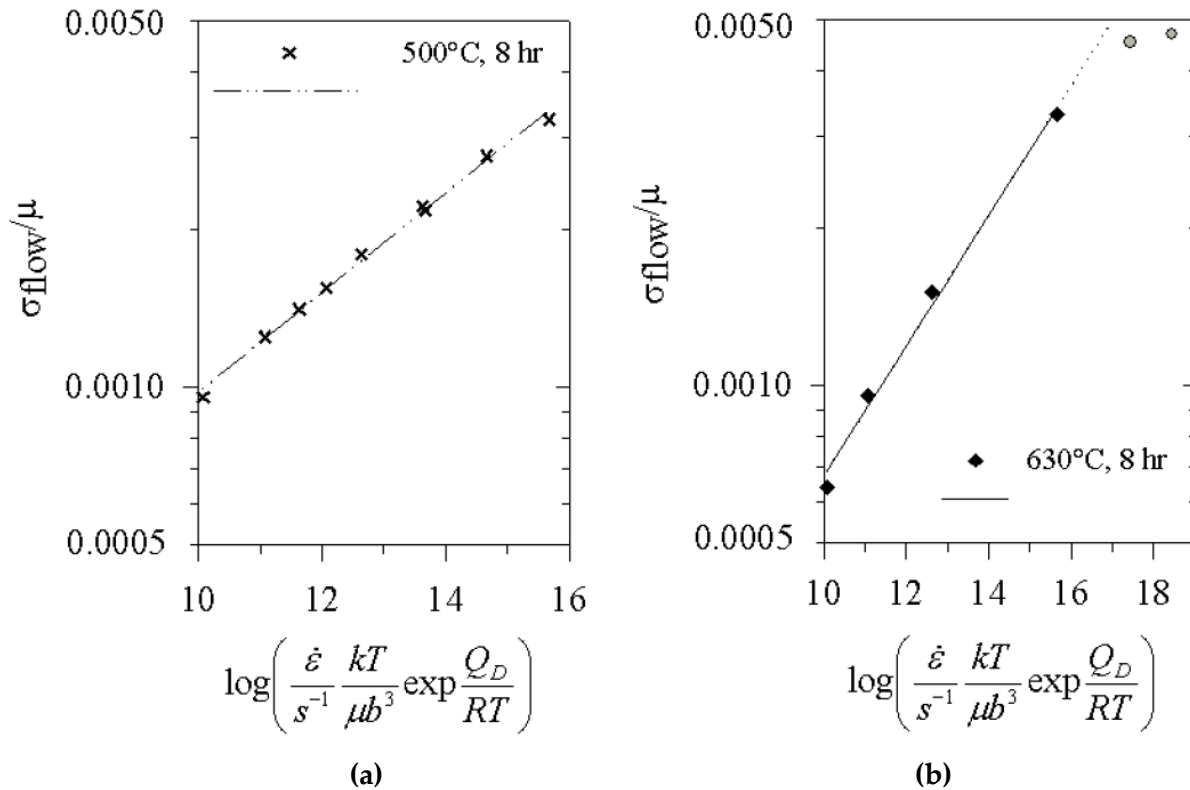
Figure 2.3 – Steady-state flow stress data plotted using Kocks and Chen's constitutive model for AA3003 with (a) 8 h at 500°C and (b) 8 hr at 630°C homogenization. Reproduced with permission from [5].

2.8.3   Influence of Strain Rate Changes on the Flow Stress

Plasticity is path dependent in aluminum and in other polycrystalline f.c.c. metals. A change in strain path affects the rate of hardening and the extent of dynamic recovery [58] [59]. The flow stress and strain hardening rate are highly influenced by variations in strain rate and temperature [50] [60]. Kubiak [5] [11] and Geng [4], have looked at the validity of the Kocks and Chen model within a range of temperatures (400°C to 600°C) and constant strain rates (0.1 s^{-1} to 10 s^{-1}), but did not investigate the ability of the model to predict the behavior of AA3xxx under transient strain rates. Khan and Haowen [50] emphasized that a constitutive relation needs to

define the dependence of the flow stress on the coupled effect of strain hardening, strain rate and temperature. There have been many constitutive models developed and validated using a constant strain rate path [50], but few have looked at the constitutive behavior of a material under various strain rate paths - i.e. increasing the strain rate as the test progresses [60]. The results of Furu et al. [60] have shown the importance of the deformation history in controlling the structure evolution which drives subsequent recrystallization for Al-1 wt% Mg. An increasing strain rate was found to drive a decrease in the subgrain size, and vice-versa.

This chapter has summarized some of the work that has been conducted on the AA3xxx system. Previous work has included characterizing the microstructure evolution of the AA3xxx alloys during casting and homogenization treatments through experiments and models. The as-cast microstructure and homogenized states were characterized and the restorative mechanisms involved in extrusion were touched on. Empirical constitutive models were discussed along with the Kocks and Chen physically-based constitutive model and its applicability to describe the flow stress behavior of AA3003 during high temperature deformation. Chapter 3, describes the scope and objectives of the current study to increase the knowledge of the recrystallization behavior of AA3003 during high temperature extrusion.

3 Scope and Objectives

Aluminum alloys containing manganese (Mn) and iron (Fe) additions are used extensively for heat exchanger applications in the automotive industry. In these applications alloys such as AA3003 (1.27% Mn, 0.54% Fe, 0.10% Si, 0.02% Ti), undergo manufacturing operations that include casting, homogenization, extrusion and brazing. A favorable microstructure for heat exchanger applications is one consisting of fine equiaxed grains, which provide good strength, ductility and corrosion resistance. One of the main goals of such manufacturing operations is to be able to tailor process parameters so that the desired material properties and microstructure profile may be obtained. In return, process optimization leads to reduced production costs and waste. This notion has led many aluminum producers to push for through process modeling. This project is a part of a larger project to develop a process model for AA3xxx.

3.1 Scope

This investigation focuses on the extrusion portion of the processing route that material must undergo before it is turned into a heat exchanger. The alloy of interest is AA3003. This study aims to characterize the as-extruded microstructure for different homogenization treatments and extrusion process conditions (extrusion temperature, ram speed, extrusion ratio) and the predisposition of the material to recrystallize. The following extrusion process parameters where explored:

- Homogenization treatment: temperatures between 500°C and 600°C and durations of 8 h to 24 h.
- Extrusion temperature: 350°C to 500°C.
- Ram speed: 2 mm/s to 36 mm/s
- Extrusion ratio: 17:1 to 280:1

Some of the as-extruded samples underwent post-extrusion annealing in order to investigate the stability of the as-extruded microstructure. The following conditions were explored:

- Temperature: 500°C to 550°C
- Duration: 1 min. to 100 min.
- Water quench at room temperature

High temperature compression testing was conducted for samples homogenized for 24 h at 600°C, and deformed at 500°C under varying strain rate conditions, as work by Mahmoodkani et al. [12] has shown that the strain rate changes during the extrusion process. Testing was conducted using a strain rate which transitions from an initial strain rate of 1 s^{-1} to a final strain rate of 10 s^{-1}.

3.2 Objectives

The following are the objectives of this investigation:

- To quantify the deformed state of the microstructure evolution of AA3003 during high temperature extrusion using standard metallographic techniques.
- To understand if the grains deform geometrically during the extrusion process.
- To determine under what conditions 100% recrystallization is obtained at the centre of the extrudate.
- To investigate the stability of unrecrystallized as-extruded microstructures with respect to Zener Pinning and stored energy.
- To test the constitutive model, developed by Kocks and Chen [56] and applied by Kubiak [5] and Geng [4] to AA3003, to see its ability to capture the effects of the strain rate history on the flow stress of the material.

4 Experimental Methodology

This chapter details the experimental methodology used for the characterization of the as-cast, as-extruded and post-extrusion annealed AA3003. A systematic study of processing conditions for AA3003 was conducted using a laboratory scale fully instrumented extrusion press at Rio Tinto Alcan's (RTA) Arvida Research and Development Centre (ARDC). Billets previously homogenized at different conditions were extruded with a variety of extrusion ratios, ram speeds, and extrusion temperatures. The microstructure of the material was characterized with the use of optical microscopy, resistivity measurements, and electron back scatter diffraction. The material was first characterized in its as-cast and as-extruded states (as provided by RTA) and later some of the samples were further characterized after post-extrusion annealing. High temperature compression samples were machined from an as-cast billet, homogenized and tested under high temperature and strain rates. Figure 4.1 is a flowchart depicting the order in which processing, laboratory tests and characterization were conducted for this investigation.
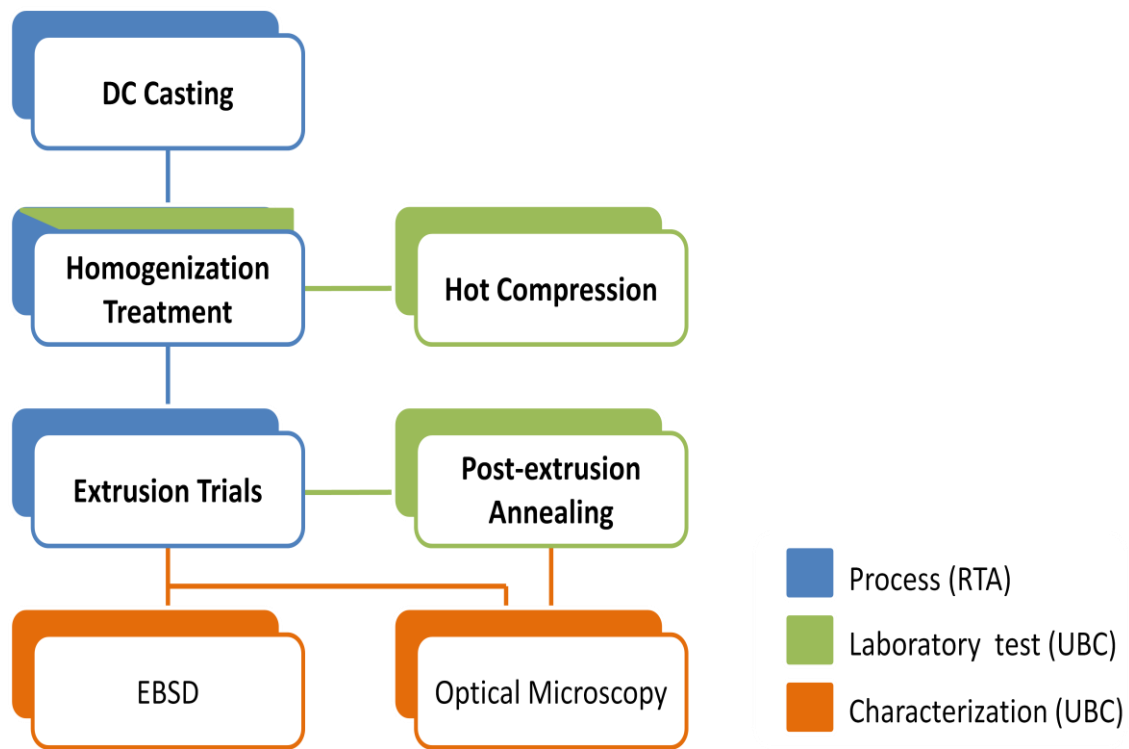
Figure 4.1 - Experimental methodology for the AA3003 extrusion trials and material characterization.

4.1 Initial Material

The initial material was provided by the ARDC located in Jonquiere, Quebec. It was provided in one of two forms: as-cast billets or as-extruded rods. The aluminum alloy examined in the current work was AA3003 with a composition of 1.27% Mn, 0.54% Fe, 0.10% Si, 0.02% Ti by weight.

4.1.1 Homogenization

The extrusion billets produced by DC casting are 101.6 mm in diameter and 200 mm in length. After casting the billets were homogenized in a Carbolite ™ (HRF) circulating air furnace at ARDC. The heating rate during homogenization is 150°C/h up to 50°C below the soaking temperature. For the last 50°C a heating rate of 50°C/h is employed. The temperature profiles for the 3 different homogenization treatments: 8 h at 500°C, 8 h at 550°C and 24 h at 600°C, are depicted in Figure 4.2. After homogenization the billets are water quenched to room temperature.
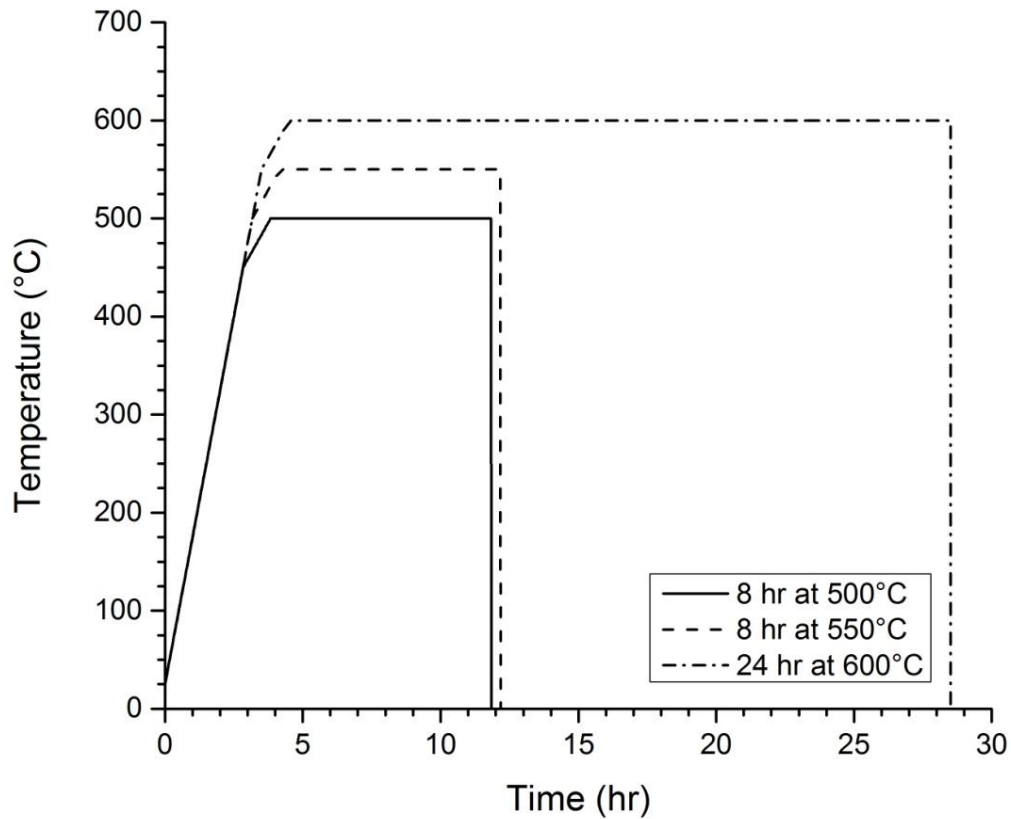
Figure 4.2 - Homogenization treatment temperature profiles.

4.1.2   Extrusion Trials

The extrusion trials were conducted using a laboratory scale fully instrumented extrusion press at ARDC. Prior to extrusion, the homogenized billets are heated to their extrusion temperature in an induction furnace and then loaded into the extrusion press, with heated container and die, using a mechanical loading system. Once loaded in the container the billet upset to a diameter of 106 mm, and is then extruded through the die. The material is extruded into rods of various extrusion ratios using various ram speeds. The material coming out of the die passed into a water quench located 2 m away from the die. A schematic of the process set-up can be seen in Figure 4.3. A total of 7 extrusion trials were conducted for this investigation (Table 4.1).
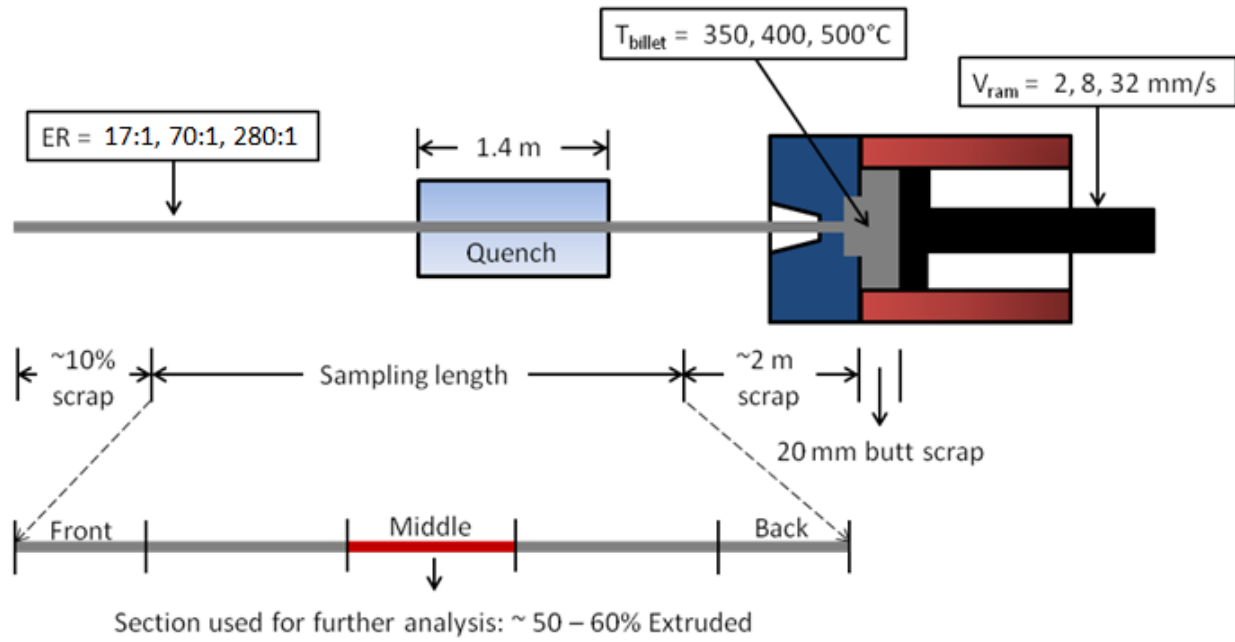
Figure 4.3 - Schematic diagram of the extrusion press setup and water quench, with process conditions.

Table 4.1 – Summary of extrusion trials (Note: the initial diameter of the billet is 106 mm, i.e. the diameter after upsetting of the billet in the container).

Trial No.	Extruded Diameter (mm)	Extrusion Ratio	Extrusion Temperature (°C)
1	12.7	70:1	500
2	25.5	17:1	500
3	6.3	280:1	500
4	12.7	70:1	400
5	25.5	17:1	400
6	6.3	280:1	400
7	12.7	70:1	350

Four process conditions were directly explored in the trials: homogenization treatment, extrusion temperature ($T_{extrusion}$), ram speed (v_{ram}) and extrusion ratio (ER), where ER is defined as follows:

$$ER = \frac{A_b}{A_e} \qquad \text{(4.1)}$$

$$ER = \frac{r_b{}^2}{r_e{}^2} \qquad \text{(4.2)}$$

and A_b is the transverse cross-sectional area of the billet (after upset), and A_e is the transverse cross-sectional area of the extrudate. In this case as the initial cross-section and the final cross-section are the same shape, therefore the ER can be defined as the ratio of the squares of the respective radii (equation (4.2)).

A complete list of the process conditions used can be seen in Table 4.2. A combination of these process conditions produced 27 samples to investigate. The three different homogenization conditions were chosen due to recommendations by Kubiak [5] and Geng [4], in order to obtain a microstructure with high (8 h at 500°C) and moderate (8 h at 550°C) density of dispersoids, along with a structure with few to no dispersoids (i.e. 24 h at 600°C). The extrusion temperatures, ram speeds and ERs were selected in order to encompass a range of interest for industry.

Table 4.2 - Extrusion trial process conditions.

Process	Condition
Homogenization Treatment	8 h at 500°C
	8 h at 550°C
	24 h at 600°C
Extrusion Temperature	350°C
	400°C
	500°C
Ram Speed	2 mm/s
	8 mm/s
	32 mm/s
Extrusion Ratio	17:1
	70:1
	280:1

Data logged during the extrusion tests included: ram position, ram velocity, exit temperature, ram pressure, extrusion temperature, liner temperatures, and die temperatures. During the trials the exit temperature of the extrudate was measured using a hand held probe which was held in contact with the extruding material. This measurement was taken at the back end of the extrudate, at approximately 80% extruded. For the extrusion ratio of 280:1, accurate exit temperature measurements could not be taken due to the small diameter of the extrudate. The electrical resistivity of the extrudates was measured in the lab at UBC.

During the extrusion trials the first 10% of the extruded billet, by volume, was scrapped along with the last 2 m of rod and the 20 mm billet butt (Figure 4.3). The sampling length was then divided into three sections: front, middle and back. For this investigation only the material taken from the middle of the sampling length, which corresponds to approximately 50-60% extruded was examined extensively. This location was selected for the study as it does not include any residual material from the previous billet and deformation induced from chattering, typically found in the front and back ends of the extrudate, respectively.

4.2 Post-Extrusion Annealing

Several of the samples which appeared unrecrystallized after extrusion were then selected for post-extrusion annealing tests. This was done to investigate the stability of the as-extruded microstructure. These samples were annealed in a nitrate salt bath (60% potassium nitrate, 40% sodium nitrite) and quenched in water at room temperature. Samples were annealed for 1 min., 10 min., and 100 min. at temperatures of 500°C, 525°C and 550°C and examined in the as-quenched state. Prior to placing the sample in the salt bath an independent temperature reading was obtained. A second thermocouple immersed in the heating medium at regular intervals and depth levels was used to ensure that there was a maximum thermal gradient of ±5°C from the bottom to the top of the salt bath. To minimize the heating time of the sample a small sample dimension was used (approximately 1 cm^3). The electrical resistivity of the samples was measured before and after the post-extrusion annealing.

4.3 High Temperature Compression Tests

High temperature compression tests were conducted, at a extrusion temperature of 500°C and strain rates ranging from 1 s^{-1} to 10 s^{-1}, using a Gleeble® 3500 Thermo-mechanical Simulator. Various tests were conducted in order to determine the effect of the strain rate path on the final flow stress of the material. Figure 4.4, depicts 3 of the 5 ideal strain rate paths investigated. The first two (not shown in the figure) are constant strain rates of 1 s^{-1} and 10 s^{-1} in

which the strain rate was maintained constant throughout the entire test. The other three (Figure 4.4) tests start at a strain rate of 1 s^{-1} and transition to 10 s^{-1}. The range in strain in which this transition occurs is adjusted from gradual (0.2 to 0.4), moderate (0.2 to 0.3) to rapid (0.2 to 0.25).
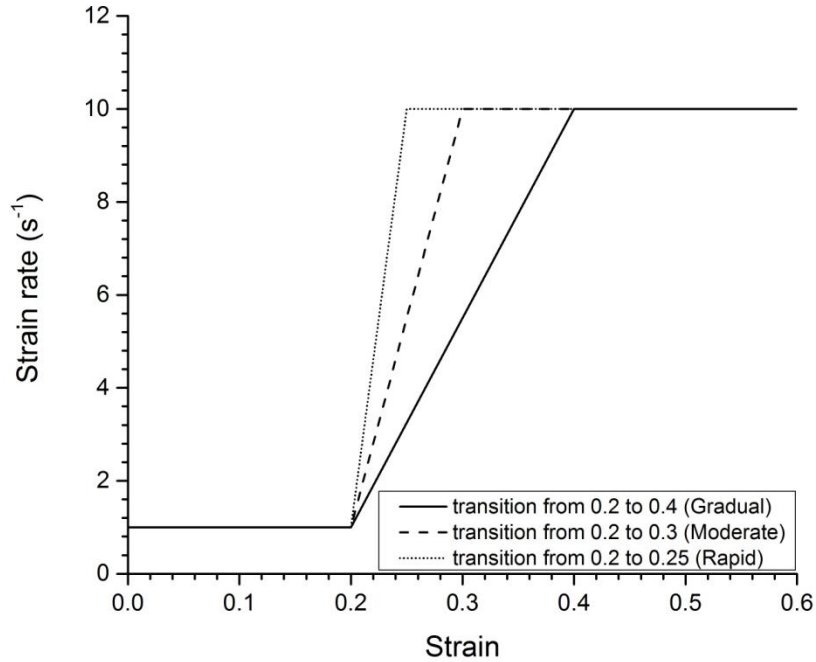
Figure 4.4 - Ideal strain rate transitions for high temperature compression tests.

4.3.1 High Temperature Compression Cylinders

The compression cylinders for the tests were machined from as-cast billets. The location along the billet where the cylinders were sectioned and the sample dimensions can be seen in Figure 4.5. The compression cylinders were sectioned approximately 10 mm from the edge of the billet and 10 mm from the centre of the billet as this region has minimal grain size variation, and is free of inverse segregation. The samples were also sectioned as shown in order to make sure that the axial direction during compression was parallel to the axial direction of the parent billet. The compression cylinders were machined to have a diameter of 8 mm and a length of 12 mm. The cylinders were then homogenized in a Carbolite™ (HRF) recirculating air furnace and water quenched. A homogenization treatment of 24 h at 600°C was selected as it provides a microstructure almost free of dispersoids. The heating profile used is the same as the one shown in Figure 4.2, in Section 4.1.1. Thermocouple data was recorded during the homogenization using instruNet™ software.
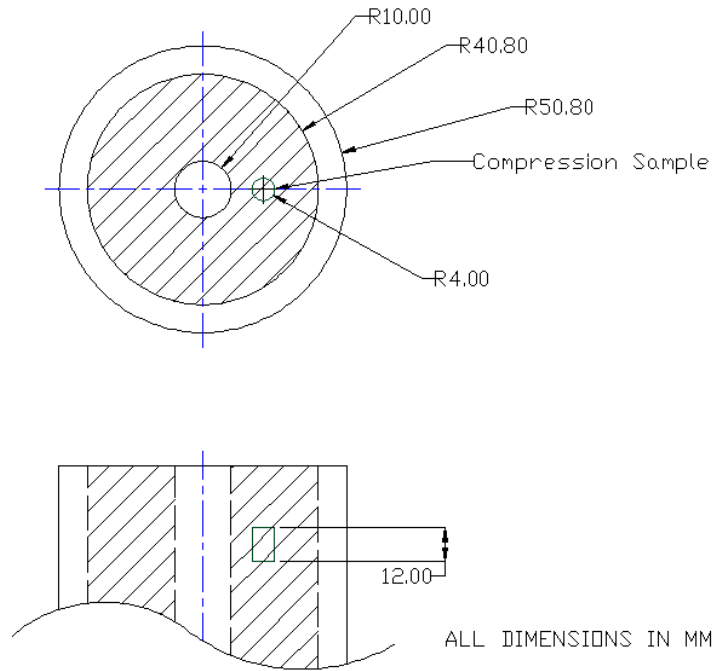
Figure 4.5 - High temperature compression sample dimensions and sectioning location from the billet.

4.3.2 High Temperature Compression Test

A type K thermocouple was spot welded to each compression cylinder at the middle of the length. The compression cylinder ends were lubricated using nickel paste and one layer of 0.25 mm graphite foil, 12 mm in diameter, was placed at each end. The sample was then loaded into the Gleeble® and pre-loaded to 200 N, in order to hold the sample in place. The low force jaws, a 1,000 lb (4.4 kN) load cell, dilatometer and Argon back-fill were used for all tests. A heating rate of 5°C/s was used, and once at the deformation temperature (500°C), the sample was held at temperature for three seconds before deformation commenced. The cooling of the sample was not controlled. Gleeble® output data was collected using QuickSim software and included: Time (sec), Diameter (µm), Force (N), Power Angle (°C) and Temperature (°C). The electrical resistivity of the samples was measured both before and after high temperature compression.

4.3.3 Data Analysis

The data was post-processed using Origin Pro 9.0. Stress-strain curves were constructed, and the yield stress and steady-state flow stress for each test were determined. The true strain was calculated using Equation (4.3), and the true stress was calculated using Equation (4.4).

$$\varepsilon = 2ln\left(\frac{d_0}{d_0 + \Delta d}\right) \tag{4.3}$$

$$\sigma = \frac{F}{\left(\frac{\pi(d_0 + \Delta d)^2}{4}\right)} \tag{4.4}$$

where d_0 is the initial diameter of the sample, Δd is the change in diameter measured by the dilatometer, and F is the force. Details regarding the data post-processing routine can be found in chapter 4.3.4. The temperature dependent parameters (Burger's vector, Shear and Young's Moduli) used in this study were calculated using methods detailed in [5].

Gleeble data such as yield stress, steady-state flow stress and strain rate were also determined from the obtained data. The steady-state flow stress was taken as the average stress over a range of strain from 0.4 to 0.6 for all tests. This was done by obtaining a linear relationship for the curve in the specified range. This relationship was used to calculate the stress at 0.4 and 0.6 strain. The average of these two values was taken as the steady-state flow stress. The comparative strain rate, and temperature were taken at a strain of 0.5 for all tests.

4.3.4 Experimental Strain Rates

The test data was post-processed to determine the strain rates to be used as inputs for the constitutive model. The dilatometer versus time data was first plotted in order to determine what the initial dilatometer reading (i.e. initial diameter) was at the beginning of deformation. This value was used to calculate the true strain and true stress using equations (4.3) and (4.4). This information was plotted to produce a stress-strain curve that was smoothed using adjacent averaging. An example of the data smoothing can be seen in Figure 4.6, showing the stress-strain curve for 1 s^{-1} strain rate at 500°C.

The smoothed stress and strain curve data was used for further calculations and analysis. The data had to be smoothed due to the introduction of noise from the force load cell (Figure 4.7). The smoothed strain was plotted against time (Figure 4.8) and the curve was differentiated to obtain the strain rate data (Figure 4.9). This data was then plotted against the smoothed strain. The strain rate was then smoothed using adjacent averaging. The smoothed strain rate data was then used for the constitutive model calculations.
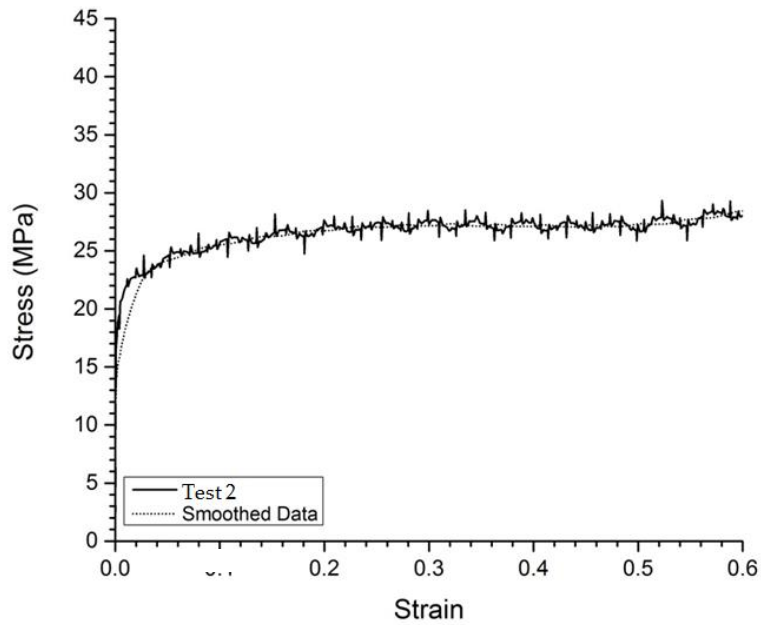
Figure 4.6 - Raw stress-strain curve (Test 2) and smoothed stress-strain curve (Smoothed data) for a extrusion temperature of 500°C and strain rate of 1 s⁻¹.
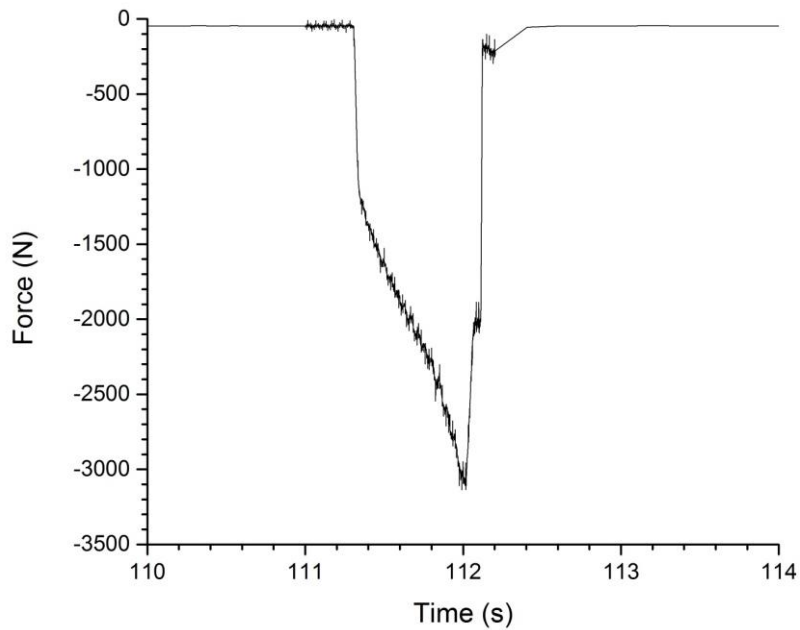
Figure 4.7 - Force load cell experimental data for test a strain rate of 1 s⁻¹, Test 2.
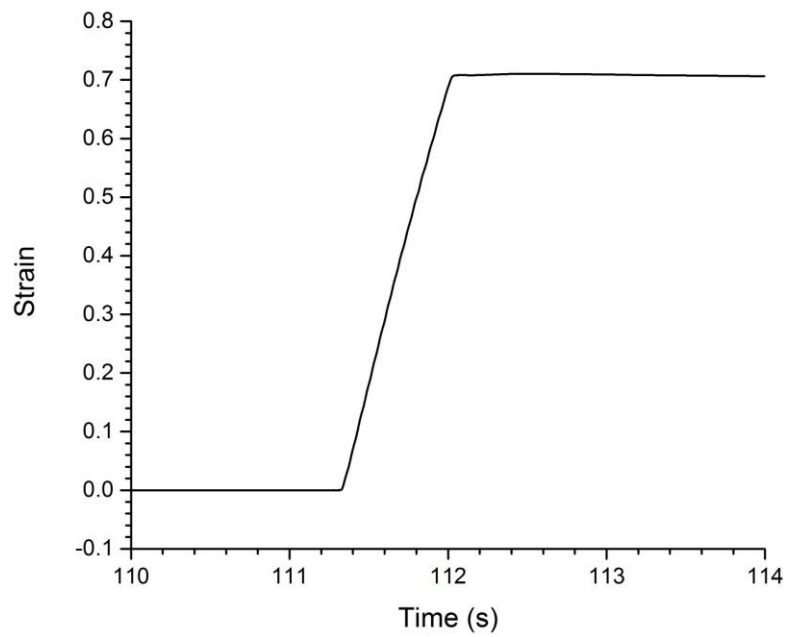
Figure 4.8 – Experimental strain versus time plot used to obtain strain rate data for strain rate of 1 s^{-1}, Test 2.
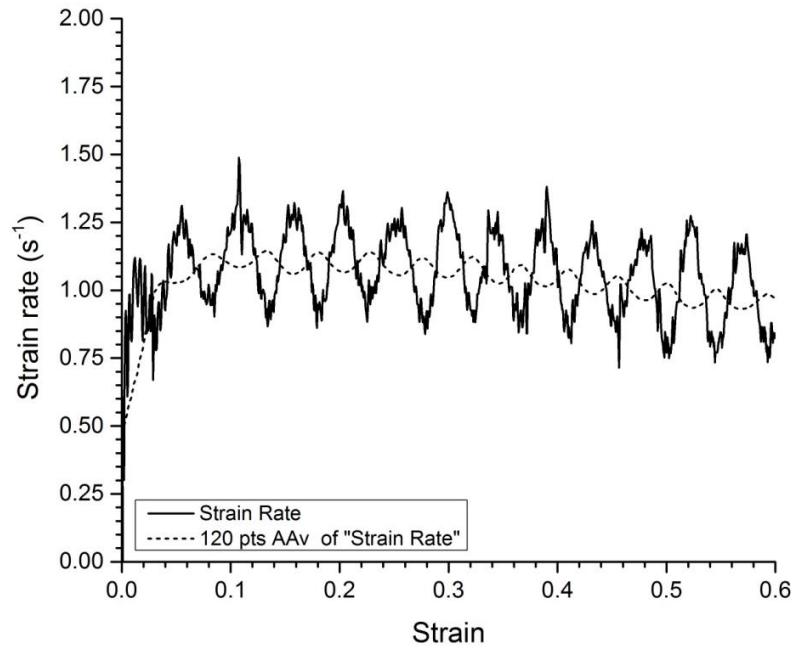
Figure 4.9 - Strain rate versus strain for a strain rate of 1 s^{-1}, Test 2.

4.4 Electrical Resistivity

Electrical conductivity measurements were made at various stages of testing. Electrical conductivity data was collected from the as-extruded samples, the post-extrusion annealing samples (before and after annealing) and the high temperature compression cylinders (before homogenization, before deformation and after deformation). These measurements were obtained through the use of a Sigmatest® 2.069 (by Foerster Instruments Inc.™), with an 8 mm diameter probe, at a frequency of 60 kHz. Samples with a diameter less than 8 mm could not be analyzed using the 8 mm probe, therefore there are no resistivity measurements for samples of ER of 280:1. The Sigmatest® was calibrated prior to each measurement, and the temperature was allowed to stabilize at room temperature before conducting any readings. The calibration was performed using two standards and one air point. The Sigmatest® has a conductivity measuring accuracy of ±0.5% and a resolution of ±0.1% of the measured value at 60 kHz and a temperature measuring accuracy of 0.5°C [61]. If the temperature fluctuated by ±5°C, relative to the temperature of last calibration, the system was recalibrated. The data was output in units of MS/m. Electrical conductivity was converted to resistivity using Equation (4.5), where ρ is the resistivity of the sample in nΩm and γ_c is the electrical conductivity in MS/m. Each sample had three measurements conducted at each frequency and the reported values are the averages of this data. The standard deviation associated with each electrical resistivity measurement was found to be approximately ±0.22 nΩm.

$$\rho = \frac{10^3}{\gamma_c}$$
(4.5)

4.5 Metallography

This section will detail the methods used at various stages of the microstructure characterization of the material.

4.5.1 Sample Sectioning

All samples prepared for optical microscopy (OM) or scanning electron microscopy (SEM) were prepared by standard metallographic techniques. Samples were sectioned by the machine shop using a Marvel Series 8 vertical band saw (1 x 4/6″ teeth by 14′6″ blade), DoAll Vertical band saw (1/2″ x 12/14″ x 12′10″ blade) and Ex-cell-o Milling Machine.

The as-cast billet samples for initial grain size analysis were sectioned as shown in Figure 4.10. Samples were taken from 3 sections along the radius of the billet. Location 1 is from

the centre, location 2 is at approximately the midpoint of the radius, and location 3 is close to the surface. All 3 samples were 0.5 mm x 15 mm x 20 mm in dimension.

In order to obtain information from both the longitudinal and transverse sections the as-extruded samples with ER of 17:1 and 70:1 were sectioned as shown in Figure 4.11. Due to sample symmetry only ¼ of the rod was evaluated, except for the samples with an ER of 280:1. Due to the 280:1 small dimension (diameter of 6.33 mm), the entire surface along the transverse and longitudinal were examined. Both the post-extrusion annealing samples and the constituent particle analysis samples were sectioned in the same manner as the as-extruded samples, but only the transverse sections were analyzed.
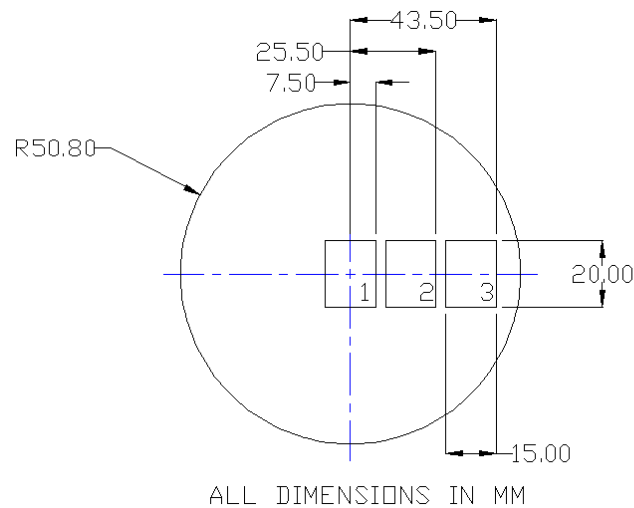
Figure 4.10 - As-cast grain size analysis sample sectioning schematic.
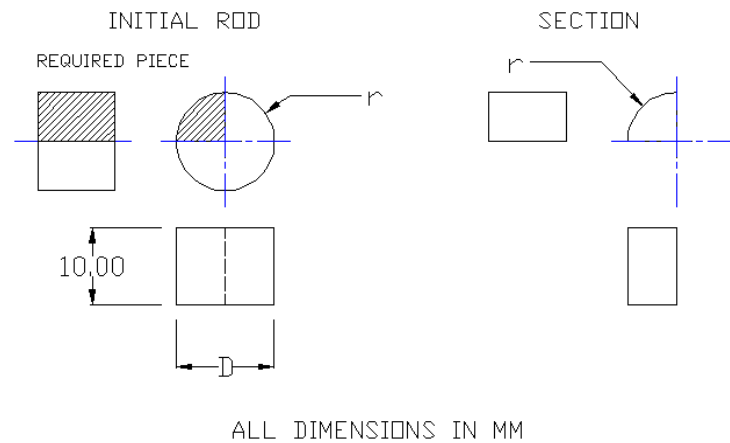
Figure 4.11 - As-extruded rod sample sectioning schematic. For 17:1 ER, D = 25.54 mm; 70:1 ER, D = 12.69 mm.

Samples prepared for EBSD were only examined along the longitudinal cross-section. Figure 4.12 and Figure 4.13 show the respective sample sectioning used for samples with ER of 17:1 and 70:1. The one sample with ER of 280:1 was sectioned in the same manner as the 70:1 samples. For all ER the surface of interest was along the centre of the longitudinal section of the extrudate. This surface is depicted in Figure 4.13. The "centre" was defined as the region 1/3 of the radius away from the centre point of the extrudate. For example for the 70:1 samples the maximum distance from the centre point of the rods classified as being the "centre" was 2 mm.
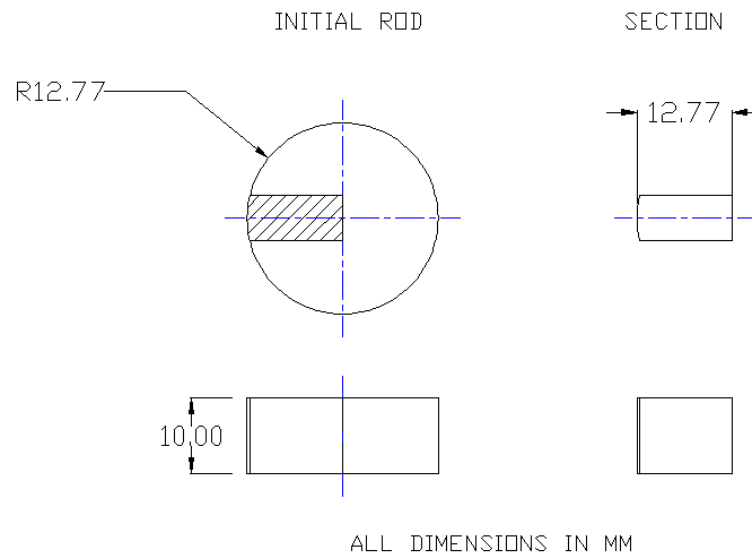
Figure 4.12 - ER of 17:1 sample sectioning for EBSD analysis.
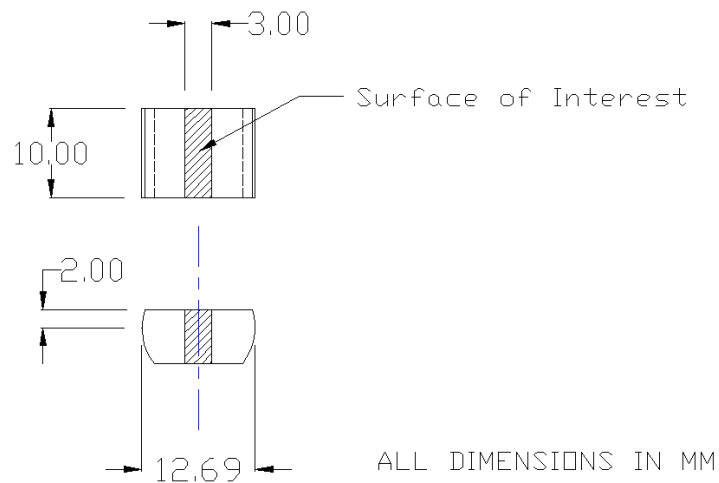
Figure 4.13 - ER of 70:1 sample sectioning for EBSD analysis.

4.5.2 Surface Preparation

Optical microscopy (OM) samples were first sectioned and then a conductive foil was attached to the sample using MG Chemicals® Silver Conductive Epoxy in order to make sure the sample could later be anodized. The samples with the attached foil were mounted using LECO Lecoset™ 100 castable mounting material. The samples were then mechanically ground, and polished using a Buehler EcoMet IV with a Buehler EuroMet I power head automatic polisher. A force of approximately 10 N was applied per sample during grinding and polishing. The grinding and polishing schedules are shown in Table 4.3 and Table 4.4. After each of the grinding and polishing steps the samples were rinsed with water and the polishing plate was wiped clean with a damp cloth. Once polishing was completed the samples were rinsed with water, followed by an ethanol rinse and then dried using a blow dryer.

Table 4.3 - Grinding schedule.

Type of Paper	Grit	Speed (rpm)	Time (min)	Lubricant
SiC	320	150	4	Water
SiC	400	150	8	Water
SiC	600	150	10	Water
SiC	800	150	15	Water

Table 4.4 - Polishing schedule.

Type of Paper	(µm)	Speed (rpm)	Time (min)	Lubricant
LECO FEPA	6	150	20	6 µm diamond suspension + microid diamond compound extender
LECO Lecloth or Imperial	1	125	25	1 µm diamond suspension + microid diamond compound extender
LECO Imperial	0.05	125	5	Colloidal silica

4.5.3   Anodizing

Barker's Reagent (3% Flouroboric acid (48% HBF_4 conc.) in distilled water) was used to anodize the material, at room temperature, in order to reveal the microstructure. In the anodizing set-up pure aluminum was used as the cathode, and the sample as the anode. The sample was rinsed before being anodized. The sample and the anode were hooked up to the power supply (BK Precision 0-60V, 0-2A DC Power Supply), and then the power supply was turned on. The sample was immersed in the reagent at an angle in order to eliminate any air bubbles forming on the surface to be anodized. Once in the solution the voltage was slowly turned up to 30 to 34 V DC. The sample was maintained under these conditions for 70 to 120 s, depending on the sample cross-sectional area.

4.5.4   Optical Microscope

Microstructural observations on the anodized as-cast, as-extruded and post-extrusion annealed samples were made using a Nikon Epiphot 300 optical microscope under polarized light (crossed Nicols position; colour temperature compensation filter NCB11) at magnifications of 50x, 100x, 200x and 500x. Sample images were obtained using Clemex Vision PE 6.0 image analysis software. This software was also used to build mosaic images. This was primarily done to qualitatively determine initial grain size in the as-cast material and the extent of recrystallization for the as-extruded and post-extrusion annealing material.

4.5.5   As-Cast Grain Size Analysis

The as-cast billet microstructure was analyzed using specimens that had been sectioned, prepared, and analyzed as described in chapters 4.5.1 to 4.5.4. The micrographs of the structure, at 100x magnification, were then printed and a transparency was placed on top. The grain boundaries were then traced using a fine tip permanent marker. The transparencies were then scanned and imported into the Clemex software for analysis. Figure 4.14, shows a micrograph for location 1 and the corresponding transparency. Once calibrated to the corresponding magnification (at a magnification of 100x the calibration is approximately 0.1 μm/pixel) the following built-in Celemex analysis routines were used: Aspect Ratio, Circular Diameter, Spherical Diameter, Area and ASTM E112-96. This was done three to four times for each location in order to obtain a good statistical distribution of the structure. Please note that the experimental grain sizes reported are the circular diameter. The reader is referred to Appendix B for the full Clemex routine and comments on the routine parameter sensitivity.

| (a) | (b) |
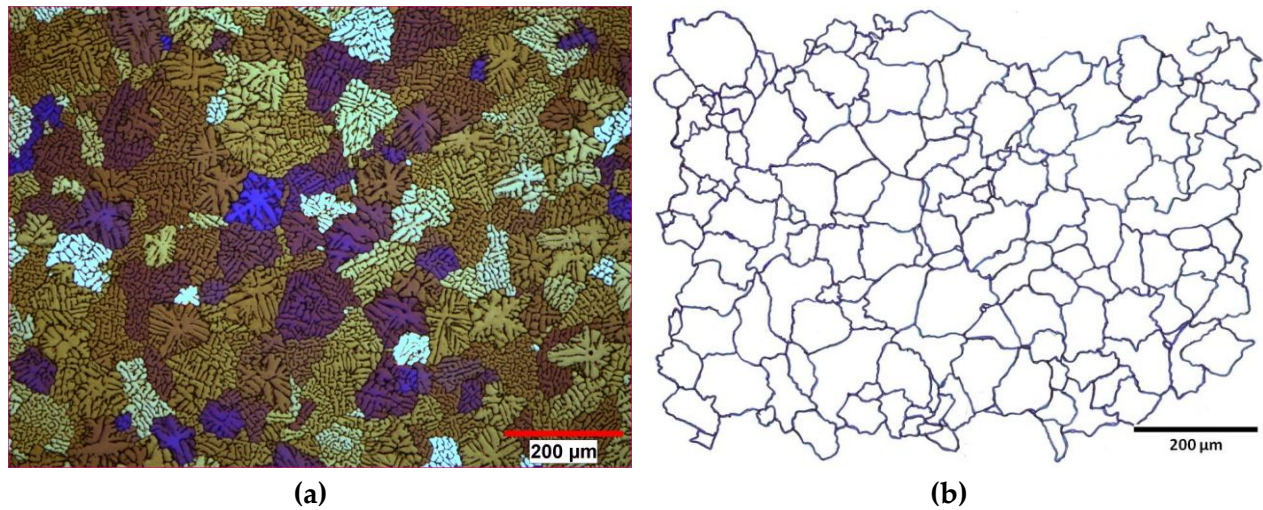
Figure 4.14 - (a) Anodized 100x micrograph of location 1 of the as-cast 3003 billet, (b) transparency tracing of the grain boundaries of (a). (Refer to Figure 4.10 for a schematic of the locations).

4.5.6   Constituent Particle Distribution Analysis

In order to investigate the constituent particle distribution through the profile, of the 70:1 as-extruded samples, two longitudinal samples were ground and polished and etched with 0.5% hydrofluoric acid (48% HF) in distilled water. The dilute hydrofluoric solution was used to reveal the constituent particles. The samples were immersed in the etchant for 60 s, at room temperature, and then rinsed with ethanol and dried using a blow drier. These samples were then observed using the Nikon Epiphot 300 in bright field and black and white settings at a magnification of 500x. The images were printed and the constituent particles were manually traced onto a transparency, which was scanned and analyzed by the Clemex software. A Clemex software routine was used to obtain a quantitative analysis of the constituent particles such as: size, aspect ratio, area fraction and number density was done using the Clemex software routine. An example of the image analysis process is shown in Appendix B.

4.6 Electron Back Scatter Diffraction

Electron Back Scatter Diffraction (EBSD) was conducted in order to gain further information regarding grain geometry and grain thickness of fibrous unrecrystallized samples that could not be resolved through the use of OM.

4.6.1 Sample Preparation

EBSD samples were mounted using System Three Cold Cure. Samples were ground and polished as described in chapter 4.5.2. The samples were then placed in the Buehler VibroMet 2® vibratory polisher for three hours. An Imperial cloth and colloidal silica were used for this final polish. The samples were mounted on to the specimen holders and no additional weights were utilized. After vibratory polishing the samples were rinsed with ethanol, placed in a beaker with ethanol in an ultrasonic bath for 5 minutes, then rinsed with ethanol again and dried with a blow drier. The samples were then removed from the mounting material by carefully cutting them out using a hack saw. They were then mounted onto stubs and etched for 2 minutes using the DESK II: Denton Vacuum.

4.6.2 Test Details

EBSD was conducted using a Zeiss Σigma FE-SEM equipped with the GEMINI column and EDAX DigiView IV EBSD Camera. Data was collected using EDAX TSL Orientation Imaging Microscopy (OIM™) Data Collection software and processed using EDAX TSL OIM™ Analysis 6. EBSD analysis was conducted on the centre region of the as-extruded samples. The analysis was conducted at a magnification of 90x (capturing an area of approximately 1 mm by 1 mm), using 8 x 8 binning, a working distance of 8 to 11 mm, and a step size of 0.6 μm to 1 μm. Inverse pole maps were produced using the clean-up procedure described in Appendix C.

4.6.3 EBSD Map Clean-up

This section shows a sample of run information, and the clean-up procedure used on the EBSD data in order to obtain "cleaned" Inverse Pole Figure (IPF) Maps. The same clean-up procedure was used for all samples. The varying parameter from sample to sample was the "Min. grain size", as this was dependent on the step size used during the EBSD run. As a range of step sizes was used (from 0.6 μm to 1 μm) a range of pixel values was used in order to obtain a constant minimum grain size of approximately 2 μm. Therefore runs that had a step size of 0.6 μm had a minimum grain size of 3 pixels; whereas runs that had a step size of 1 μm had a minimum grain size of 2 pixels. The "Grain Tolerance Angle" was always maintained at 2°, and all clean-up methods were only set for a single iteration. Depending on the "Average Confidence Index" of the run a single iteration grain dilation led to a grain removal amount of 8.1 to 41.1%, with a higher average confidence index have a lower removal amount and vice versa. For the EBSD map clean-up procedure details please refer to Appendix C.

4.6.4 Grain Thickness Measurements

The grain thickness of the 'unrecrystallized' samples was determined by using point to point misorientation vectors and the cleaned EBSD IPF maps. After cleaning the IPF map, and adding in high angle grain boundaries (defined here as misorientation greater than 15°), five vector lines were drawn perpendicular to the extrusion direction. One vector line was drawn at a time at various locations in order to gain improved statistics, as shown in Figure 4.15. By doing this one can obtain a distance (µm) versus misorientation (°) profile (Figure 4.15 (b)) and corresponding data which can then be exported as a .txt file and imported into Excel. First the data with misorientation angles less than 15° was sorted out. Then the distance between high angel grain boundaries (HAGBs) was determined by looking at the corresponding distance data (i.e. the location between HAGB A and HAGB B was determined). This distance is taken as the grain thickness.

(a)   (b)
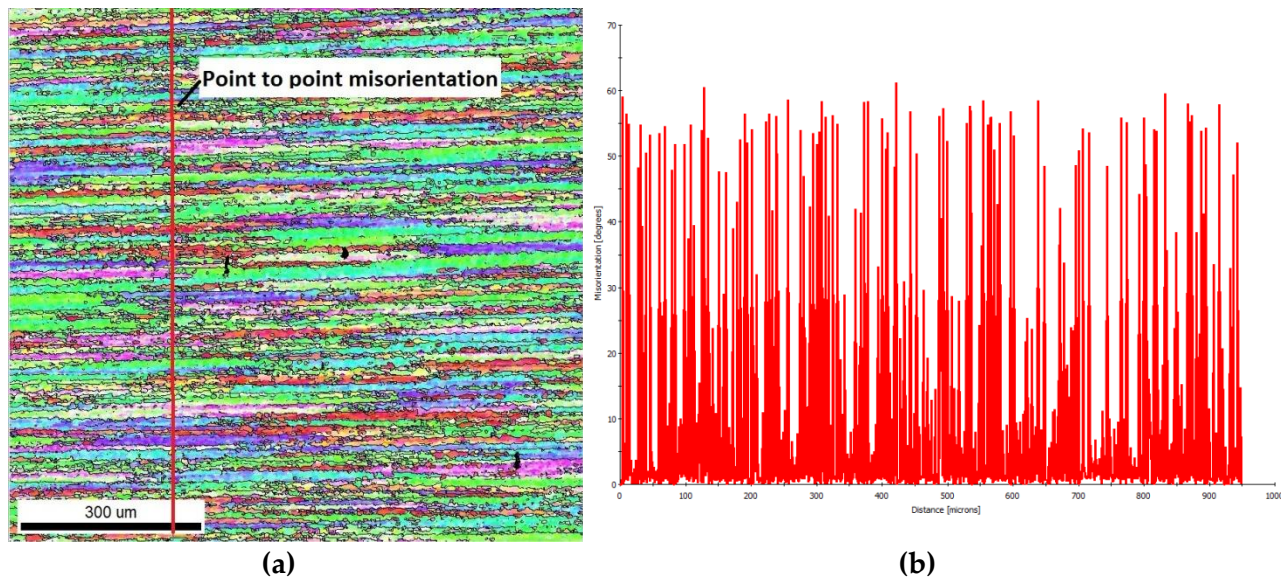
Figure 4.15 - (a) EBSD map point to point misorientation vector, and (b) misorientation profile for vector# 2 of an 70:1 ER sample (homogenization treatment of 8 h at 500°C, extrusion temperature of 500°C and ram speed of 8 mm/s).

The data was then further processed by setting a minimum grain thickness equivalent to the minimum grain size used in the clean-up of the EBSD data (i.e. approximately 2 µm depending on the step size). Any grains with thickness less than the set minimum grain size were sorted out of the data set and the grain thicknesses were recalculated as before (i.e. finding the distance between HAGB A and HAGB B). This data was then used to determine the average grain thickness for each vector. All average data reported is for a set of five vectors. Table 4.5,

shows an example of the distribution for each vector and the group of vectors for a 70:1 ER sample. The average 2-D planar thickness for a set of vectors was then multiplied by a correction factor of 1.2 [62] to provide an estimate of the 3-D grain thickness (i.e. mean equivalent volume diameter) from measurements made using the EBSD maps.

Table 4.5 - Grain thickness vector data set for a 70:1 ER sample (homogenization treatment of 8 h at 500°C, extrusion temperature of 500°C and ram speed of 8 mm/s), using a minimum grain thickness boundary of 2 μm.

Vector #	Count	Average 2-D grain thickness (μm)	Minimum 2-D grain thickness (μm)	Maximum 2-D grain thickness (μm)
1	118	7.8	2.0	31.0
2	140	6.7	2.0	28.0
3	132	6.9	2.0	23.0
4	127	7.3	2.0	39.0
5	119	7.8	2.0	34.0
Total/Average	*636*	*7.3*	*2.0*	*31.0*
Standard deviation		*0.52*	*0*	*6.04*

Chapter 4 provided the experimental methodology used for the metallurgical characterization of the as-cast, as-extruded and post-extrusion annealing samples. Details on the high temperature compression test set-up along with the cleaning of the data were reported along with information regarding the EBSD IPF map grain thickness measurements. Chapter 5 details the results of the conducted experiments.

5 Results

This chapter presents the results of the experimental work detailed in chapter 4. The microstructure evolution of AA3003 is qualitatively and quantitatively assessed through various steps throughout the high temperature extrusion process. This includes the qualitative microstructure characterization of the as-cast, as-extruded, and post-extrusion annealing AA3003. This was done through the use of optical microscopy, and the quantitative analysis through electrical resistivity measurements, and EBSD. This chapter also details the results of the high temperature compression tests which explored the effect of a variable strain rate path on the final flow stress of the material.

5.1 Extrusion Trial Data

During the extrusion trials a total of 7 trials were conducted and the tests were divided into trial groups as described in Table 4.1 in chapter 4.1.2. The time, ram position, ram velocity, ram pressure, extrusion temperature, liner temperature and die temperature were logged during the extrusion trials. Table 5.1 shows the experimentally determined ram speed, extrusion temperature, liner temperature, and container temperature for several tests conducted in 3 different trials (trials 1, 2 and 3). The liner temperatures reported are for the location closest to the entrance of the die (approximately 30 mm away). All of these tests were for samples that had been homogenized for 8 h at 550°C and were set to be extruded at a temperature of 500°C. The 17:1 ER tests was the fourth of trial #2. The 1.60 mm/s and 7.76 mm/s 280:1 ER tests were the fourth and sixth tests of their trials, respectively. The 70:1 ER tests with ram speeds of 1.84

mm/s, 7.90 mm/s, and 30.6 mm/s were the fifth, eleventh and fourteenth tests of trial #1, respectively.

The ram speed was found to be within ±5% of the set ram speeds tests of 8 mm/s and 32 mm/s. The ram speed deviation for 2 mm/s was up to 20% lower than the set point during extrusion (e.g. 280:1 ER, 8 h at 550°C, $T_{extrusion}$ = 500°C, v_{ram} = 1.60 mm/s). The extrusion temperatures were all within ±1% for samples with set extrusion temperatures of 500°C and 400°C. There was no temperature data for trial with an extrusion temperature of 350°C. It should be noted that this temperature is the temperature of the preheated billet moments prior to the commencement of extrusion.

Table 5.1 – Extrusion trial data for a selection of tests extruded at 500°C.

Trial #	Test #	Extrusion Ratio	Homogenization Treatment	Ram Speed, v_{ram} (mm/s)	Extrusion Temperature, $T_{extrusion}$ (°C)	Liner Temperature (°C)
2	4	17:1	8 h at 550°C	7.74	498	479
1	5	70:1	8 h at 550°C	1.84	497	456
1	11	70:1	8 h at 550°C	7.90	496	461
1	14	70:1	8 h at 550°C	30.6	499	463
3	4	280:1	8 h at 550°C	1.60	500	464
3	6	280:1	8 h at 550°C	7.76	502	472

Figure 5.1 shows the liner temperatures for trial #1. From this figure it can be seen that the tests were run continuously and that through the entire duration of the trial (approximately 1 hr), the temperatures did not deviate by much. For all trial sets the extrusion temperature and liner temperatures did not fluctuate by more than approximately ±30°C. As the extrusion trial progressed there was a gradual increase in the liner temperatures. The maximum temperature increase seen was approximately 20°C. Only one sample (70:1 ER, 8 h at 500°C, extrusion temperature of 400°C, and ram speed of 8 mm/s) had to be removed from being further investigated as there was a jam during extrusion and the actual extrusion temperature could not be determined.
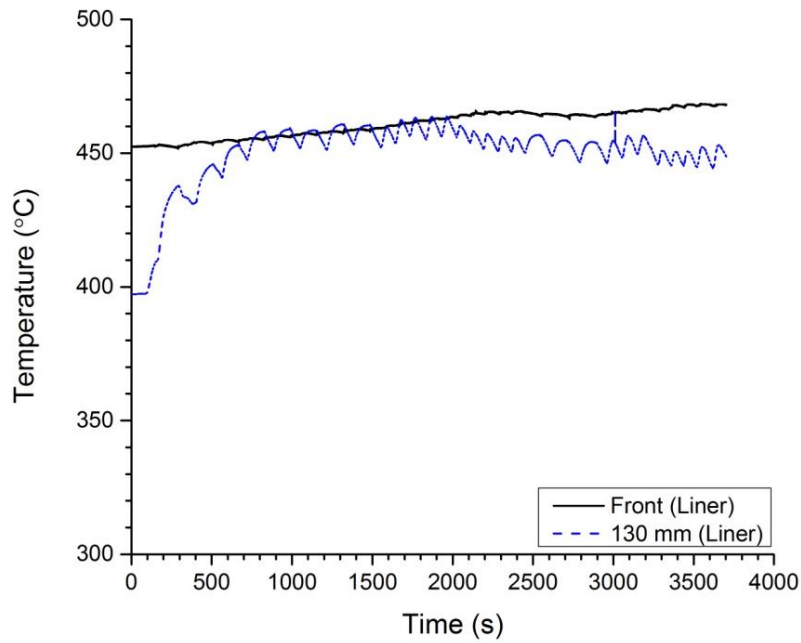
Figure 5.1 - Liner temperatures near the die (front) and 130 mm from the die (130 mm) during the extrusion of 70:1 ER samples with extrusion temperature of 500°C.

5.2 As-Cast Microstructure

The as-cast microstructure was first characterized using anodized samples and optical microscopy using polarized light. The utilization of the Clemex software's built-in circular diameter routine was later used to determine the as-cast grain size. The average equivalent circular diameter was measured as 60.8 μm, 60.6 μm, and 67.7 μm at locations 1, 2 and 3 (Figure 4.10), respectively. This corresponds to an average equivalent volumetric diameter of 73.0 μm, 72.7 μm, and 81.2 μm at locations 1, 2 and 3, respectively. The equivalent circular diameter measurements were converted to an equivalent volumetric diameter by multiplying by a factor of 1.2 [62]. Figure 5.2, shows optical micrographs of the anodized as-cast structure for the three various locations. It can be seen that the variations in the grain size are minor through the cross-section of the billet, and a minimum variation in composition is supported by electrical resistivity data. At location 1 the electrical resistivity was measured as 62.5 nΩm, while at location 2 and 3 the electrical resistivity was measured as 61.6 nΩm and 62.5 nΩm, respectively. Resistivity measurements were taken along the radius of the billet from the centre to the surface, approximately 1 measurement every centimeter, and the standard deviation of the values was found to be 0.43 nΩm. A variation in the as-cast grain structure from centre to surface is also expected due to the nature of the casting process used. The grain structure is dependent both on the cooling path (the billet solidifies from the surface to the centre) and on production factors such as the amount of Ti addition and the length of stirring [63].

(a)

(b)

(c)
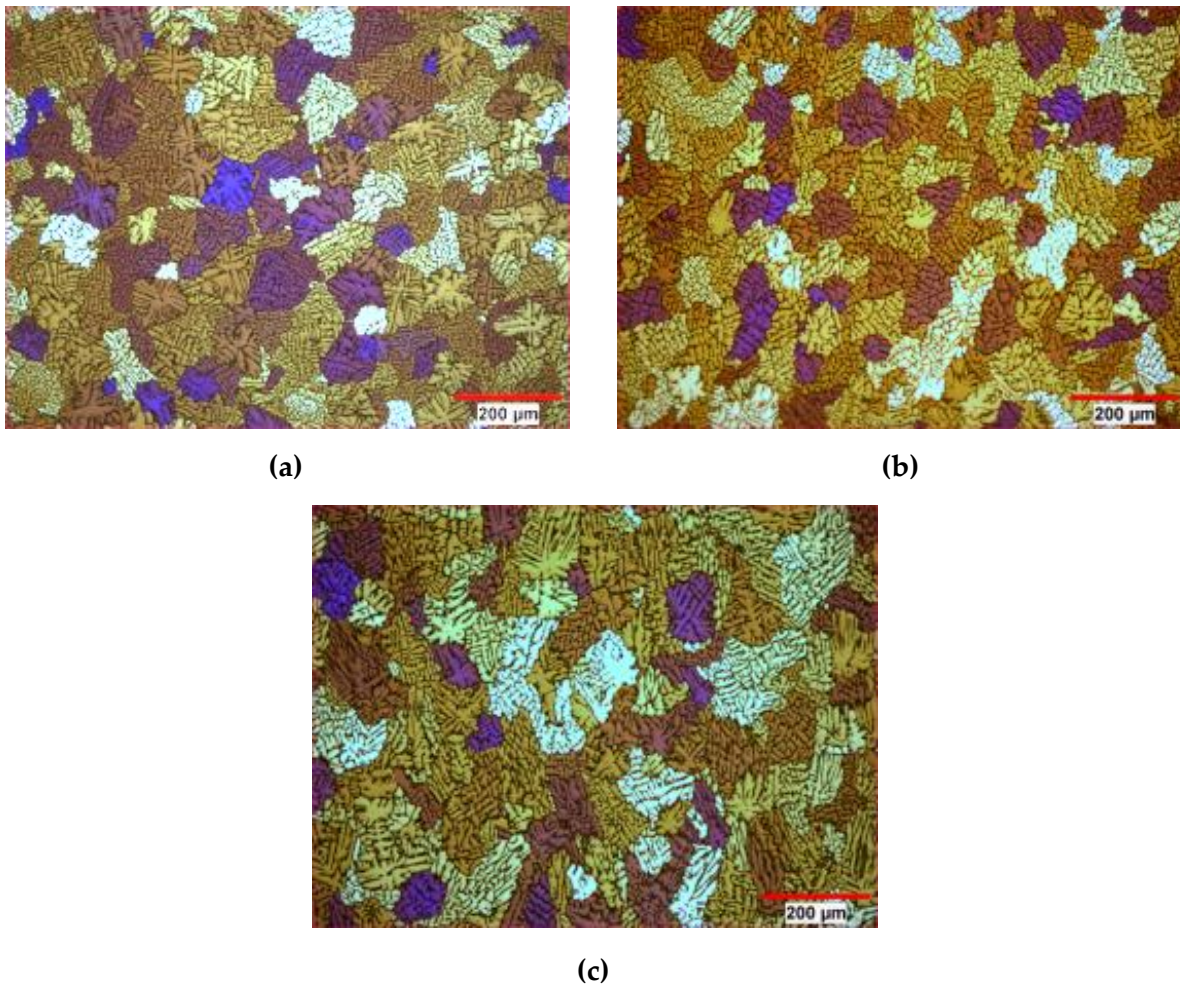
Figure 5.2 - Anodized as-cast optical micrographs for locations (a) 1, (b) 2, and (c) 3 at a magnification of 100x under polarized light (Refer to Figure 4.10 for a schematic of the locations).

5.3 As-Extruded Microstructure

The as-extruded microstructure was then characterized in the same manner as the as-cast samples. Samples that were not recrystallized after extrusion were then analyzed using EBSD. The results are presented in the following sections.

5.3.1 Grain Structure

The as-extruded microstructure was characterized using optical microscopy and polarized light. Every sample was ground, polished and anodized as described in chapter 4. Mosaics were made for the transverse and longitudinal sections of each sample (chapter 4.5.4) and then tabulated. The tables provided information regarding the effect of homogenization,

ram speed, extrusion temperature and ER. In order to more easily describe characteristics of a sample across the section the schematic shown in Figure 5.3 details the location of each region.

Surface (~ 7/8r to r)
Sub-surface (~ 3/4r to 7/8r)
½ radius (~ 1/3r to 3/4r)
Centre (~ 0 to 1/3r)
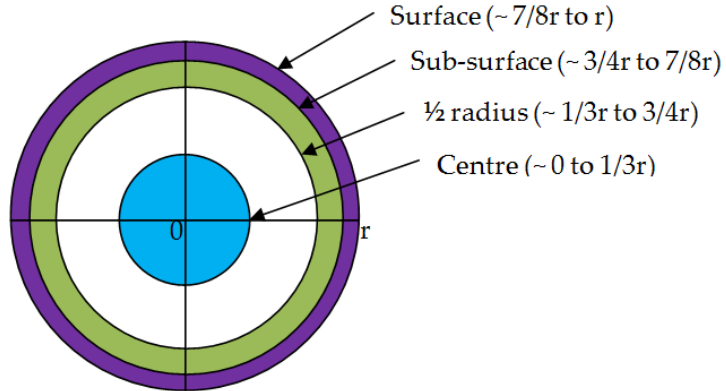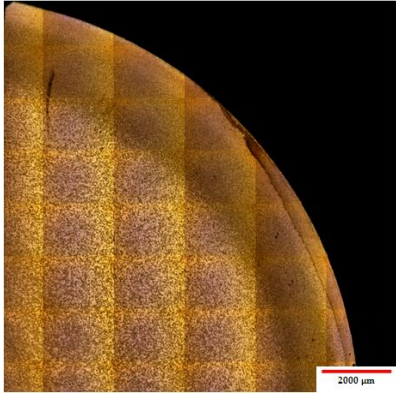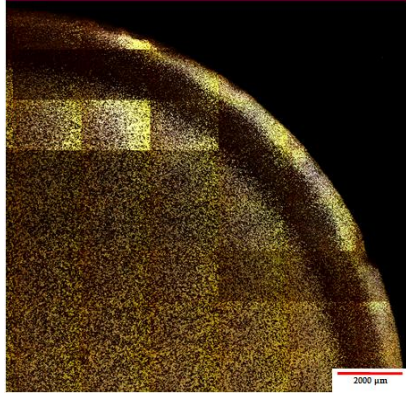
Figure 5.3 – Schematic of the sample regions: Surface, Sub-surface, ½ radius and Centre.

Details on the exit temperature of the extrudates (after exiting the quench) are provided for the 17:1 ER samples and for the 70:1 ER samples with extrusion temperature of 400°C and 500°C. No comments in this chapter will be provided with regards to the exit temperature as this will be discussed in more detail in chapter 6.

Homogenization of 8 h at 550°C, Ram Speed of 8 mm/s (17:1 ER):

Table 5.2, shows mosaics of optical micrographs of the transverse and longitudinal samples that were homogenized for 8 h at 550°C and extruded to an ER of 17:1 at a ram speed of 8 mm/s. The billets for these samples were heated to 400°C and 500°C. From the longitudinal sections it appears that the samples are unrecrystallized after extrusion. The grain structure is difficult to distinguish in these images, but it appears to be highly fibrous. The exact aspect ratio could not be determined from the images. A difference in the grain structure in the cross-sections is evident. The thickness of the fibers appears to decrease from the centre to the surface of the samples. In both cases there is also a difference in the structure at the sub-surface region. In the images this region is distinguished as a dark ring or band. It is difficult to conclude if this is a microstructural effect or whether it is a geometric effect introduced during the anodizing step of sample preparation.

Table 5.2 – Optical micrographs of anodized samples homogenized for 8 h at 550°C and extruded at a ram speed of 8 mm/s to an ER of 17:1. (Note: the reported temperatures were taken after extrusion using a hand held temperature probe).
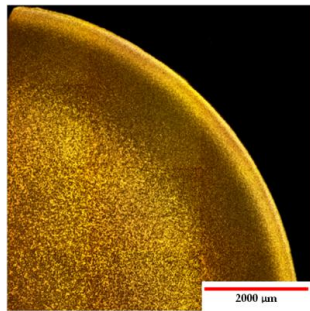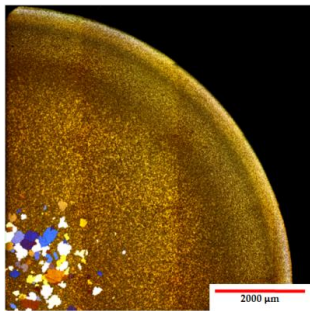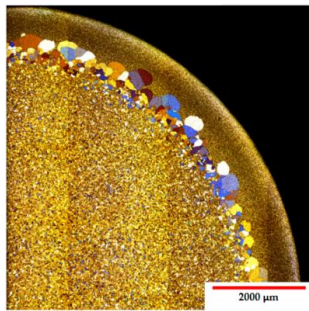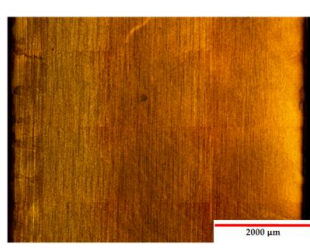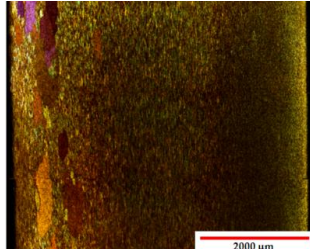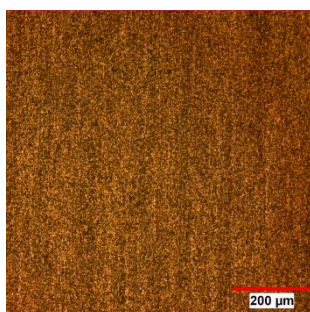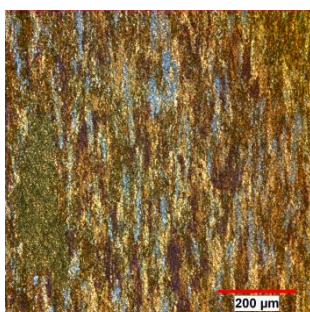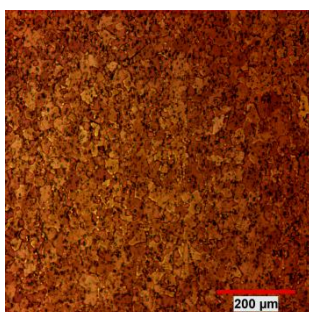
Transverse		
Longitudinal	 484°C	 521°C
Textrusion	**400°C**	**500°C**

Extrusion at 350°C (70:1 ER):

The 70:1 ER samples with extrusion temperature of 350°C and ram speed of 8 mm/s are shown in Table 5.3. As the homogenization soak time and temperature increase the extent of recrystallization increases; with a treatment of 24 h at 600°C providing the most uniformly recrystallized structure. There are fine equiaxed grains, with an approximate aspect ratio of 1.5:1 and grain size of approximately 20 µm by 45 µm, covering most of the cross-section of the 24 h at 600°C sample. The surface structure could not be characterized and the sub-surface has large tear drop shaped recrystallized grains with an aspect ratio of approximately 2.5:1. The grain size within the sub-surface region ranges in size from approximately 30 µm up to, and over, 860 µm in length and 280 µm in diameter.

The sample with a homogenization treatment of 8 h at 550°C shows partial recrystallization within the centre region. The recrystallized centre grains have an aspect ratio of approximately 5:1, and are surrounded by fibrous grains with aspect ratio of approximately 10:1. It is difficult to distinguish the structure at the sub-surface and surface as being either unrecrystallized or having undergone GDRX. Further analysis using EBSD is required.

Table 5.3 - Optical micrographs of anodized samples extruded at 350°C using a ram speed of 8 mm/s to an ER of 70:1. High magnification (100x) images correspond to the centre region.

		8 h at 500°C	8 h at 550°C	24 h at 600°C
Transverse	Low mag. (50x)			
Longitudinal	Low mag. (50x)			
	high mag. (100x)			
Homog.		8 h at 500°C	8 h at 550°C	24 h at 600°C

Extrusion at 400°C (70:1 ER):

Samples with extrusion temperature of 400°C and ER of 70:1 can be seen in Table 5.4. As the homogenization temperature and length of the treatment increase, the extent of recrystallization is also increased. This can be seen in the samples homogenized for 24h at 600°C. These 3 samples are almost all fully recrystallized. The one with the fastest ram speed (32 mm/s) is fully recrystallized and has a resultant grain size of approximately 30 µm and aspect ratio of 1:1. The 8 mm/s sample appears to be recrystallized through the structure except for at the sub-surface-surface boundary. At this boundary the extent of recrystallization is difficult to determine as the structure could not be resolved using optical microscopy. At the centre the structure is equiaxed with grains in the magnitude of 50 µm. The 2 mm/s sample is

fully recrystallized at the centre, ½ radius and surface, it is difficult to determine whether the sub-surface has recrystallized but there appears to be a very small grain size in this region. The grain size at the centre ranges from 30 µm by 30 µm to 215 µm by 95 µm. This corresponds to a range in aspect ratio from 1:1 to approximately 2.5:1.

Turning to the samples homogenized for 8 h at 550°C one can observe that the sample with ram speed of 2 mm/s is unrecrystallized. On the other hand, the sample with ram speed of 32 mm/s is close to being fully recrystallized. The surface consists of a mix of a fibrous structure closer to the sub-surface and what looks to be fine grains at the surface. The grain size through the profile increases from the centre to the sub-surface. The grain size at the centre is approximately 300 µm by 70 µm (~4:1 aspect ratio).

Finally, the samples homogenized for 8 h at 500°C samples with ram speed of 2 mm/s and 8 mm/s are unrecrystallized. There is a dark ring present at the sub-surface of the unrecrystallized samples. The state of recrystallization of this area could not be determined from these optical images. The sample with ram speed of 32 mm/s has a few recrystallized grains at the centre-1/2 radius boundary. The aspect ratio of these recrystallized grains ranges approximately from 6:1 to 8:1 (~280 µm by 2500 µm).

Extrusion at 500°C (70:1 ER):

In Table 5.5, we see the same trends that are present in Table 5.4. The 24 h at 600°C samples extruded at 500°C are all 70% to >95% recrystallized, with the grain size and aspect ratio decreasing as the ram speed increases. The samples with higher ram speed also experienced an increased extent of recrystallization. The aspect ratio for the 32mm/s sample is approximately 1:1, at the centre, with a range in grain size from 20 µm to 100 µm. The 8 mm/s sample is also fully recrystallized, but it has larger grains at the centre with an aspect ratio of 2.5:1 (approximately 285 µm in length by 110 µm in diameter). The 2 mm/s ram speed sample is a bit of an outlier in the sense that it is fully recrystallized at the surface, sub-surface, and ½ radius but not at the centre -where it still retains a fibrous structure. At the ½ radius region the grain size is approximately 710 µm by 160 µm (aspect ratio of ~4.5:1).

At a homogenization treatment of 8 h at 550°C, recrystallization is only clearly evident in the micrograph of the 32 mm/s ram speed sample. There are large recrystallized grains in this sample through the microstructure, with the centre being mostly recrystallized. The aspect ratio of these grains varies from 3:1 all the way to 8:1 (~2160 µm by 250 µm). The ½ radius region is approximately 50 to 70% recrystallized (by cross-sectional area), as is the sub-surface. The surface appears to have a highly fibrous structure, but the aspect ratio could not be determined. At the very surface of the sample the microstructure also contains sparse large grains. In the

Table 5.4 - Optical micrographs of anodized samples extruded to 70:1 ER at an extrusion temperature of 400°C. (Note: the reported temperatures were taken after extrusion using a hand held temperature probe).

Ram Speed (mm/s)		Transverse			Longitudinal		
32				531°C	520°C	518°C
8			✕	511°C	✕	500°C
2				460°C	459°C	460°C
Homog.		8 h at 500°C	8 h at 550°C	24 h at 600°C	8 h at 500°C	8 h at 550°C	24 h at 600°C
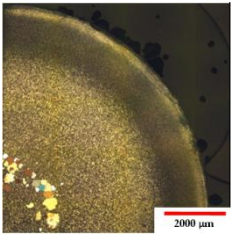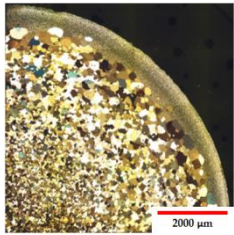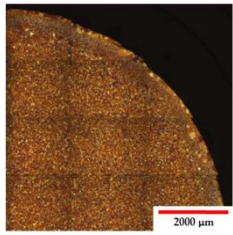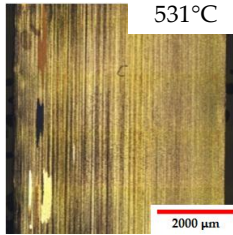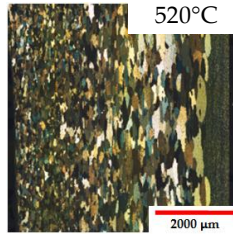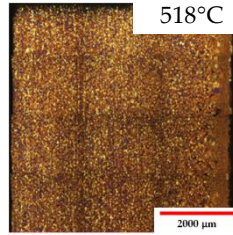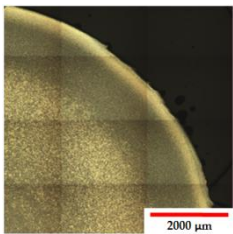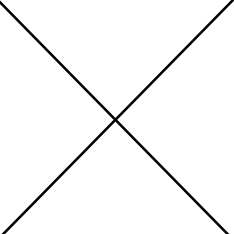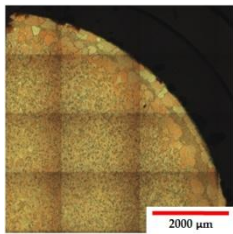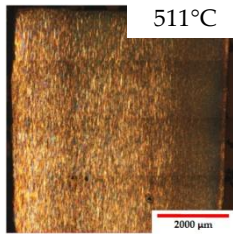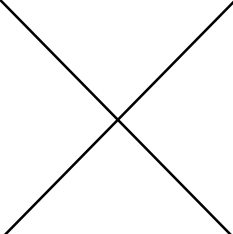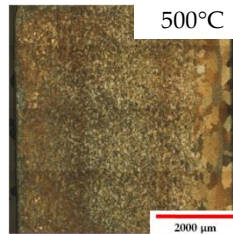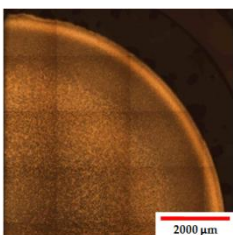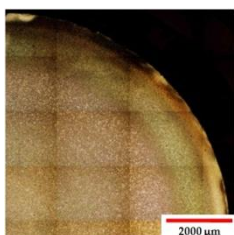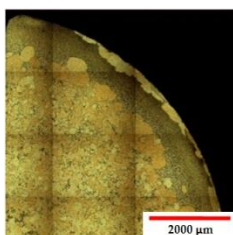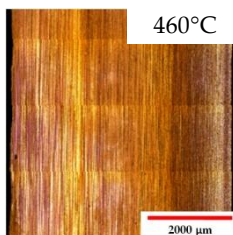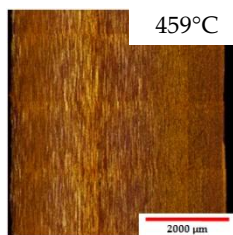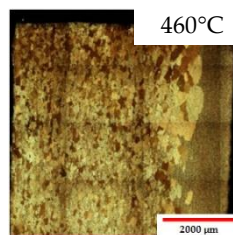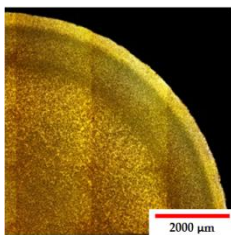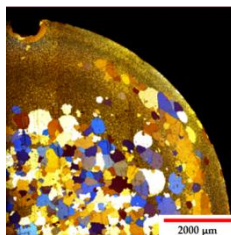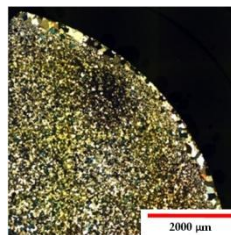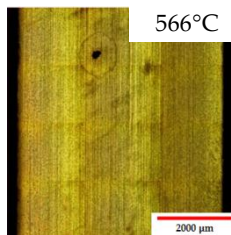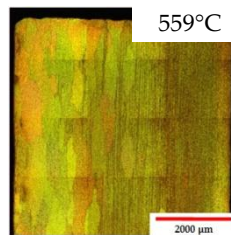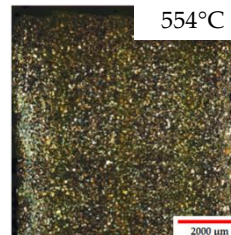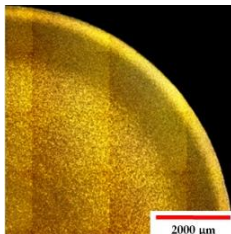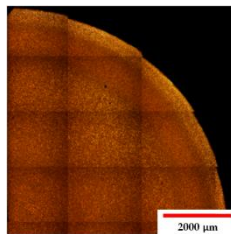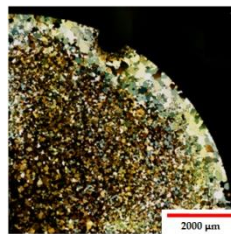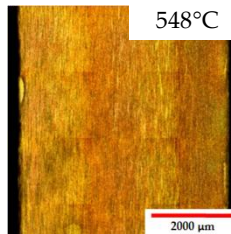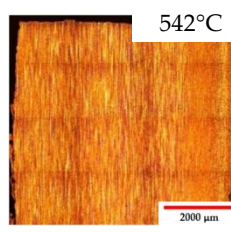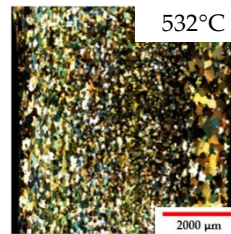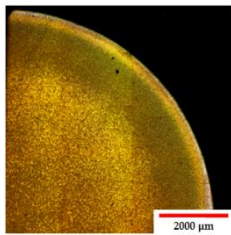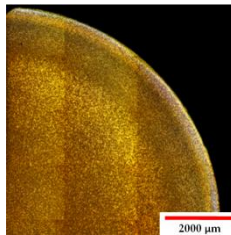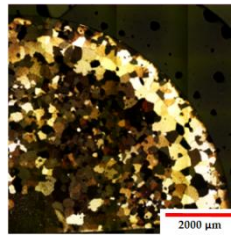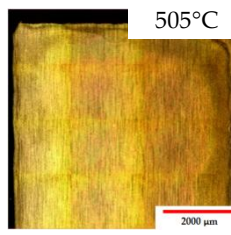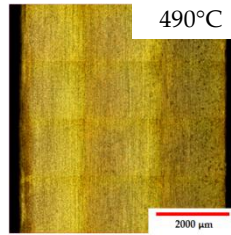
Table 5.5 - Optical micrographs of anodized samples extruded to 70:1 ER at an extrusion temperature of 500°C. (Note: the reported temperatures were taken after extrusion using a hand held temperature probe).

Ram Speed (mm/s)							
32				566°C	559°C	554°C	
8				548°C	542°C	532°C	
2				505°C	490°C	497°C	
Homog.	8 h at 500°C	8 h at 550°C	24 h at 600°C	8 h at 500°C	8 h at 550°C	24 h at 600°C	
	Transverse			Longitudinal			
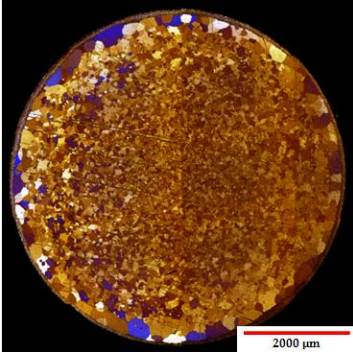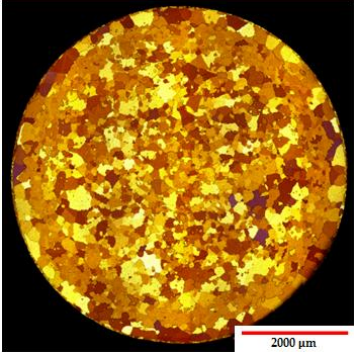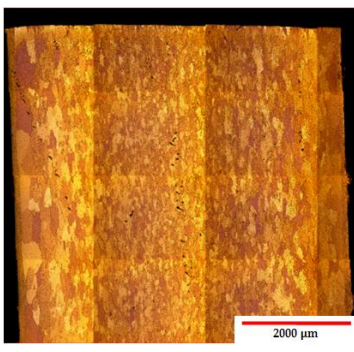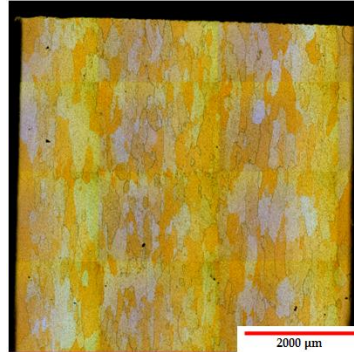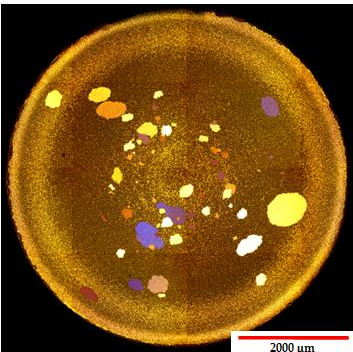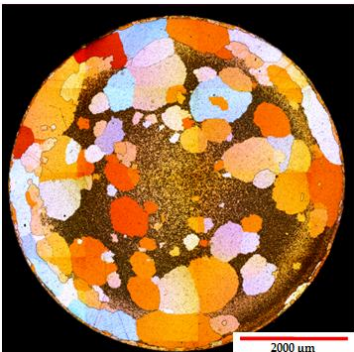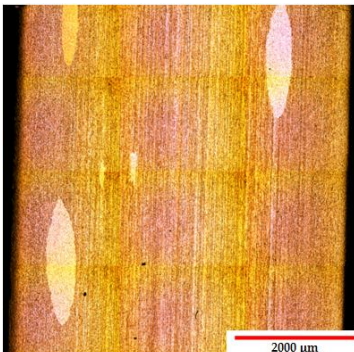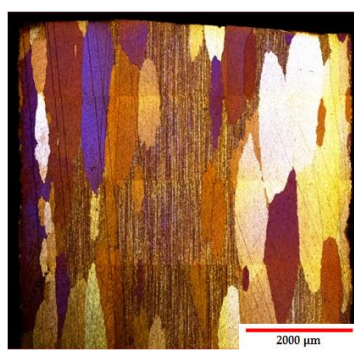
8 mm/s ram speed sample, with homogenization treatment of 8 h at 550°C, the structure is highly fibrous, but in higher magnification optical micrographs there is some evidence that recrystallization may have begun as there are a few recrystallized grains throughout the radius of the structure. All the samples homogenized for 8 h at 500°C appear to be fully unrecrystallized.

Homogenization of 8 h at 550°C (280:1 ER):

The optical micrographs in Table 5.6 are of samples homogenized for 8 h at 550°C, which have been extruded to a ratio of 280:1 with either an extrusion temperature of 400°C or 500°C, and ram speed of 2 mm/s or 8 mm/s.

The micrographs for an extrusion temperature of 400°C show two different results. Firstly, a ram speed of 2 mm/s results in a mostly unrecrystallized structure with a small number of larger grains with high aspect ratio (~5:1) and large grain size within the ½ radius region (~2100 μm by 450 μm). Secondly, the higher ram speed results in a fully recrystallized structure. The fully recrystallized structure contains very fine grains at the surface and sub-surface, followed by grains of 200 μm in diameter within the ½ radius region and 110 μm in diameter with low aspect ratio at the centre. A similar trend of small recrystallized grains at the surface, followed by a layer of large grains and then more equiaxed grains has also been reported by Mahmoodkhani et al. [64] (for an I-beam with an extrusion ratio of 130:1, ram speed of 14 mm/s, extrusion temperature of 400°C and homogenization treatment of 8 h at 550°C). A similar trend is also evident in Table 5.6 for the 280:1 ER samples homogenized for 8 h at 550°C, and extruded at 500°C. As the ram speed increases the extent of recrystallization increases, the structure is finer and has a low aspect ratio. The 8 mm/s ram speed samples are both recrystallized and have varying grain structures through the profile, but it can be seen that the sample with the lower extrusion temperature has a finer structure with a decreased aspect ratio.

Table 5.6 - Optical micrographs of anodized samples homogenized for 8 h at 550°C, and extruded to 280:1 ER.

Ram Speed (mm/s)				
8				
2				
$T_{extrusion}$	400°C	500°C	400°C	500°C
	Transverse		Longitudinal	

5.3.2 Summary

- Both of the 17:1 ER samples appear unrecrystallized, but the fibrous grain structure was difficult to resolve from the optical micrographs. This was also true for all 'unrecrystallized' structures.
- In many of the unrecrystallized structure a dark band in the sub-surface region was noted. This microstructure within this band could not be resolved from optical micrographs.
- Many samples exhibited a fine grain layer in the surface region.
- All samples homogenized for 24 h at 600°C experienced close to 100% recrystallization independent of extrusion temperature and ram speed.
- As the ram speed and the extent of homogenization increased the resultant as-extruded grain structure was more equiaxed and refined.
- A higher extrusion temperature resulted in a higher extent of recrystallization.

5.3.3 Unrecrystallized Grain Thickness

The average 3-D grain thickness of 'unrecrystallized' extruded material was measured using EBSD IPF maps as described in chapter 4.6. Figure 5.4 to Figure 5.7 show examples of some of the cleaned EBSD IPF maps used for calculating the average 2-D grain thickness for 17:1 ER and 70:1 ER and their corresponding Image Quality (IQ) maps. The results for all of the analyzed samples are summarized in Table 5.7.

When the EBSD data was being processed for the sample with ER of 280:1 it was noticed that the 'unrecrystallized' region was partially recrystallized. For this reason the data for the sample was not included in any further analysis of unrecrystallized grain size. The 17:1 ER sample with extrusion temperature of 400°C, was also left out of further analysis as the measured average grain size of 11.6 μm is much smaller than what would be expected from a simple geometric approximation using the initial grain size and ER. A sensitivity analysis was conducted (Appendix C) on the procedure in order to determine if the resultant average grain thickness discrepancy could be attributed to the grain thickness procedure.
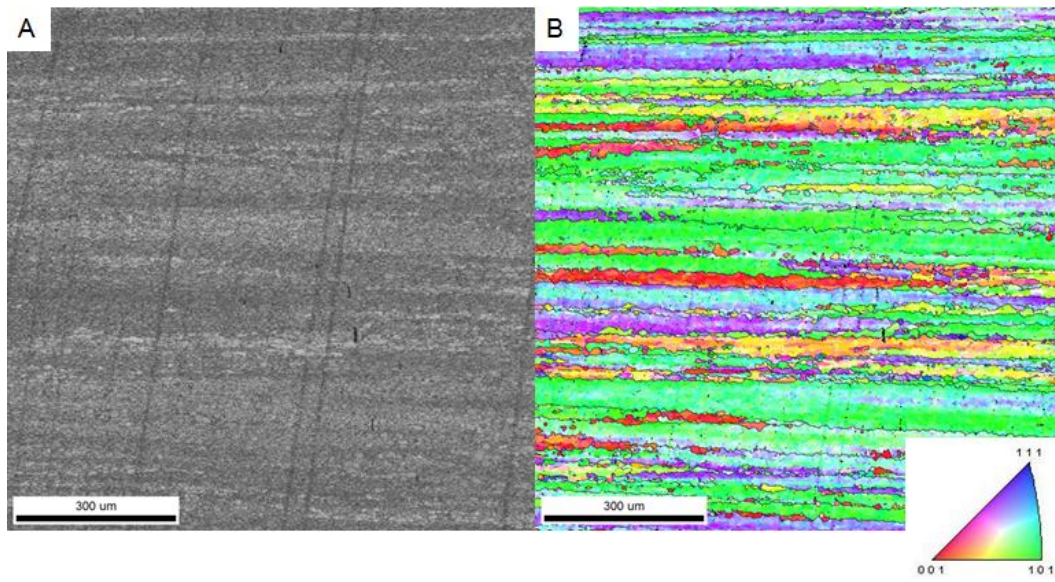
Figure 5.4 – EBSD (a) IQ and (b) IPF maps for 17:1 ER, homogenization of 8 h at 550°C, extrusion temperature of 500°C and ram speed of 8 mm/s.
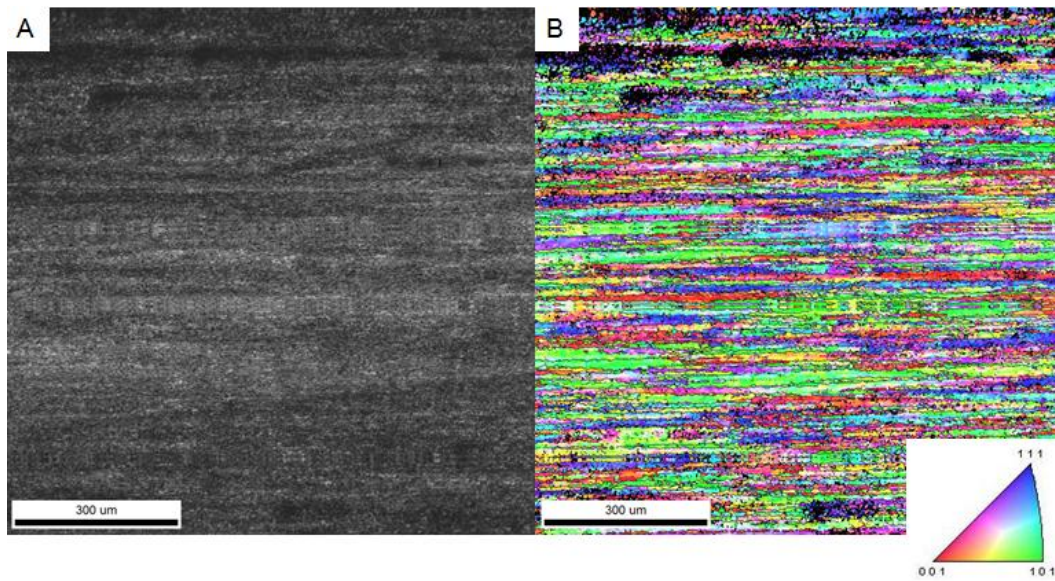
Figure 5.5 - EBSD (a) IQ and (b) IPF maps for 70:1 ER, homogenization of 8 h at 500°C, extrusion temperature of 500°C and ram speed of 2 mm/s.
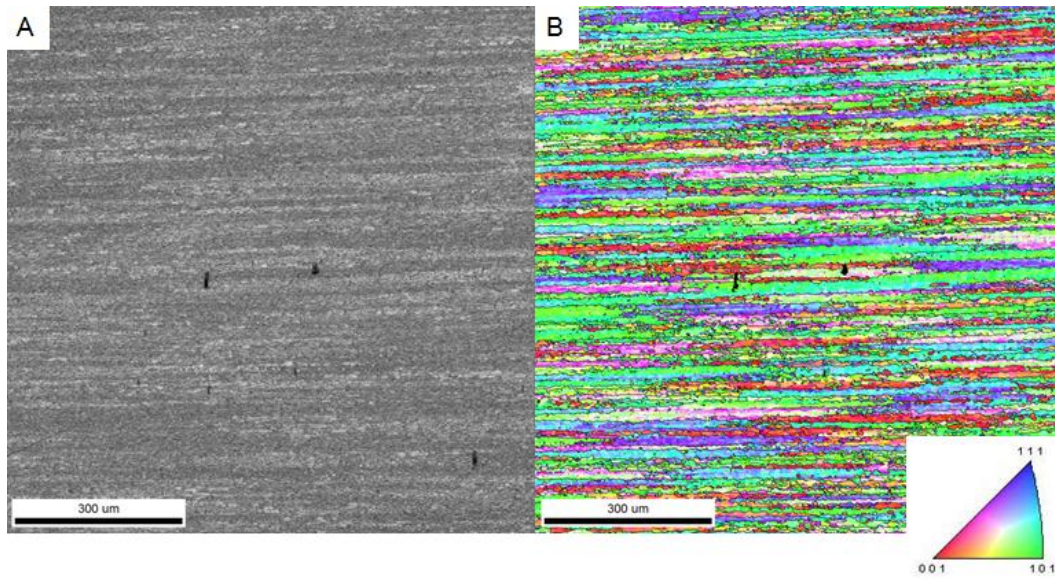
Figure 5.6 - EBSD (a) IQ and (b) IPF maps for 70:1 ER, homogenization of 8 h at 500°C, extrusion temperature of 500°C and ram speed of 8 mm/s.
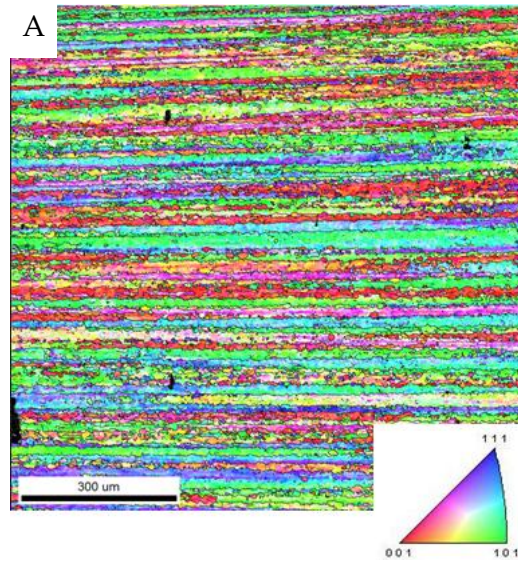
Figure 5.7 - EBSD IPF map for 70:1 ER, homogenization of 8 h at 500°C, extrusion temperature of 500°C and ram speed of 32 mm/s.

Table 5.7 – Experimental average 2-D grain thickness and corrected 3-D average grain thickness results from EBSD data.

Extrusion ratio	Homogenization treatment	$T_{extrusion}$ (°C)	Ram speed, v_{ram} (mm/s)	Average 2-D grain thickness, (µm)	Average 3-D grain thickness, (µm)
17:1	8 h at 550°C	400	8	9.7	11.6*
17:1	8 h at 550°C	500	8	15.5	18.6
70:1	8 h at 500°C	350	8	5.7	6.8
70:1	8 h at 500°C	400	2	6.8	8.2
70:1	8 h at 500°C	400	8	6.7	8.0
70:1	8 h at 500°C	500	2	7.4	8.9
70:1	8 h at 500°C	400	32	5.7	6.8
70:1	8 h at 500°C	500	8	7.3	8.8
70:1	8 h at 500°C	500	32	8.6	10.3
70:1	8 h at 550°C	350	8	6.6	7.9
70:1	8 h at 550°C	400	2	6.8	8.2
70:1	8 h at 550°C	500	2	7.4	8.9
70:1	8 h at 550°C	500	8	8.3	10.0
280:1	8 h at 550°C	400	2	5.3	6.4*

*This data was not used in further analysis.

5.3.4 Constituent Particle Distribution

The as-extruded micrographs for two samples showed an unusual result where some large recrystallized grains were observed at the boundary between the centre and the ½ radius region of the extrudates (please refer to Table 5.8 for the sample condition details). The grains found in this section are generally large (>100 µm) and have a large aspect ratio (>4:1). Therefore a more in depth investigation was conducted on the structure of two of these samples. It has been noted by Geng [4] and noticed here that constituent particles align preferentially along the extrusion direction. It has also been reported by Geng that there are variations in the through cross-section of the sample as the centre of extrudate undergoes a different thermo-mechanical history than the ½ radius, sub-surface and surface regions. Therefore all of these regions were investigated to search for differences in the distribution of constituent particles.

The samples chosen for further analysis both have a 70:1 ER. The first was homogenized for 8 h at 500°C, and extruded at 400°C with a ram speed of 32 mm/s (Top left micrograph of

Table 5.4). The second was homogenized for 8 h at 550°C, and extruded at 350°C with a ram speed of 8 mm/s (Centre micrograph of Table 5.3). A quantitative measurement of the number density and area fraction of constituent particles for both samples (Table 5.8) was conducted using the OM images of the HF etched samples (described in chapter 4.5.6). Figure 5.8 shows the through profile OM images of the HF etched sample 1. From the micrographs it is difficult to even make qualitative conclusions regarding differences in the aspect ratio and density of the particles. The main thing noted was that the particles appear to be larger at the surface and decrease in size as one moves out to the surface of the extrudate. Details regarding quantitative results gathered using Clemex software can be found in chapter 4.5.6 and Appendix B.

Table 5.8 – Constituent particle sample identification.

Extrusion Ratio	Homogenization treatment	Extrusion Temperature, $T_{extrusion}$ (°C)	Ram Speed, v_{ram} (mm/s)	Sample #
70:1	8 h at 500°C	400	32	**1**
70:1	8 h at 550°C	350	8	**2**

Figure 5.9 (a) shows the data for the mean aspect ratio, for both samples, from the centre out to the surface. In general the mean aspect ratio of sample 2 (8 h at 550°C) is lower than that of sample 1 (8 h at 500°C) by approximately 10%. In both cases the mean aspect ratio is greatest at the centre and decreases along the cross-section leveling off at the sub-surface (sample 1) or continuing to decrease until the surface (sample 2). The overall mean aspect ratio through the structures is approximately 2:1. The number density (Figure 5.9 (b)) was found to be greater in sample 2, but both samples followed the same trend. The largest density is at the sub-surface and surface regions, followed by the centre and ½ radius regions. The range of number density seen here is from 0.013 to 0.024 particles/μm^2, which is consistent with Geng [4] whom reported values in the range of 0.017 to 0.024 particles/μm^2 for a sample homogenized for 24 h at 600°C and extruded at 400°C. The circular radius for the samples was found to be approximately 0.70 μm for sample 2 (8 h at 550°C) throughout the entire profile. The circular radius for sample 1 (8 h at 500°C) was highest near the centre, 0.88 μm, and lowest near the surface, 0.68 μm. Once again these values are consistent with Geng's [4] findings for samples homogenized for 8 h at 500°C and 8 h at 550°C and extruded at 400°C, in which Geng reported the circular radii as being approximately 0.5 to 0.6 μm, respectively. Geng also reports an extruded area fraction for various homogenization conditions and extrusion at 400°C, being within the range of 3.25 to 4%. In this analysis the area fraction for sample 2 showed little variation throughout the various

regions. The area fraction was 3.5% at the surface, 3.5% at the ½ radius and 3.2% at the centre, whereas sample 1 was 3% at the surface and increased to 3.9% at the centre.

(a)   (b)

(c)   (d)
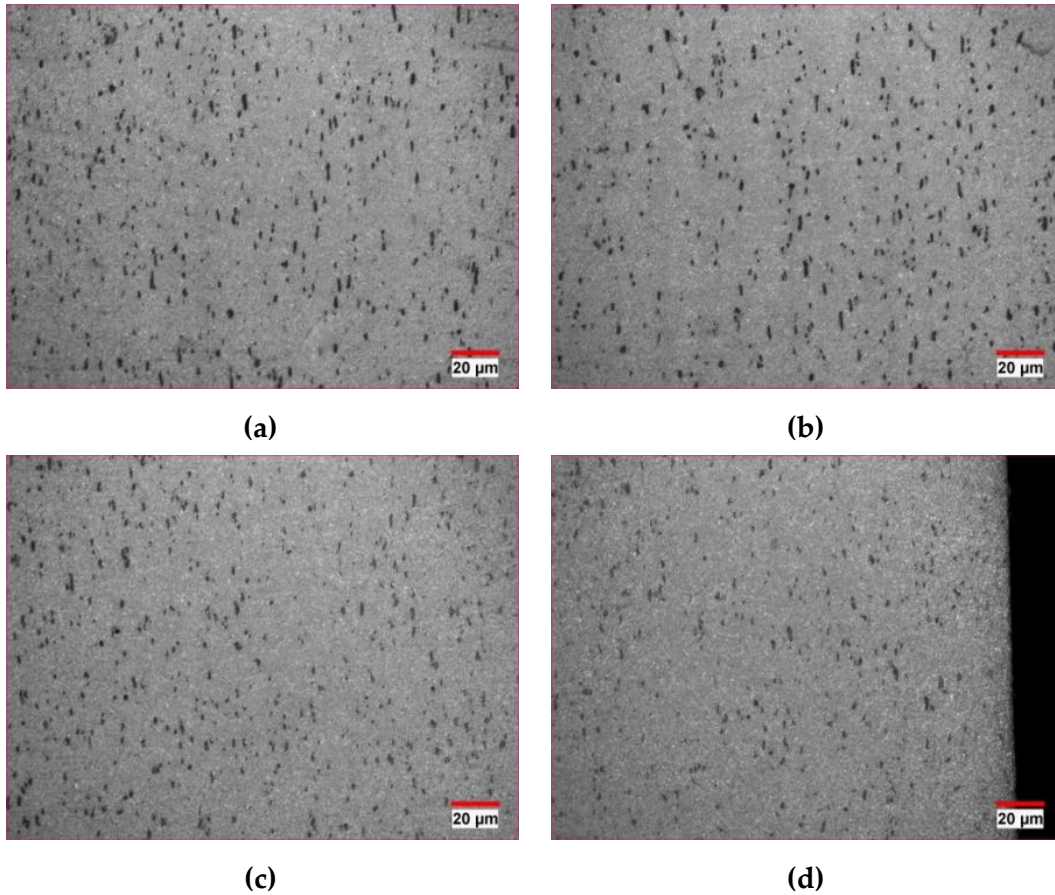
Figure 5.8 - 500x optical micrographs of a 70:1 ER sample homogenized for 8 h at 500°C, extruded using a ram speed of 32 mm/s at a temperature of 400°C, etched using 0.5% HF for 60 s: (a) centre, (b) ½ radius, (c) sub-surface and (d) surface.
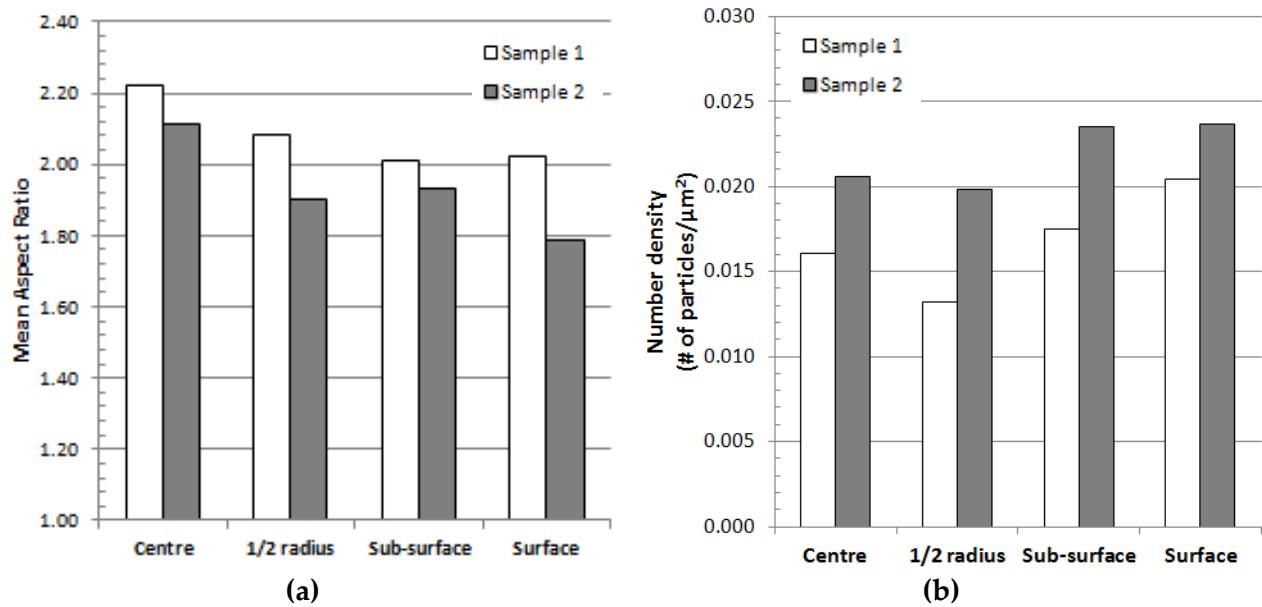
Figure 5.9 – (a) Mean precipitate aspect ratio and (b) Precipitate number density results (see Table 5.8 for the definition of sample #1 and #2).

5.3.5   Post-Extrusion Annealing Microstructure

Post-extrusion annealing was conducted on samples which appeared to have a highly fibrous unrecrystallized structure, from anodized optical images, after extrusion. These samples were annealed in a nitrate salt bath as described in chapter 4.2. Table 5.9 summarizes the post-extrusion annealing tests conducted on 14 unrecrystallized samples. This test was conducted to determine if the Zener pinning pressure in the system was high enough to retard recrystallization from occurring, or just high enough to impede nucleation during recrystallization, i.e. only a few viable nuclei are produced resulting in very large recrystallized grain size. In most cases the post-extrusion annealing results indicate that recrystallization is possible after extrusion. There were 3 cases in which recrystallization did not occur, and one case in which minimal recrystallization (<15%) occurred (after 10 min. at 550°C). These samples had extrusion ratios of 17:1 and 70:1 with homogenization treatments of 8 h at 550°C and 8 h at 500°C, respectively, and extrusion temperature of 500°C. The ram speeds ranged from 2 mm/s to 32 mm/s and are depicted in Figure 5.10.

Table 5.9 – Post-extrusion annealing test summary (Note: unRx = unrecrystallized, and the percentages reported are the percent recrystallized based on area measurements from optical micrographs of anodized samples).

Extrusion ratio	Homogenization treatment	Extrusion Temperature, $T_{extrusion}$ (°C)	Ram Speed, v_{ram} (mm/s)	As-extruded	500°C			525°C			550°C	
					1 min.	10 min.	100 min.	1 min.	10 min.	100 min.	1 min.	10 min.
17:1	8 h at 550°C	400	8	unRx	--	--	--	--	~35%	~40%	>95%	>95%
17:1	8 h at 550°C	500	8	unRx	--	--	--	--	unRx	unRx	--	unRx
70:1	8 h at 500°C	350	8	unRx	unRx	--	--	~20%	--	--	>85%	>90%
70:1	8 h at 500°C	400	2	unRx	--	--	--	--	unRx	--	--	>85%
70:1	8 h at 500°C	400	8	unRx	--	--	unRx	--	~20%	--	~45%	>95%
70:1	8 h at 500°C	400	32	~5%	--	--	~25%	~35%	--	--	>80%	>95%
70:1	8 h at 500°C	500	2	unRx	--	--	unRx	unRx	--	--	unRx	unRx
70:1	8 h at 500°C	500	8	unRx	--	--	unRx	unRx	--	--	unRx	unRx
70:1	8 h at 500°C	500	32	unRx	--	<5%	unRx	unRx	--	--	unRx	~15%
70:1	8 h at 550°C	350	8	~10%	~50%	>90%	>90%	>95%	--	--	--	--
70:1	8 h at 550°C	400	2	unRx	unRx	--	<5%	~25%	>90%	--	~20%	>95%
70:1	8 h at 550°C	500	2	unRx	--	--	unRx	unRx	--	--	~5%	>95%
70:1	8 h at 550°C	500	8	unRx	--	--	--	--	unRx	<5%	--	~55%
280:1	8 h at 550°C	400	2	~5%	30%	>95%	--	>95%	--	--	--	--
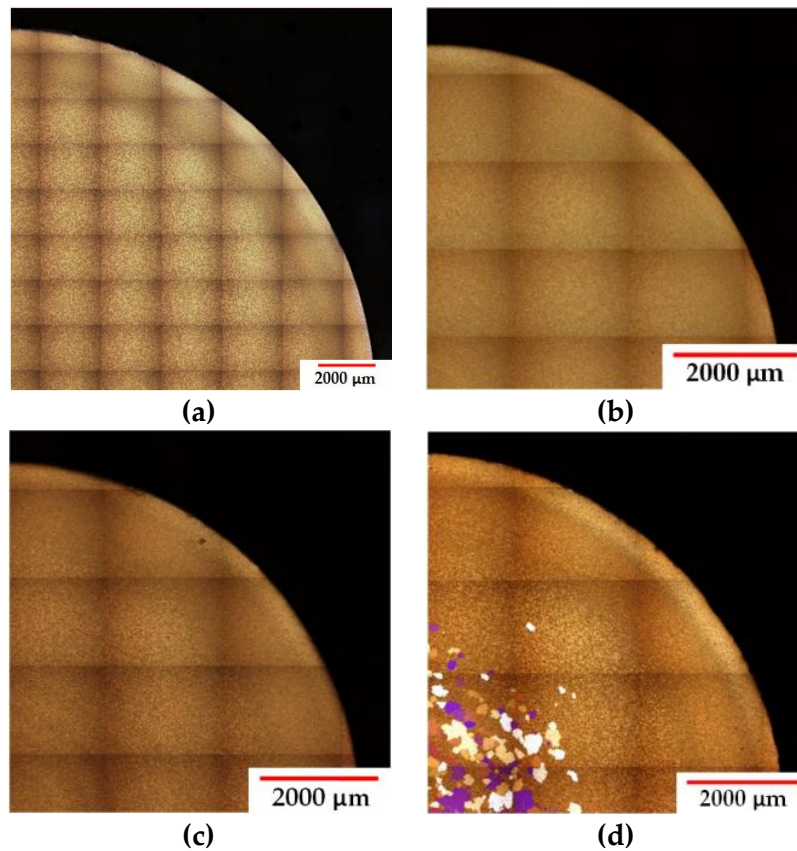
Figure 5.10 – Transverse optical micrographs of anodized samples illustrating the effect of post-extrusion annealing for 10 min. at 550°C on samples extruded at 500°C: (a) 17:1, 8 h at 550°C and ram speed of 8 mm/s and 70:1, 8 h at 500°C samples extruded using a ram speed of (b) 2 mm/s, (c) 8 mm/s and (d) 32 mm/s.

Although there were a few samples that did not recrystallize (shown in Figure 5.10) within the test conditions listed in Table 5.9, the rest of the samples experienced some extent of recrystallization, with a large number of them reaching an extent of >95% recrystallized. The resultant recrystallized grain morphology was different in the post-extrusion annealing samples as compared to the samples that were recrystallized after extrusion. The post-extrusion annealing samples resulted in large grains with very high aspect ratios, as seen in Figure 5.11. Figure 5.11 (a) shows a 70:1 ER sample which has been homogenized for 8 h at 500°C and extruded at 400°C using a ram speed of 32 mm/s. The as-extruded grain structure is highly fibrous in all regions except for a ring of large grains with high aspect ratio near the border of the centre and ½ radius regions. Once this sample has undergone post-extrusion annealing at 500°C for 100 min. (Figure 5.11 (b)) the resultant structure at the centre region is close to 100% recrystallized, with much larger high aspect ratio grains (greater than 10:1), than in the as-extruded state.
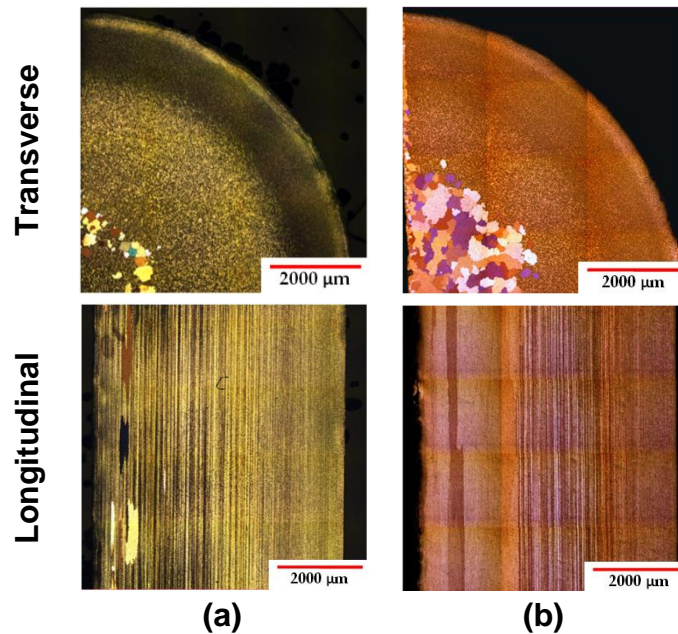
Figure 5.11 – Optical micrographs of anodized 70:1 ER samples homogenized for 8 h at 500°C and extruded using an extrusion temperature 400°C and ram speed of 32 mm/s: (a) as-extruded, (b) post-extrusion annealing at 500°C for 100 min..

The post-extrusion annealing results indicate that, in most cases, recrystallization is possible after extrusion. The resultant grains in the post-extrusion annealing microstructures are large, as compared to the as-extruded structure, and have a large aspect ratio with minimal variation along the radius of the samples.

5.4 Resistivity

The as-cast billet resistivity at locations 1, 2 and 3 (Figure 4.10) was found to be 62.5, 61.6, and 62.5 nΩm, respectively, using a frequency of 60 kHz (as mentioned in chapter 5.2). After the billets were homogenized these values decreased to 44.0, 44.7, and 47.3 nΩm (60 kHz) for homogenization treatment of 8 h at 500°C, 8 h at 550°C, and 24 h at 600°C, respectively. These measurements were all taken using a hand held 8 mm Eddie current probe (Sigmatest® 2.069) and the procedure outlined in chapter 4.4. Table 5.10 tracks the change in resistivity from the homogenized state to the as-extruded state. The change in resistivity between the homogenized and as-extruded states is small, with the difference being between a 3% drop and an increase of approximately 4%. The resistivity change for high temperature compression samples was found to be approximately 3% (please refer to Appendix A). This suggests there is relatively little change in the solid solution during or after deformation. This is also the case for the post extrusion annealing test samples (Table 5.11), where the change in resistivity ranged from approximately -4% to 2% for post-extrusion annealing of 10 min. at 550°C.

Table 5.10 – Resistivity data for homogenized (ρ_{homo}) and as-extruded ($\rho_{extruded}$) samples.

Extrusion ratio	Homogenization treatment	Extrusion Temperature, $T_{extrusion}$ (°C)	Ram Speed, v_{ram} (mm/s)	ρ_{homo} (nΩm)	$\rho_{extruded}$ (nΩm)	Δρ (extruded-homo) (nΩm)	Change (%)
17:1	8 h at 550°C	400	8	44.7	43.5	-1.3	-2.8
17:1	8 h at 550°C	500	8	44.7	43.4	-1.3	-2.9
70:1	8 h at 500°C	350	8	44.0	44.2	0.2	0.4
70:1	8 h at 500°C	400	2	44.0	43.4	-0.6	-1.4
70:1	8 h at 500°C	400	8	44.0	43.7	-0.3	-0.6
70:1	8 h at 500°C	400	32	44.0	43.8	-0.1	-0.3
70:1	8 h at 500°C	500	2	44.0	43.2	-0.8	-1.8
70:1	8 h at 500°C	500	8	44.0	45.4	1.4	3.1
70:1	8 h at 500°C	500	32	44.0	44.4	0.4	0.9
70:1	8 h at 550°C	350	8	44.7	43.5	-1.3	-2.9
70:1	8 h at 550°C	400	2	44.7	43.6	-1.1	-2.6
70:1	8 h at 550°C	400	32	44.7	44.3	-0.5	-1.1
70:1	8 h at 550°C	500	2	44.7	43.0	-1.8	-3.9
70:1	8 h at 550°C	500	8	44.7	43.3	-1.5	-3.3
70:1	8 h at 550°C	500	32	44.7	44.1	-0.6	-1.4
70:1	24 h at 600°C	350	8	47.3	48.3	1.0	2.2
70:1	24 h at 600°C	400	2	47.3	46.3	-1.0	-2.0
70:1	24 h at 600°C	400	8	47.3	46.0	-1.3	-2.7
70:1	24 h at 600°C	400	32	47.3	48.0	0.7	1.5
70:1	24 h at 600°C	500	2	47.3	45.5	-1.8	-3.7
70:1	24 h at 600°C	500	8	47.3	46.1	-1.1	-2.4
70:1	24 h at 600°C	500	32	47.3	46.9	-0.4	-0.8

Table 5.11 - Resistivity data for as-extruded ($\rho_{extruded}$) and post-extrusion annealing (ρ_{anneal}).

Extrusion ratio	Homogenization treatment	Extrusion Temperature, $T_{extrusion}$ (°C)	Ram Speed, v_{ram} (mm/s)	$\rho_{extruded}$ (nΩm)	ρ_{anneal} (nΩm)	Δρ (anneal-extruded) (nΩm)	Change (%)
17:1	8 h at 550°C	400	8	43.5	44.5	1.0	2.2
17:1	8 h at 550°C	500	8	43.4	42.8	-0.6	-1.4
70:1	8 h at 500°C	350	8	44.2	44.5	0.3	0.7
70:1	8 h at 500°C	400	2	43.4	42.9	-0.4	-1.0
70:1	8 h at 500°C	400	8	43.7	44.6	0.9	2.0
70:1	8 h at 500°C	400	32	43.8	44.4	0.6	1.4
70:1	8 h at 500°C	500	2	43.2	43.8	0.6	1.4
70:1	8 h at 500°C	500	8	45.4	43.5	-1.9	-4.1
70:1	8 h at 500°C	500	32	44.4	43.9	-0.5	-1.2
70:1	8 h at 550°C	350	8	43.5	42.2	-1.3	-2.9
70:1	8 h at 550°C	400	2	43.6	42.9	-0.7	-1.6*
70:1	8 h at 550°C	500	2	43.0	42.5	-0.5	-1.1
70:1	8 h at 550°C	500	8	43.3	42.9	-0.4	-0.8

Note: All post-extrusion annealing measurements are for 10 min. at 550°C.

' * ' This value is for 1 min. at 525°C.

5.5 High Temperature Compression Tests

High temperature compression tests were conducted using the Gleeble® 3500 Thermo-mechanical Simulator as described in chapter 4.3. In total 17 tests were conducted at temperature of 500°C and strain rates ranging from 1 s^{-1} to 10 s^{-1}, using samples that had been homogenized for 24 h at 600°C (low to no dispersoids density). Tests were also conducted using a constant strain rates (i.e. 1 s^{-1} and 10 s^{-1}) and transitional strain rate changes. The transitional strain rate tests involved transitioning from a strain rate of 1 s^{-1} to 10 s^{-1} from 0.2 to 0.4 strain, 0.2 to 0.3 strain, and 0.2 to 0.25 strain for a gradual, moderate and rapid transition, respectively. A shorter transition, than 0.2 to 0.25 strain, which would be more relevant for industry, could not be investigated due to limitations with the testing set-up. The goal of these tests was to investigate the effect of the strain rate path on the final steady-state flow stress (i.e. flow stress) for the system. Chapter 4.3 describes how the data was processed and how the flow stress, and yield stress were determined. Detailed results for the various tests can also be found in Appendix A along with resistivity data.

The first test conducted was a constant strain rate test at 1 s^{-1} in order to compare with Kubiak's work [5], and check the reproducibility of the results. Figure 5.12 shows the stress strain curve from Kubiak, against the new test data for a constant strain rate of 1 s^{-1}. The new data is consistent with the previous data, and the steady-state flow stress is found to be approximately 27 MPa. Figure 5.13, shows the stress-strain data collected for the 10 s^{-1} constant strain rate tests. This test was replicated 4 times giving an average flow stress of 37.7 MPa and a standard deviation of 1.43 MPa.
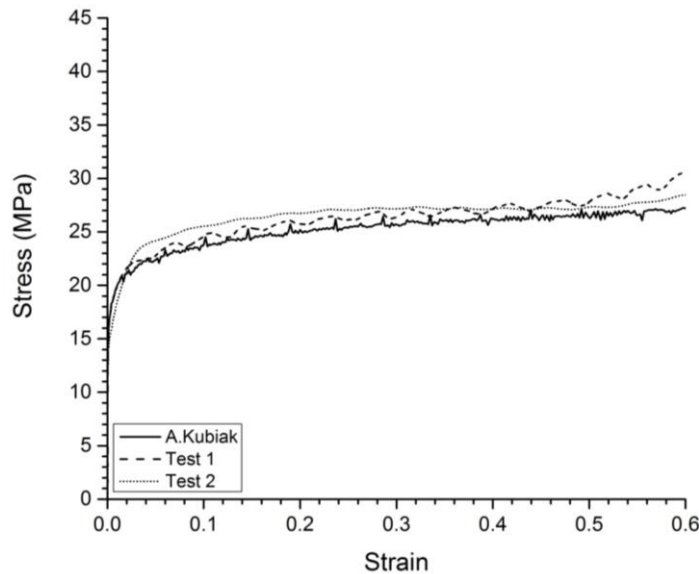
Figure 5.12 – Stress-strain curves for samples homogenized for 24 h at 600°C, deformed at 500°C at a constant strain rate of 1 s^{-1}.
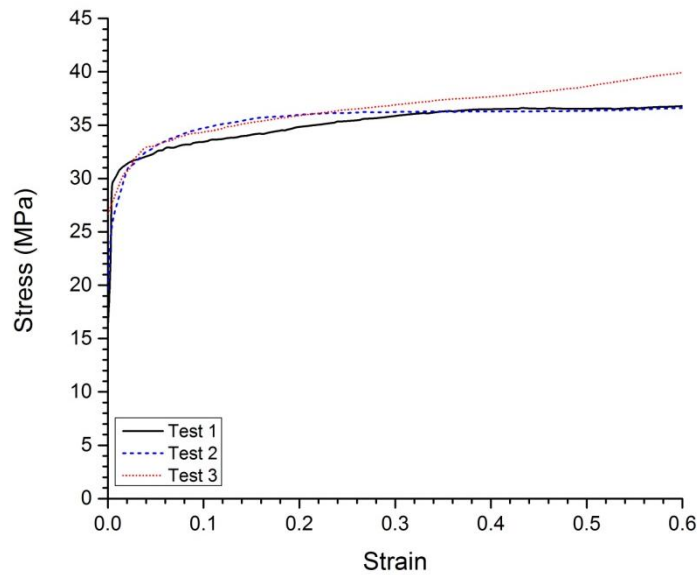
Figure 5.13 - Stress-strain curves for samples homogenized for 24 h at 600°C, deformed at 500°C at a constant strain rate of 10 s⁻¹.

Figure 5.14 shows the stress-strain curves for a gradual transition strain rate from a strain of 0.2 to 0.4. These tests were a little more difficult to duplicate, with 3 tests, resulting in an average flow stress of 37.9 MPa and a standard deviation of 2.34 MPa. This transitional test produced the largest range in the flow stress data. It should also be noted that even after a strain of 0.6 the stress-strain curves do not flatten out to reach a "steady-state flow stress". The moderate strain rate transition test (Figure 5.15) was also conducted numerous times. This test was the test with the best reproducibility of the transition test, having a standard deviation of only 0.90 MPa. The average flow stress for these results is 36.9 MPa. These test conditions were found to result in stress-strain curves that approach a "steady-state flow stress" more closely than the gradual transition test. The rapid strain rate test results show an average flow stress of 39.2 MPa. This can be seen in Figure 5.16, in which two of the tests (Test 1 and Test 2) show a flow stress of approximately 40 MPa, and test 3 has a flow stress of 37.6 MPa. It should also be noted that the samples with a higher flow stress do not reach a "steady-state flow stress", whereas the one with a lower flow stress (Test 3) appears to flatten out (reaches a region of steady-state flow stress) and then begins to decrease as the test approaches a strain of 0.6.
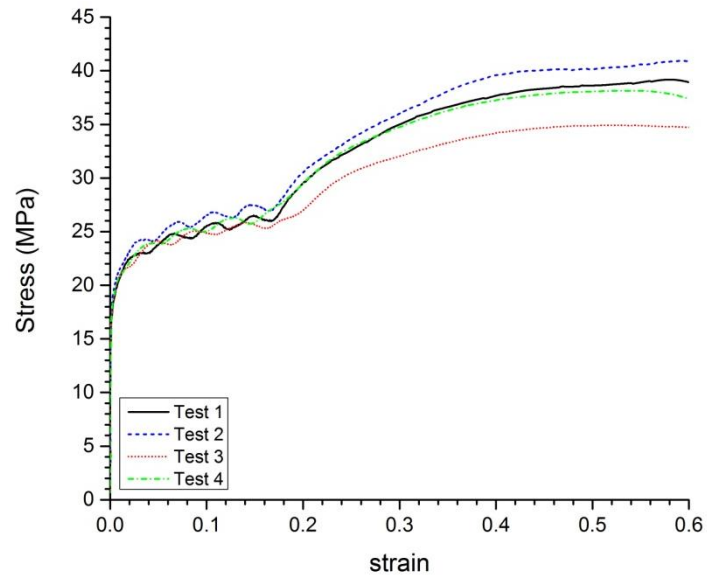
Figure 5.14 - Stress-strain curves for samples homogenized for 24 h at 600°C, deformed at 500°C. Gradual (ε = 0.2 to 0.4) strain rate transition from 1 s⁻¹ to 10 s⁻¹.
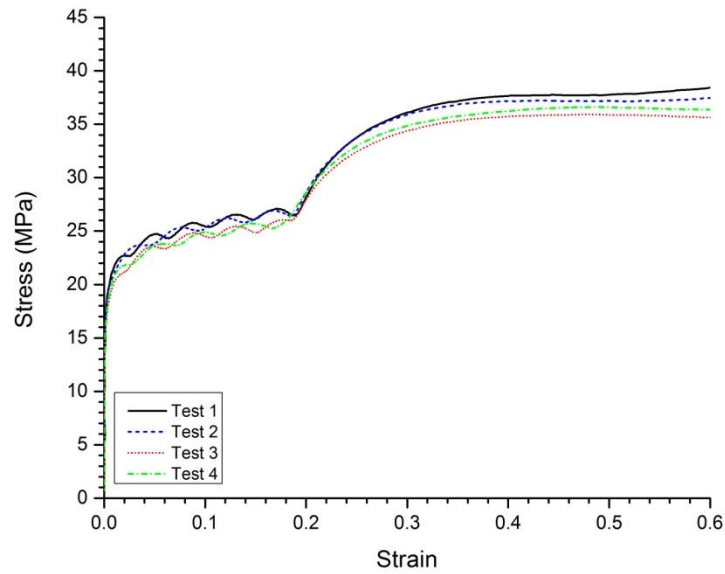
Figure 5.15 - Stress-strain curves for samples homogenized for 24 h at 600°C, deformed at 500°C. Moderate (ε = 0.2 to 0.3) strain rate transition from 1 s⁻¹ to 10 s⁻¹.
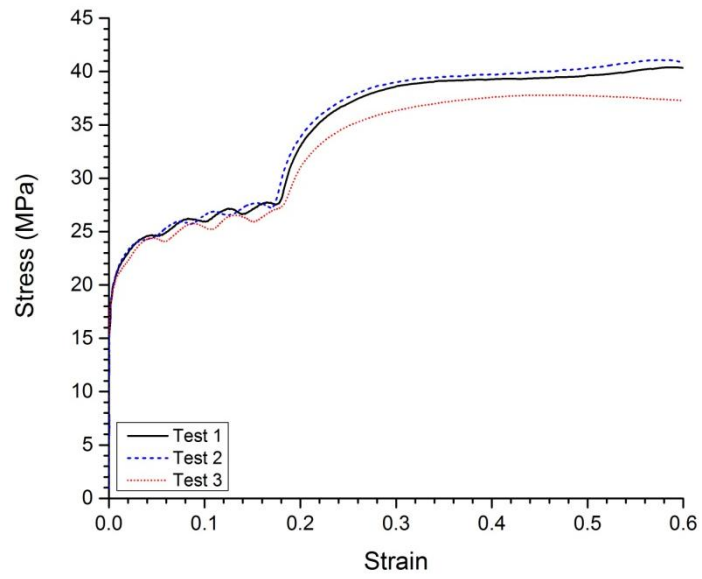
Figure 5.16 - Stress-strain curves for samples homogenized for 24 h at 600°C, deformed at 500°C. Rapid (ε = 0.2 to 0.25) strain rate transition from 1 s^{-1} to 10 s^{-1}.

6 Discussion

In this chapter the results presented in chapter 5 are discussed. The discussion begins with the through profile recrystallization of the extrudate, and the various restorative mechanisms occurring during the thermo-mechanical process. The progression of recrystallization through the profile of the extrudate, with focus on the surface and center, are also discussed. The effect of Zener pinning on the propensity of recrystallization is viewed with regards to the distribution of constituent particles through the transverse cross-section. Next is a comparison of grain thickness results in unrecrystallized extrudates from EBSD measurements and those determined using a simple geometric analysis. Later post-extrusion annealing experiments are compared to FEM model predictions for the centre of the extrudates using Zener-Holloman. The effect of transient strain rate history on the flow stress is discussed along with the physically-based constitutive model's ability to predict the behavior. The applicability of the model to non-steady-state strain rate condition is discussed.

6.1   As-Extruded Microstructure

The as-extruded microstructure of AA3xxx aluminum alloys is a function of the thermo-mechanical processing parameters such as the initial microstructure, temperature profiles and strain. The resulting as-extruded structure is dependent on the homogenization treatment (initial microstructure), extrusion temperature, ram speed (exit temperature) and extrusion ratio (strain).

6.1.1 The Effect of Homogenization Treatment

The homogenization treatment of a billet prior to extrusion sets the conditions up for extrusion. This is because the initial microstructure may have a large effect on the propensity of the structure to recrystallize. This is related to the fraction of constituents and dispersoid mean volume fraction, average radius and number density for a homogenization treatment (see Table 6.1 and Table 6.1). It has been observed by Geng [4], that an increase of the fraction of constituent particles in AA3003 during homogenization is accompanied by a decrease in the volume fraction of dispersoids.

The temperature ramp used to reach the soak temperature was constant for all treatments, the main variations being the soak temperature (500°C, 550°C and 600°C) and the soak durations (8 h and 24 h). What this achieved was a variation in the constituent and dispersoid structure (see Figure 6.1 below). The dark particles in the images are the constituent particles (mixture of $Al_6(Mn,Fe)$ and α-Al(Mn,Fe)Si) with a distribution of 1 - 5 μm [13] and the light colored small particles are the dispersoids (α-Al(Mn,Fe)Si phase) [4] [8]. The 8 h at 500°C homogenization treatment (Figure 6.1 (a)) provides a structure with a high dispersoid number density (~121/μm^3) and a lower fraction of constituents (~2.8%). The 8 h at 550°C homogenization treatment (Figure 6.1 (b)) provides a structure with a moderate dispersoid density and the billets homogenized for 24 h at 600°C (Figure 6.1 (c)) contain a dispersoid density close to zero. The dispersoid density of the microstructure prior to extrusion is of interest as it affects the extent of recrystallization present in the as-extruded structure (Figure 6.2). It was found that a lower dispersoid density resulted in a greater extent of recrystallization. This can be seen in Tables 5.4 to 5.6 for extrusion ratios of 70:1 or in Figure 6.2. The samples with homogenization treatment of 8 h at 500°C and 8 h at 550°C exhibited no recrystallization except for at ram speeds of 32 mm/s; Whereas samples homogenized for 24 h at 600°C were all close to 100% recrystallized.

(a)   (b)   (c)
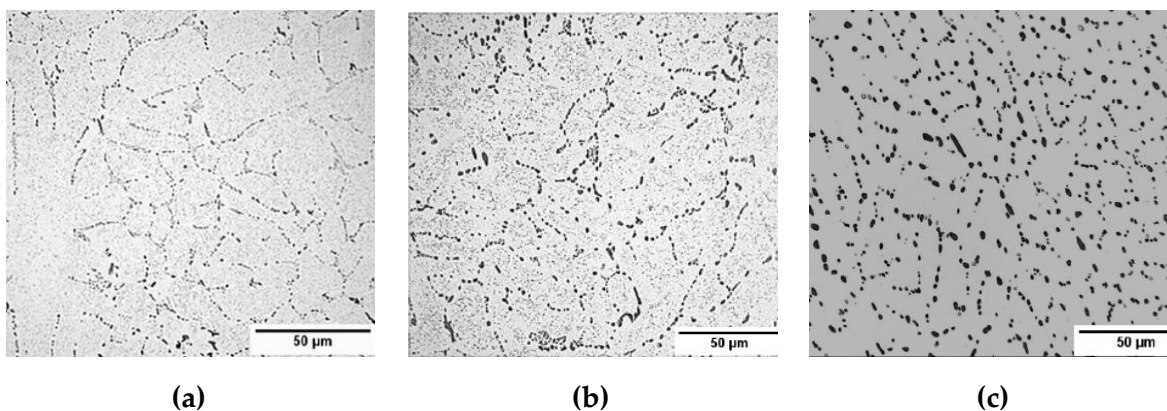
Figure 6.1 – Optical micrographs of homogenized AA3003: (a) 8 h at 500°C, (b) 8 h at 550°C and (c) 24 h at 600°C. Reproduced with permission from Geng [4].

Table 6.1 – Constituent and dispersoid particle data for various homogenization treatments. Data provided by [4] and [65].

Homogenization treatment	Measured fraction of constituents (%)	Dispersoids		
		Mean volume fraction, F_v (%)	Mean average radius, r (nm)	Mean number density, (#/μm^3)
8 h at 500°C	2.8 ± 0.3	1.18	27.6	121
8 h at 550°C	3.5 ± 0.3	0.95	62.1	--
24 h at 600°C	3.9 ± 0.2	0.23	138	0.18

(a) (b) (c)
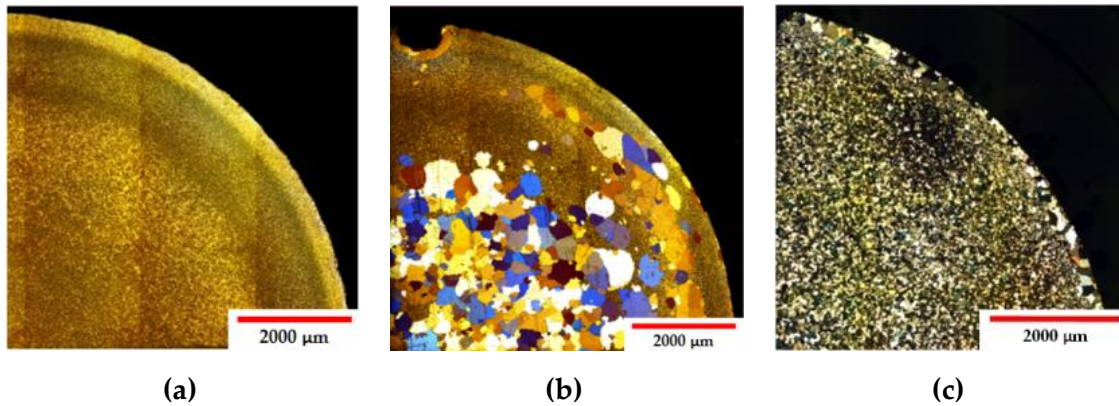
Figure 6.2 – Optical micrographs of anodized transverse sections illustrating the effect of homogenization treatment (a) 8 h at 500°C, (b) 8 h at 550°C and (c) 24 h at 600°C. All samples extruded at 500°C and a 70:1 ER.

6.1.2 The Effect of Extrusion Temperature and Ram Speed

The effect of the extrusion temperature and the ram speed are combined in this section as they both relate to the temperature history of the extrudate. The first relates to initial temperature of the billet while the later relates to the exit speed of the extrudate. The effect of extrusion temperature can be studied by examining Table 5.6 and 5.7 (in chapter 5.2.2) or by looking at Figure 6.3 and Figure 6.4.

(a)   (b)
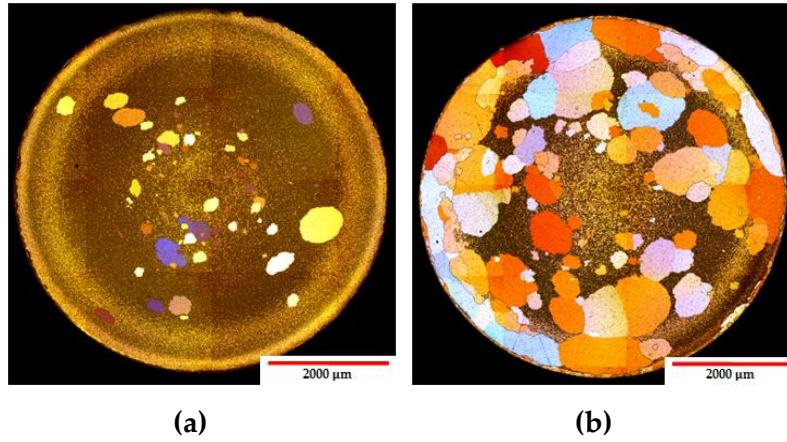
Figure 6.3 - Transverse optical micrographs of anodized samples illustrating the effect of extrusion temperature: (a) 400°C and (b) 500°C. Homogenization treatment of 8 h at 550°C, ram speed of 2 mm/s and ER of 280:1.

(a)   (b)   (c)
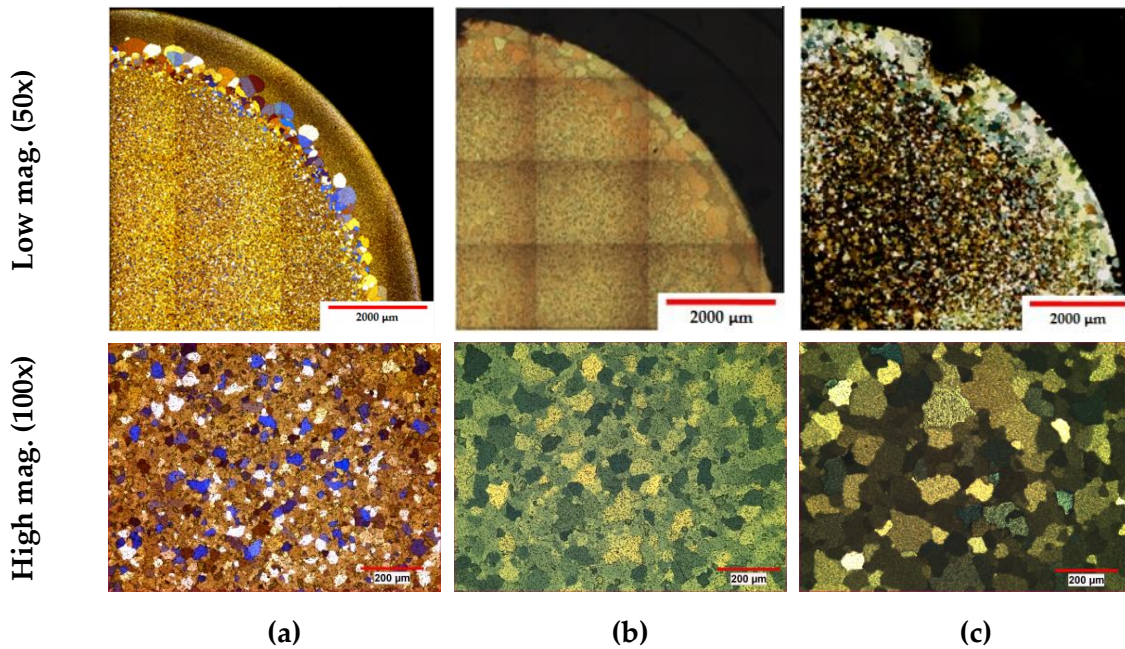
Figure 6.4 – Transverse optical micrographs of anodized samples illustrating the effect of extrusion temperature: (a) 350°C, (b) 400°C and (c) 500°C. Homogenization treatment of 24 h at 600°C, ram speed of 8 mm/s and ER of 70:1. The higher magnification images (100x) are of the centre region.

From Figure 6.3, it can be seen that as the extrusion temperature increases from 400°C to 500°C, the extent of recrystallization also increases. In Figure 6.4 we can see another effect of extrusion temperature. As the extrusion temperature is increased the final grain size increases. The grain size range increased from 20 to 45 μm at an extrusion temperature of 350°C to 20 to 170 μm at an extrusion temperature of 500°C. The effect of the ram speed can be seen by looking at Figure 6.5 and Tables 5.5 to 5.7 in chapter 5.2.2. The increase in the final grain size may be related to the number of viable nuclei available for recrystallization as a result of the low stored energy from extrusion at higher temperatures.

(a) **(b)**
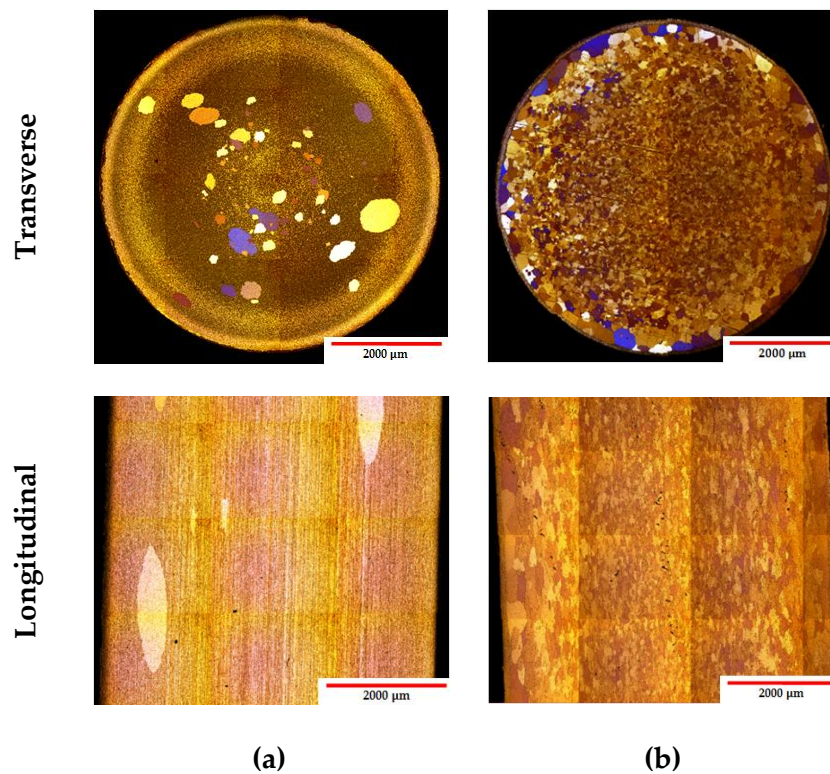
Figure 6.5 - Optical micrographs of anodized samples illustrating the effect of ram speed: (a) 2 mm/s and (b) 8 mm/s. Homogenization treatment of 8 h at 550°C, extrusion temperature of 400°C and ER of 280:1.

In general as the ram speed increases the extent of recrystallization increases. This effect can be attributed to a variety of effects, such as a strain rate effect and a temperature effect. As the ram speed is increased the strain rate of the system is increased and thereby increases the stored energy of the system. The mean strain rate experienced during extrusion can be estimated using equation (6.1) [5].

$$\dot{\varepsilon} = \frac{6 v_{ram} lnER}{D_C}$$

(6.1)

Where v_{ram} is the ram velocity, ER is the extrusion ratio, and D_c is the container diameter (106 mm). For samples with ER of 70:1, and ram speeds of 2 mm/s, 8 mm/s and 32 mm/s corresponds to an approximate mean strain rate of 0.5 s^{-1}, 1.9 s^{-1} and 7.7 s^{-1}, respectively.

An increase in ram speed results in an increase in the exit temperature of the extrudate as it relates to the extrusion exit speed, thereby dictating the time that the extrudate spends in the water quench. This contributes to the temperature history of the extrudate with regards to the cooling of the extrudate (i.e. how long the sample is in the quench, which may determine the effectiveness of the quench).

The exit speed, time to quench ($t_{to,q}$), and the time in quench ($t_{in,q}$) were all determined from information gathered during the extrusion trials. The times were calculated by using the ER of the sample and the ram speed. The exit speed (v_{ram}) and the time to quench and time in quench were calculated using equations (6.2), (6.3) and (6.4):

$$v_{exit} = v_{ram} \times ER$$

(6.2)

$$t_{to,q} = \frac{2000 mm}{v_{ram}}$$

(6.3)

$$t_{in,q} = \frac{L_{quench}}{v_{exit}}$$

(6.4)

The results for the various sets of conditions can be found in Table 6.2. From this information it can be seen that a sample with a high ER and a low ram speed (70:1 ER and v_{ram} = 2 mm/s) and a sample with a low ER and a higher ram speed (17:1 ER and v_{ram} = 8 mm/s) can have the same exit speed (v_{exit} = 128 mm/s) and therefore take the same amount of time to reach the quench ($t_{to,q}$ = 15.6 s) and remain in the quench ($t_{in,q}$ = 10.9 s). If both samples are extruded at the same temperature, as is the case in Figure 6.5, the sample with the slower ram speed (2 mm/s) takes almost 4 s to reach the quench while the one with a faster ram speed (8 mm/s) takes only approximately 1 s to reach the quench. The exact temperature profiles for the extrudates is unknown as there was no temperature tracking conducted from the point the extrudate leaves the die until it exits the quench. After the extrudate left the quench the temperature was measured using a hand held probe, but this information was not available for all samples. In general the samples that had a faster ram speed exhibited higher exit temperatures after leaving the die (please refer to Table 5.2, Table 5.4 and Table 5.5 in chapter 5.3.1 for the temperatures).

Table 6.2 – Exit speed, time to quench and time in quench for various sets of extrusion conditions.

Extrusion Ratio	Ram Speed, v_{ram} (mm/s)	Exit Speed, v_{exit} (mm/s)	Time to Quench, $t_{to,q}$ (s)	Time in Quench, $t_{in,q}$ (s)
17:1	8	128	15.6	10.9
70:1	2	128	15.6	10.9
70:1	8	512	3.90	2.73
70:1	32	2048	0.98	0.68
280:1	2	520	3.85	2.69
280:1	8	2080	0.96	0.67

6.1.3   The Effect of Extrusion Ratio

The effect of the extrusion ratio may also be presented as the effect of true strain on recrystallization of the deformed structure. The ideal true strain (here after referred to as strain) can be calculated by using the extrusion ratio, equation (6.5).

$$\varepsilon_T = ln\left(\frac{A_b}{A_e}\right) = \ln\left(ER\right) \tag{6.5}$$

were A_b is the transverse cross-sectional area of the billet after upset (106 mm), and A_e is the transverse cross-sectional area of the extrudate. Therefore extrusion ratios of 17:1, 70:1 and 280:1 have true strains of 2.8, 4.2 and 5.6, respectively. By comparing samples with the same homogenization treatment (8 h at 550°C), extrusion temperature (500°C) and ram speed (8 mm/s) one can compare the effect of extrusion ratio on the as-extruded microstructure. Figure 6.6, shows such a relationship.

As the extrusion ratio increases, the extent of recrystallization increases. Although it is difficult to see the extent of recrystallization in Figure 6.6 (a) it is assumed that this structure is unrecrystallized as it shows a fibrous structure (i.e. elongated grains of aspect ratio greater than 10). In the longitudinal section of Figure 6.6 (b) the structure is still mostly consistent of a fibrous structure, while Figure 6.6 (c) shows a fully recrystallized structure of grains with decreased aspect ratio (approximately 4:1, with distribution of 24 μm to 225 μm along the diameter). It is important to note that the exit speeds are different for all 3 of the images shown in Figure 6.6. This can also have an effect on the recrystallization kinetics as the exit temperatures would be different for all 3 of the samples. The difference in exit temperature between the sample with ER or 17:1 (v_{ram} = 128 mm/s) and 70:1 (v_{ram} = 512 mm/s) is

approximately 20°C (please refer to the temperatures given in tables 5.3 and 5.6), with the sample with the faster exit speed (ER = 70:1) having the greater exit temperature (542°C). Therefore as the extrusion ratio increases, with all other things being equal, the exit temperature of the extrudate also increases. This combined with the higher level of deformation increases the likelihood of recrystallization occurring.
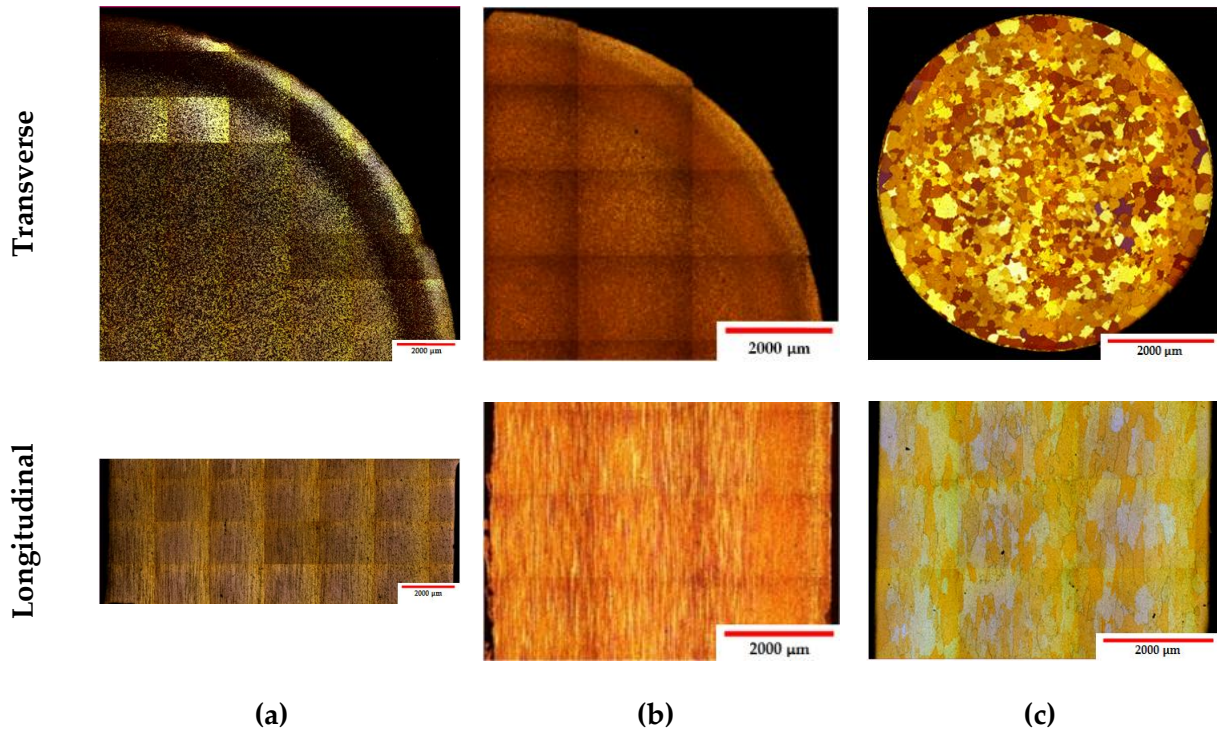
Figure 6.6 – Transverse and longitudinal optical micrographs of anodized samples showing the effect of extrusion ratio: (a) ER = 17:1, (b) ER = 70:1 and (c) ER = 280:1. (Homogenization of 8 h at 550°C, extrusion temperature of 500°C, and ram speed of 8 mm/s)

6.1.4   The Effect of Constituent Particle Distribution

After looking at the as-extruded microstructures it was noticed that two samples (*Sample 1:* 70:1 ER, 8 h at 500°C, $T_{extrusion}$ = 400°C, 32 mm/s; *Sample 2:* 70:1 ER, 8 h at 550°C, $T_{extrusion}$ = 350°C, 8 mm/s) recrystallized first at the boundary between the centre region and the ½ radius region (please refer to Table 5.9 in chapter 5.2.4). The constituent particle distributions for these two samples was investigated in order to determine whether the preferential recrystallization location was related to the distribution of constituent particles, and hence related to a low localized Zener pinning pressure in the region. Zener drag is widely estimated using equation (6.6) [40] [66]:

$$P_z = \frac{3\gamma_{gb}F_v}{2r}$$

(6.6)

where r is the average radius of the particles and F_v is the volume fraction of constituent particles. Therefore when the F_v /r ratio is large, a high Zener drag is obtained. This value was calculated for these samples to see if it would explain why the ½ radius and centre regions are experiencing recrystallization first and whether this is related to Zener drag. Figure 6.7 shows the F_v /r ratio for sample 1 and 2 through the cross-section. The F_v /r ratio is used in this case to give an estimate of the extent of Zener pinning in the system. In both cases it was found that the F_v /r ratio was highest at the ½ radius region (approximately 1.9 for sample 2 and 2.3 for sample 1) and decreases out to the surface (approximately 1.8). This would indicate that recrystallization would occur first at the surface and sub-surface, followed by the centre and the ½ radius region. This is opposite to what the micrographs show. The results indicate that there is another mechanism involved in this region (possibly the dispersoid distribution) that is not currently understood and requires further work.
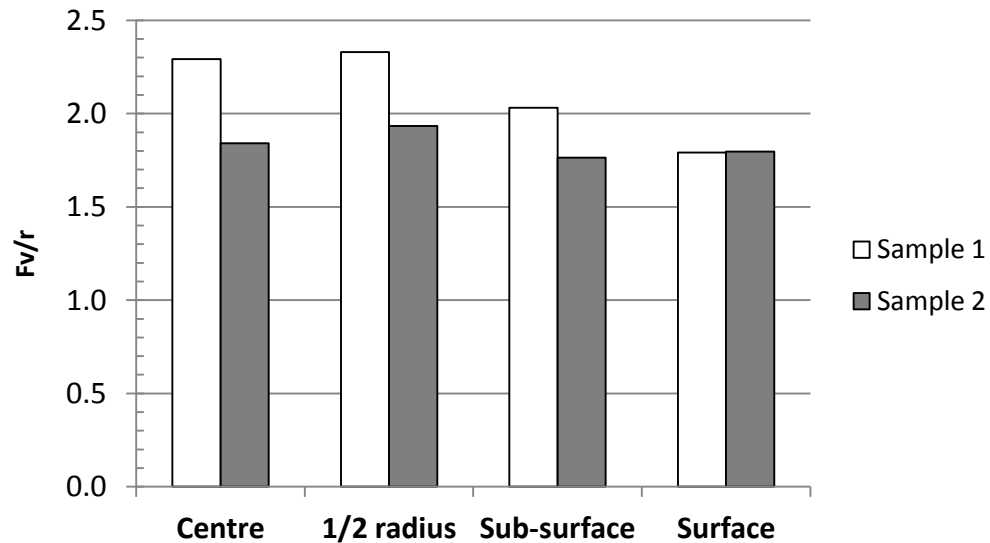
Figure 6.7 – *F_v /r* ratio results (*Sample 1:* 70:1 ER, 8 h at 500°C, T$_{extrusion}$ = 400°C, v$_{ram}$ = 32 mm/s; *Sample 2:* 70:1 ER, 8 h at 550°C, T$_{extrusion}$ = 350°C, v$_{ram}$ = 8 mm/s).

6.1.5 Summary

An investigation into the effect of homogenization treatment (initial microstructure), extrusion temperature and ram speed (strain rate and exit temperature), and extrusion ratio (strain) has shown that the greatest effect are from homogenization treatment and the exit

temperature of the extrudate. The exit temperature has been found to be a function of extrusion temperature, ram speed and extrusion ratio. Also in order to obtain a fully recrystallized structure one needs to have a high homogenization temperature and a long soak time (i.e. low dispersoid number density) or a high exit temperature. The later can be achieved by increasing the extrusion temperature or the ram speed, with both having approximately the same effect on the exit temperature (please refer to tables 5.5 and 5.6). Conversely to obtain an unrecrystallized structure a low extrusion temperature, smaller extrusion ratio and slower ramp speed are all desirable. If a fine grained recrystallized structure is of interest then a lower extrusion temperature is required (please refer to Figure 6.4). It should be noted that this has not taken into account the stability of the microstructure in progressive thermo-mechanical processing, but instead only the resultant as-extruded microstructure based on the various extrusion processing parameters tested for.

6.2   Post-Extrusion Annealing

Post-extrusion annealing tests were conducted in this investigation for two reasons. The first was to check the stability of unrecrystallized as-extruded microstructures and the second was to investigate the progression of recrystallization through the profile.

6.2.1   Stability of the Unrecrystallized Microstructure

The microstructure through the entire thermo-mechanical process (extrusion and annealing) was almost constant with regards to chemistry (i.e. minimal change in the Mn in solid solution). From homogenization to extrusion the changes in resistivity ranged from approximately -1.8 nΩm to 1.4 nΩm (the reader is referred to Table 5.10), and from extrusion to post-extrusion annealing of 10 min. at 550°C the change in resistivity ranged from approximately -1.9 nΩm to 1.0 nΩm (the reader is referred to Table 5.11). These are relatively small changes in resistivity as compared to the change from the as-cast state to the homogenized state where the measured change in resistivity was approximately -15 nΩm (from 62 nΩm in the as-cast state to 47 nΩm after homogenization of 10 h at 600°C) [13]. A change of 1.0 nΩm can be translated back to a very small change in the amount of Mn in solution, i.e. using a resistivity coefficient of ≈30 nΩm/wt% for Mn [35] a maximum change of ±2 nΩm corresponds to ±0.06 wt% Mn. This does not rule out an effect of Mn precipitation or dissolution, but it is speculated that this would be minor.

6.2.2 Progression of Recrystallization

Figure 6.8 shows the progression of recrystallization within the same sample (70:1 ER, 8 h at 500°C, 400°C extrusion temperature and v_{ram} = 32 mm/s) by using various temperatures (500°C, 525°C and 550°C) and times (1 min. and 10 min.) for post-extrusion annealing. Figure 6.8 (a) shows the as-extruded microstructure while Figure 6.8 (b) shows the sample after being in the nitrate salt bath (annealing) for 1 min. at 525°C and after (c) 10 min. at 550°C. The centre and the ½ radius region appear to recrystallize first, followed by the sub-surface region and possibly the surface. From image Figure 6.8 (d) one can see the surface structure of the post-extrusion annealing sample after 10 min. at 550°C. From an area calculation using the large grains as a boundary, this structure is said to be approximately 90% recrystallized. Although it is difficult to confirm from the optical micrographs of the anodized samples at what point in time the surface recrystallized and as to what extent this region has recrystallized as the structure in this region contains very fine grains (~< 15 µm) of unknown aspect ratio (i.e. it may possibly have been recrystallized even in the as-extruded state). The characterization of the surface layers by EBSD is recommended for future work. Figure 6.9 shows another example where the same type of recrystallization progression, as in Figure 6.8, is seen. This sample has also been homogenized for 8 h at 500°C and extruded using a temperature of 400°C. The ram speed this time was 8 mm/s instead of 32 mm/s. The initial grain structure (Figure 6.9 (a)) is highly fibrous and assumed to be 100% unrecrystallized, except perhaps at the surface. After post-extrusion annealing for (b) 10 min. at 525°C the sample appears to be 20% recrystallized. After post-extrusion annealing for (c) 1 min. at 550°C the sample is approximately 45% recrystallized, and is more than 95% recrystallized after (d) 10 min. at 550°C. Once again there is a fine grain structure at the surface and therefore is difficult to conclude, from optical micrographs, the full extent of recrystallization.

This presence of a fine grain surface structure has been reported in studies of high temperature and large strain deformation of aluminum alloys [38] [36]. The appearance of the fine surface grain layer has been attributed to a restorative mechanism termed Geometric dynamic recrystallization (GDRX) [14] [36] [40] [44] [45]). GDRX is dependent on the initial grain size and the deformation conditions. As this study involved the high temperature deformation of AA3003, under high strain and strain rate conditions, the presence of this fine grain layer at the surface could be due to GDRX.
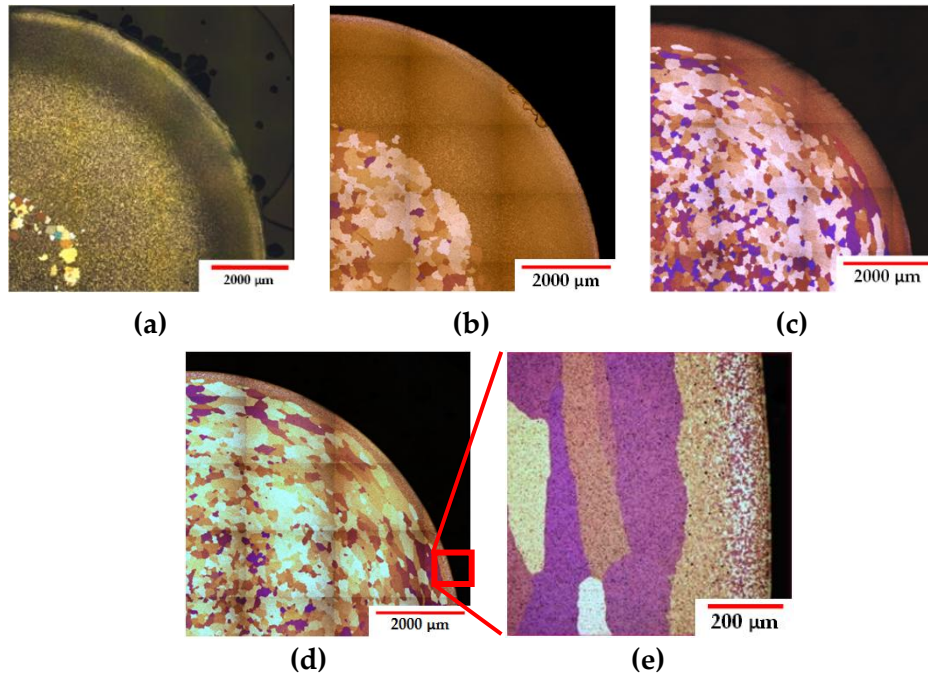
Figure 6.8 – Transverse optical micrographs of anodized 70:1 ER samples (8 h at 500°C, extrusion temperature of 400°C and ram speed of 32 mm/s): (a) as-extruded after post-extrusion annealing: (b) 1 min. at 525°C (~35% recrystallized), (c) 1 min. at 550°C (~>80% recrystallized), (d) 10 min. at 550°C (~>90% recrystallized), and (e) higher magnification of the surface of sample (d).
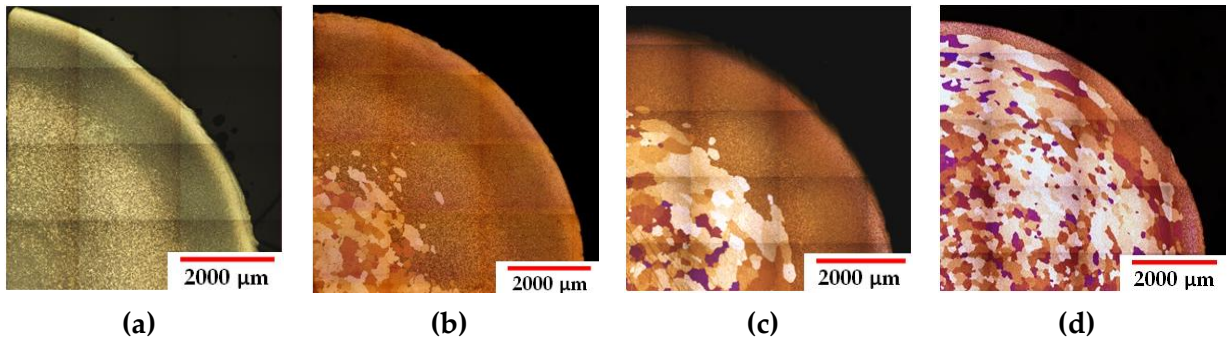
Figure 6.9 – Transverse optical micrographs of anodized 70:1 ER samples (homogenized for 8 h at 500°C, extrusion temperature of 400°C and ram speed of 8 mm/s): (a) as-extruded (unrecrystallized), (b) 10 min. at 525°C (~20% recrystallized), (c) 1 min. at 550°C (~45% recrystallized), and (d) 10 min. at 550°C (~>95% recrystallized).

6.2.3 Summary

The post-extrusion annealing results indicate that, in most cases, recrystallization is possible after extrusion and that there is minimal change in the chemistry of the system during thermo-mechanical processing. This indicates that the Zener pressure may not have been large enough in the system to retard recrystallization, but instead large enough to impede nucleation during recrystallization. The resultant grains from the post-extrusion annealing tests were of high aspect ratio and there was minimal variation in the size through the profile. This may be attributed to a directional Zener pinning pressure in the structure due to the aspect ratio of the constituent particles and their spatial distribution (the particles align preferentially to the extrusion direction), thereby allowing recrystallization to occur preferentially in the extrusion direction. The grain size of the grains may be due to a low amount of viable nuclei for recrystallization.

The post-extrusion annealing results have also shown that recrystallization follows a pattern of beginning at the centre and moving outwards to the surface of the sample. In cases in which recrystallization begins at the boundary between the centre and the ½ radius boundary, recrystallization first progresses towards the centre before progressing towards the surface. In general it is difficult to determine when 100% recrystallization has occurred as the surface region, in some cases, appears to consist of small equiaxed grains that may be a result of GDRX.

6.3 Comparison of Recrystallization Predictions and Experiments

Recrystallization in an extruded product is complex. There are a number of restorative mechanisms (recovery, static recrystallization, dynamic recrystallization and grain growth) occurring during and after the high temperature (350°C to 500°C), high strain rate (up to approximately 8 s^{-1}) and large strain (ε = 2.8 to 5.6), deformation of AA3003. During this thermo-mechanical process there is a complex interplay between recovery and recrystallization during and after extrusion. The complexity is only further increased by the through profile effects. During the extrusion process the extrudate not only undergoes a complex process, but the extrudate also experiences a range of deformation conditions (strain rate and temperature are greater at the surface than the center) and hence there is a resultant difference in the recrystallization behavior through the profile of the extrudate. The 'unrecrystallized' grain thickness was investigated and compared against a simple mass balance model. By conducting post-extrusion annealing tests on unrecrystallized structures after extrusion we were able to test the stability of the unrecrystallized structure through the profile. These results were compared against a recrystallization model developed at the University of Waterloo by Mahmoodkhani.

6.3.1 Comparison of the Models and Experiments: Grain Size

The simplest microstructural feature that could be used to characterize the deformed state is the grain shape. Information on the grain and subgrain structures is important as grain size strongly affects the mechanical properties and influences the physical properties, surface properties, phase transformation and annealing behavior [48]. When deformed, the grains of polycrystalline metals change in a manner that corresponds to the macroscopic shape change [40].

EBSD measurements can provide data of highly deformed polycrystalline materials, if the boundaries and not the dislocations are of primary interest, with a high degree of statistical reliability [41] [49]. The grain size has traditionally been measured by optical microscopy but the characterization of grain size and related parameters is difficult on highly deformed structures. A sensitivity analysis on the step size and clean-up procedure can be found in Appendix C. The average 3-D grain thickness for the 17:1 ER and 70:1 ER samples were found to be 18.6 µm and 9.0 µm, respectively (refer to chapter 5.3.3).

In the simple mass balance model the as-extruded grain size is estimated using the ER calculated at a temperature of 500°C (i.e. taking into account thermal expansion but not the upset). The initial 3-D grain size at the centre takes into account thermal expansion (r_i ~ 73.8 µm). A constant volume ($V_i = V_f$) is assumed. The final grain thickness and grain length can be approximated using the following relationships (equations (6.7) to(6.11)) and Figure 6.10, where SA_i is the initial surface area, SA_f is the final surface area and ER is the extrusion ratio. The new ER (i.e. taking into consideration thermal expansion and ignoring the upset) was calculated using a coefficient of thermal expansion of 23.6 x 10^{-6}/°C and an extrusion temperature of 500°C. A temperature difference of approximately 480°C translates to a thermal expansion of approximately 1 mm for the 101.6 mm diameter billet (i.e. initial billet diameter is approximately 102 mm, and the initial grain size goes from 73 µm to 73.8 µm).
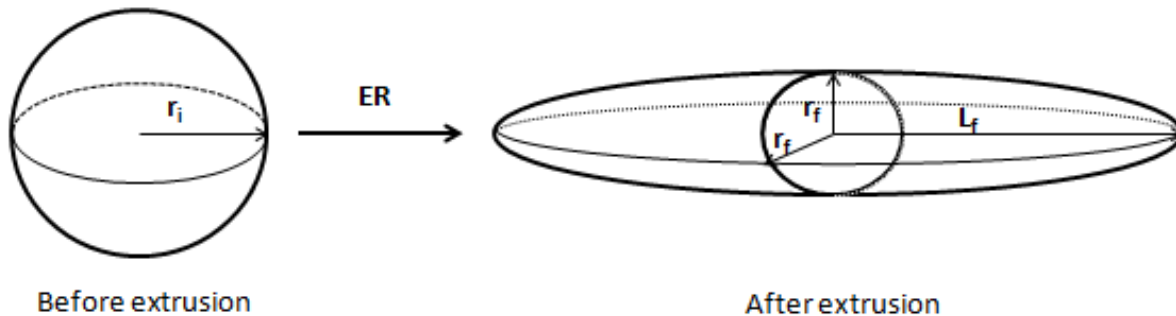
Figure 6.10 – Grain volume mass balance schematic.

$$V_i = V_f = \frac{4}{3}\pi r_i{}^3 = \frac{4}{3}\pi r_f{}^2 L_f \tag{6.7}$$

$$ER_{TH} = \frac{SA_i}{SA_f} = \frac{r_i^2}{r_f^2} \tag{6.8}$$

$$L_f = \sqrt{\frac{SA_i}{ER_{TH}}} \tag{6.9}$$

$$L_f = \frac{V_i}{SA_f} \tag{6.10}$$

where ER_{TH} is the extrusion ratio taking into account thermal expansion, V_f is the final volume, L_f is half of the final length, and the aspect ratio (AR) can be estimated as:

$$AR = \frac{L_f}{r_f} \tag{6.11}$$

This simple mass balance approach estimates the as-extruded 3-D grain thickness, at the centre, as 18.4 µm, 9.1 µm and 4.6 µm for ER of 17:1, 70:1 and 280:1, respectively. It also estimates the aspect ratios as 64:1 for an ER of 17:1, 524:1 for an ER of 70:1 and 4265:1 for an ER of 280:1. Table 6.3 summarizes the results from the two approaches. The experimental values and the mass balance are in good accordance with one another, although there are some differences. These differences may be attributed to an accumulation of experimental test sensitivity to the step size used during EBSD, the definition of HAGB and the presence of recrystallized grains.

Table 6.3 – Summary of 3-D grain thickness results from EBSD and mass balance approach.

Extrusion Ratio (with upset)	Extrusion Ratio (with thermal expansion and no upset)	Average 3-D grain thickness from EBSD, (µm)	3-D grain thickness from mass balance, (µm)	Aspect ratio from mass balance (after extrusion)
17:1	16:1	18.6	18.4	64:1
70:1	65:1	9.0	9.1	524:1
280:1	263:1	--	4.6	4265:1

6.3.2 Recrystallization Model

Mahmoodkhani et al. [12] developed a 2D mathematical model of the extrusion process for AA3003 using commercial Finite Element Method (FEM) package DEFORM-2D at the Univeristy of Waterloo. The model is able to make predictions regarding the grain thickness through the profile of the extrudate and is able to predict when a system will have the propensity to recrystallize. In this recrystallization model the driving pressure for recrystallization is taken as a balance between the stored energy of the system (assumed to come from dislocation accumulation during deformation and grain boundary energy) and the Zener pinning pressure (equation(2.4)) [40] [66]:

$$P = E_\perp + E_{gb} - P_Z = \alpha\rho Gb^2 + \gamma_{gb}A_{gb} - \frac{3\gamma_{gb}F_V}{2r} \tag{6.12}$$

where $E_\perp$ is the dislocation stored energy, E_{gb} is the grain boundary energy and γ_{gb} and $A_{gb,}$ represent the grain boundary energy and the grain boundary area (calculated from grain shape predictions from FE calculations), respectively. The dislocation density (ρ) is calculated using the average flow stress (σ_{avg}) as shown in equation (6.13) and equation (6.14) [67], below.

$$\rho = \left(\frac{\sigma_{avg}}{\alpha Gb}\right)^2 \tag{6.13}$$

$$\sigma_{avg} = \frac{\int_0^\varepsilon \sigma d\varepsilon}{\varepsilon} \tag{6.14}$$

The Zener pinning pressure (P_Z) takes into account both the contributions from the dispersoids and the constituent particles [67]. The dispersoid volume fraction (F_v) and dispersoid radius (r) comes from the homogenization model developed by Du et al. [13], and the constituent particle volume fraction and radii were obtained from experimental data gathered by Geng [4]. The contributions from both types of precipitates are added linearly to obtain P_Z.

For this discussion the focus will be on predictions and experimental results from the centre line (i.e. Centre region) of the extrudates.

6.3.3 Comparison of the Model and Experiments: Recrystallization (Centre line)

Mahmoodkhani et al. [12] model for the prediction of recrystallization along the centre line of the extrudate is compared to experimental results in this section. Figure 6.11 shows the results from the recrystallization model for stored energy (including grain boundary energy)

and the total Zener drag for 7 different extrusion samples. For each sample there are two possible cases:

- Stored energy < Zener drag → P < 0 → Recrystallization is unfavorable.
- Stored energy > Zener drag → P > 0 → Recrystallization is favorable.

This would indicate that the 2 samples, on the left, with homogenization treatment of 8 h at 500°C would not be expected to recrystallize as the stored energy is less than the Zener drag; Whereas the 4 samples on the right would be expected to recrystallize. The last two samples (24 h at 600°C) have a much larger stored energy than Zener drag indicating that a lower dispersoid density favors recrystallization. The sample with extrusion temperature of 500°C, ram speed of 2 mm/s and homogenization treatment of 8 h at 550°C has a P ~ 0. Therefore it is uncertain as to whether recrystallization is favorable as such a small difference may be attributed to model artifacts. All of these predictions were examined with EBSD or optical micrographs.
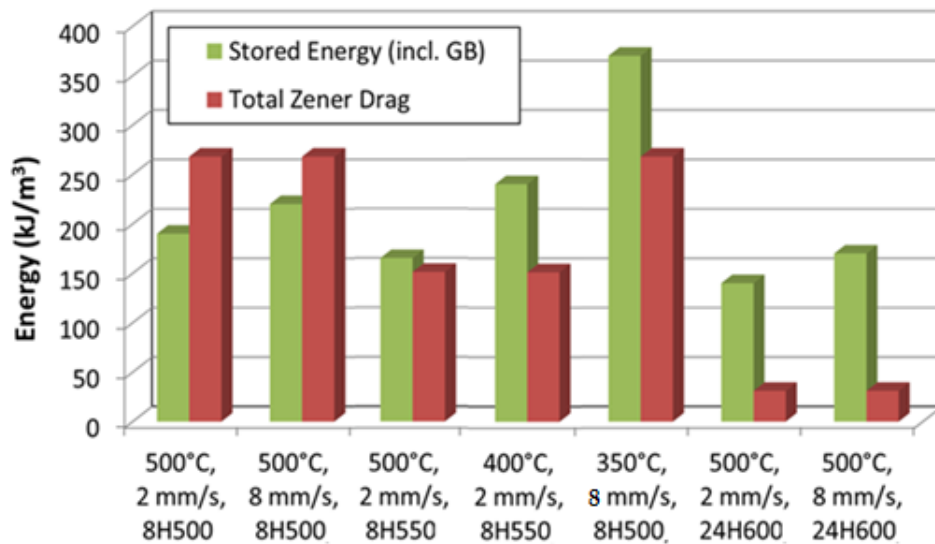
Figure 6.11 - Stored energy and Zener drag results, for the centre region, for various 70:1 ER samples. Reproduced with the permission of Mahmoodkhani [68].

Figure 6.12 shows optical micrographs of anodized samples whose stored energy is greater than their Zener drag (last 4 samples of Figure 6.11) and therefore are described as having a propensity to recrystallize. The samples with homogenization treatment of 24 h at 600°C are both fully recrystallized at the centre, and through the entire cross-section, after extrusion. The sample with homogenization treatment of 8 h at 550°C that was extruded at 400°C, with a ram speed of 2 mm/s was not recrystallized after extrusion (please refer to Table

5.5), but after a post-extrusion annealing of 1 min. at 525°C (Figure 6.12 (b)) the centre started to recrystallized and was fully recrystallized after 10 min. at 525°C. The same trend was found for the sample with homogenization treatment of 8 h at 500°C with extrusion temperature of 500°C and ram speed of 8 mm/s, after post-extrusion annealing for 1 min. at 525°C the centre of the sample was fully recrystallized (Figure 6.12 (b)).

(a) 400°C, 2 mm/s,
8 h at 550°C
(1 min. at 525°C)

(b) 350°C, 8 mm/s,
8 h at 500°C
(1 min. at 525°C)

(c) 500°C, 2 mm/s,
24 h at 600°C
(as-extruded)

(d) 500°C, 8 mm/s,
24 h at 600°C
(as-extruded)
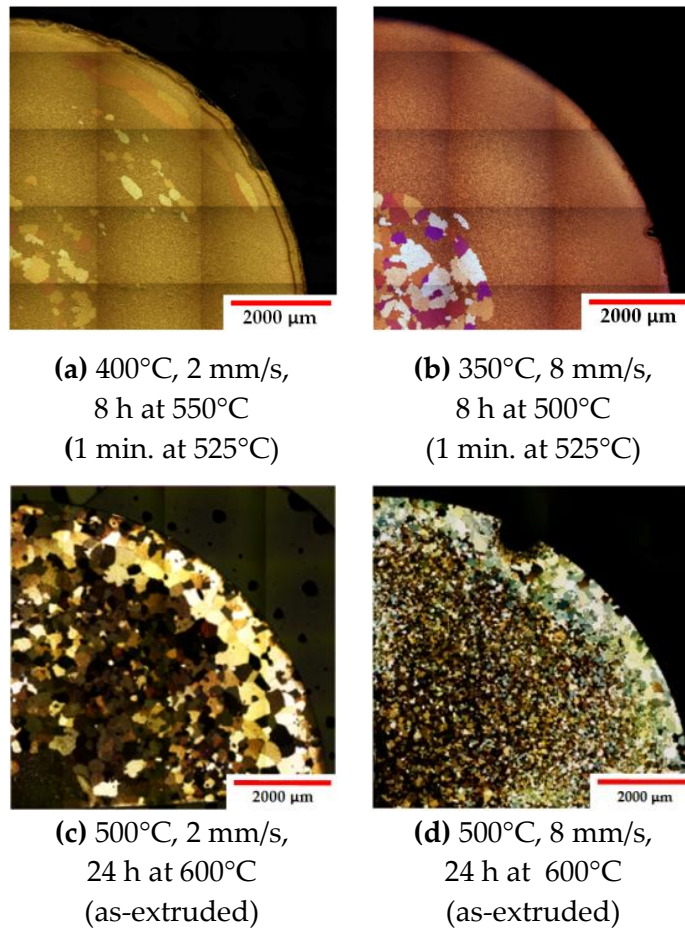
Figure 6.12 – Transverse optical micrographs of anodized samples where recrystallization is favorable (P > 0) according to Figure 6.11.

Figure 6.13 shows the transverse optical micrographs of anodized samples where recrystallization is unfavorable (P < 0) or difficult to determine (P ~ 0) – the first 3 samples of Figure 6.11. The samples with homogenization treatment of 8 h at 500°C, extrusion temperature of 500°C and ram speeds of 2 mm/s and 8 mm/s were both unrecrystallized after extrusion (please refer to Table 5.6 for the as-extruded micrographs). Post-extrusion annealing was conducted for these two samples and after 10 min. at 550°C (Figure 6.13 (a) and (b)) the samples did not experience any recrystallization at the centre, or at any other location along the radius. This correlates with the predications made that recrystallization is unfavorable for these sets of

extrusion conditions. The sample with P ~ 0 (homogenization treatment of 8 h at 550°C, extrusion temperature of 500°C and ram speed of 8 mm/s) was also unrecrystallized after extrusion, but after post-extrusion annealing for 10 min. at 550°C the centre of the sample was fully recrystallized. This indicates that the stored energy was high enough to overcome the Zener pinning pressure of the system.

(a) 500°C, 2 mm/s,	**(b)** 500°C, 8 mm/s,	**(c)** 500°C, 2 mm/s,
8 h at 500°C	8 h at 500°C	8 h at 550°C
(10 min. at 550°C)	**(**10 min. at 550°C)	**(**10 min. at 550°C)
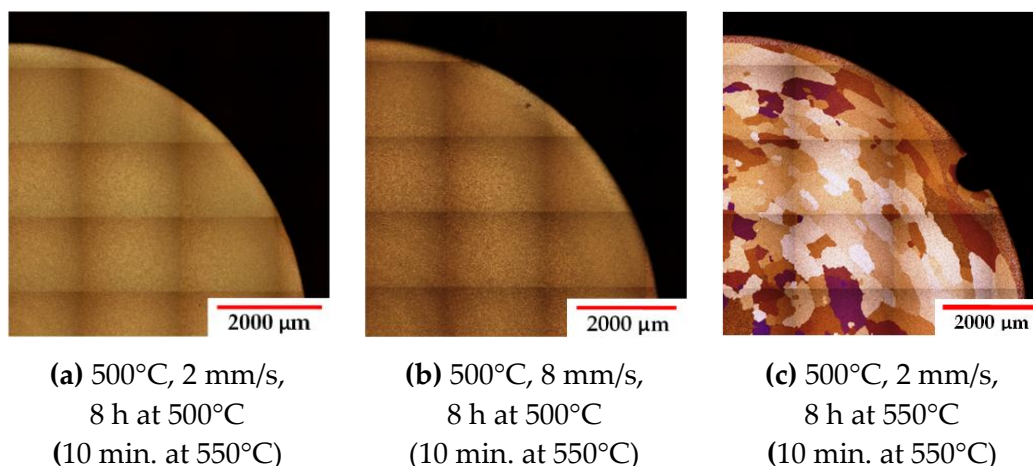
Figure 6.13 - Transverse optical micrographs of anodized samples where recrystallization is unfavorable (P < 0) (a) and (b) and where P ~ 0 (c), according to Figure 6.11.

6.3.4   Summary

The grain size of the unrecrystallized as extruded structures were close to the results obtained using a simple mass balance approach. The mass balance predicted 3-D grain thickness of approximately 18.4 μm for an ER of 17:1, 9.1 μm for an ER of 70:1, and approximately 4.6 μm for an ER of 280:1. The EBSD measurements fit in this range with measured average 3-D grain thicknesses of 18.6 μm and 9.0 μm for ER of 17:1 and 70:1, respectively. In the future, the fact that the change in grain shape appears to be a geometric relationship may be used to approximate the local strain by the grain shape change. This may allow one to be able to measure the through profile strain distribution using this technique.

The model predictions (made by FEM model developed by Mahmoodkhani et al. [12]) for recrystallization behavior, of the centre line of the extrudates, fit well with the experimental data. In general the lower the dispersoid density of the microstructure (24 h at 600°C) the greater the propensity for recrystallization as the stored energy is much greater than the Zener pinning pressure. Samples with high Zener pinning (high dispersoid density – 8 h at 500°C and 8 h at 550°C) were unrecrystallized after extrusion, and the unrecrystallized structure was most stable for those with extrusion temperature of 500°C. These samples did not show any signs of recrystallization after post-extrusion annealing for 10 min. at 550°C. More tests are needed to

continue to explore the stability of these structures (i.e. longer anneal time). The 8 h at 500°C sample with extrusion temperature of 500°C and ram speed of 32 mm/s was approximately 15% recrystallized after post-extrusion annealing for 10 min. at 550°C, indicating that an unrecrystallized as-extruded structure produced during extrusion is less stable than one produced using a slower ram speed (i.e. 2 mm/s or 8 mm/s – refer to Table 5.10).

6.4   The Effect of Transient Strain Rate on the Flow Stress

The Kocks and Chen constitutive model for flow stress has been used by Kubiak [5] and Geng [4] in the study of the hot deformation mechanisms of AA3xxx. Through high temperature compression tests Kubiak and Geng noticed that the strain rate had an effect on the flow stress of AA3003. Figure 6.14, shows the effect of strain rate on the flow stress of AA3003 deformed at 500°C, after a homogenization treatment of 8 h at 500°C. As the strain rate increases the flow stress of the material decreases. Therefore the current investigation looked to study the constitutive behavior of AA3003 under a transient strain rate scenario.
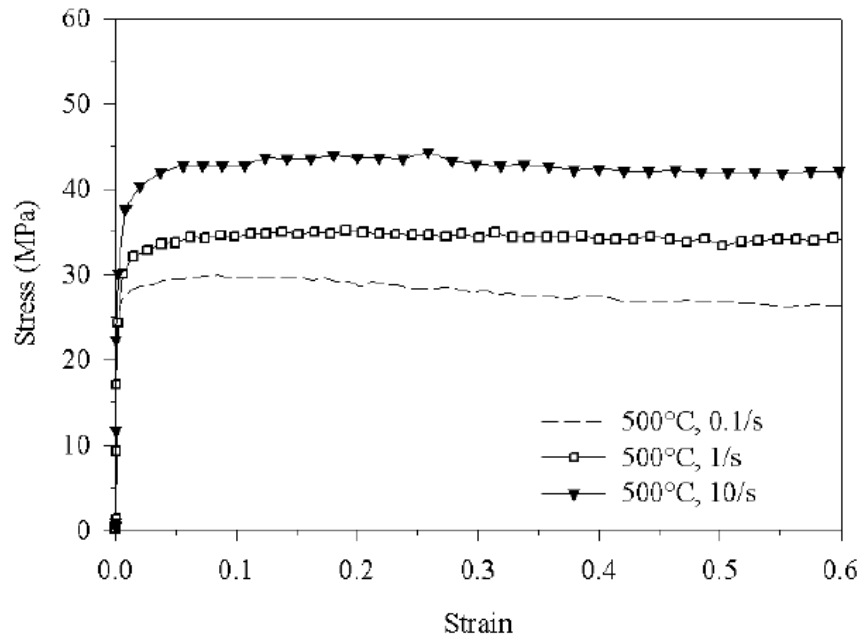
Figure 6.14 – Effect of strain rate on flow stress. High Mn alloys (1.27 wt% Mn) with a homogenization treatment of 8 h at 500°C, deformed at 500°C. Reproduced with permission from Kubiak [5].

6.4.1 The Constitutive Model

The Kocks and Chen constitutive model, shown in equation (6.15)(2.12), applies to the viscous dislocation motion regime as companied by diffusion of solute [56].

$$\dot{\varepsilon} = A \left(\frac{\sigma}{\mu}\right)^n \frac{\mu b^3}{kT} exp\left(-\frac{Q_D}{RT}\right) \tag{6.15}$$

where A is a pre-exponential constant, σ is the applied stress, μ is the temperature dependent shear modulus, n is the stress exponent, b is the magnitude of the temperature dependent Burger's vector, k is the Boltzmann's constant, T is the deformation temperature, Q_D is the activation energy for diffusion of the diffusing species, and R is the gas constant. In this study the diffusion of Mn was assumed to be the rate controlling parameter and therefore the activation energy that was used was 211.4 kJ/mol [69], as this is the activation energy for the diffusion of Mn in aluminum. The temperature dependent parameters used are summarized in Table 6.4, below. Information regarding how the yield stress and the flow stress were determined can be found in chapter 4.3.3.

Table 6.4 – Parameters used in AA3xxx constitutive model.

Parameter	Value	Unit
μ_0	25400	MPa
T_M	933	K
$\dfrac{T_M}{\mu_0}\dfrac{d\mu}{dT}$	-0.5	
a	4.05×10^{-10}	m
k	1.38065×10^{-23}	Pa.m^3.K^{-1}
Q_D	211400	J.mol^{-1}
R	8.314	J.K^{-1}.mol^{-1}

The Kocks and Chen equation can be rearranged and used to plot data on a semi-log plot using the following equations for the x-axis and y-axis, in order to obtain values for the pre-exponential constant (A) and the stress exponent (n).

$$log \left(\frac{\sigma}{\mu}\right) = \frac{1}{n} \log \left[\frac{\dot{\varepsilon}}{s^{-1}} \frac{kT}{\mu b^3} exp \left(\frac{Q_D}{RT}\right)\right] - \frac{1}{n} log(A)$$ (6.16)

where,

$$y = log \left(\frac{\sigma}{\mu}\right)$$ (6.17)

$$x = \log \left[\frac{\dot{\varepsilon}}{s^{-1}} \frac{kT}{\mu b^3} exp \left(\frac{Q_D}{RT}\right)\right]$$ (6.18)

6.4.2 Checking the Applicability of the Constitutive Model

The flow stress, yield stress and work hardening results from the high temperature compression tests were plotted using the constitutive model and the exact experimental values. The data presented is for a homogenization treatment of 24 h at 600°C. New test data includes the following:

- Deformation temperature of 500°C, strain rate of 1 s^{-1}.
- Deformation temperature of 500°C, strain rate of 10 s^{-1}.
- Deformation temperature of 500°C, transient strain rate from 1 to 10 s^{-1}, gradual transition from 0.2 to 0.4 strain
- Deformation temperature of 500°C, transient strain rate from 1 to 10 s^{-1}, moderate transition from 0.2 to 0.3 strain.
- Deformation temperature of 500°C, transient strain rate from 1 to 10 s^{-1}, rapid transition from 0.2 to 0.3 strain.

The new data was plotted along with data obtained from Kubiak [5] for tests conducted using a deformation temperatures of 400°C, 500°C and 600°C and strain rates of 10 s^{-1}, 1 s^{-1} and 0.1 s^{-1}, respectively. This is presented in Figure 6.15 to Figure 6.18. Figure 6.15, shows the reproducibility of the high temperature compression tests. The new constant strain rate data and the new transitional strain rate test flow stress data has a good fit to the data provided by Kubiak. Some general observations that can be derived from this plot are that high temperature, low strain rate tests (600°C, 0.1 s^{-1}) result in a low value of 'x' (approximately 10), while low temperature, high strain rate tests (400°C, 10 s^{-1}) result in high values of 'x' (approximately 15.8). The next thing that can be seen is that there is a small vertical spread in the data for constant 10

s^{-1} strain rate tests and transitional strain rate tests. A straight line is fit to the data (Figure 6.16) in order to determine the fitting parameters (A and n). Although the fit is good (R^2 = 0.95) the small vertical spread in the data, for the transitional strain rate tests, could lead to a poor fit of the fitting parameters for this data.

Figure 6.17, shows the fit of the yield stress data to the model. The fit for this data is not as good (R^2 = 0.76) as the fit for the steady-state flow stress. There is a vertical spread in the data again at an 'x' value of approximately 14 (this is the data from the transient strain rate tests). The reason for the spread here may be attributed to how the yield stress data was gathered, as the experimental stress strain data for these tests was smoothed and in some situations the yield stress may have been shifted when the smoothing function was applied to the data. In general, the model does follow the experimental data closely providing an adequate correlation to the constitutive model.

Figure 6.18 shows the work hardening of the material plotted using the constitutive model, where the work hardening is defined as the difference between the steady-state flow stress and the yield stress. The material was found to experience little work hardening except for at higher 'x' values (> 15) which correspond to low temperature, high strain rate deformations. This is the combination where the model approaches its limits.
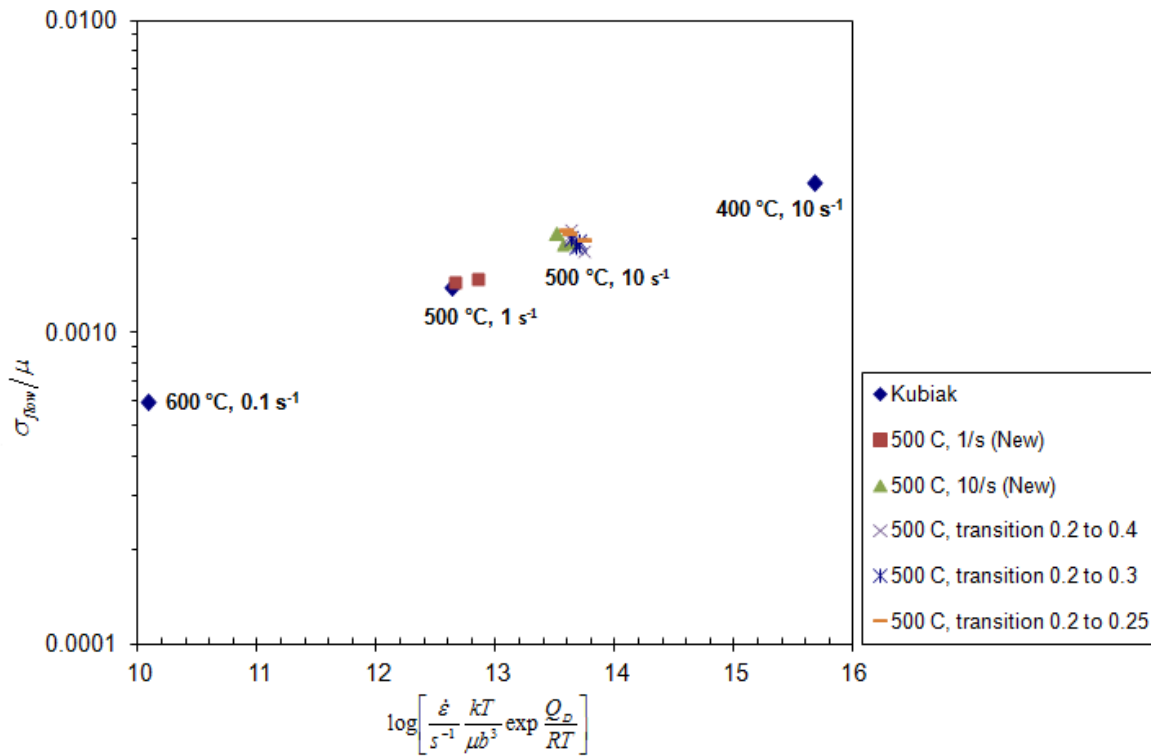
Figure 6.15 - Steady-state flow stress data for a homogenization of 24 h at 600°C plotted using the constitutive model. Some data provided by Kubiak [5].
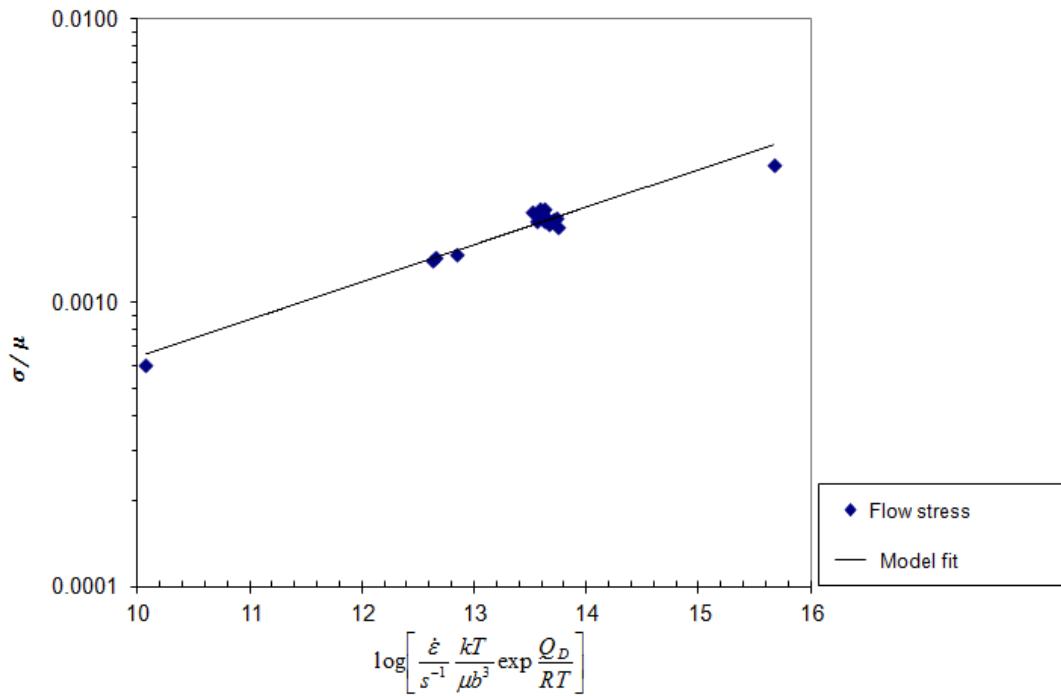
Figure 6.16 - Linear fit of the steady-state flow stress data for a homogenization of 24 h at 600°C plotted using the constitutive model ($R^2 = 0.95$). Some data provided by Kubiak [5].
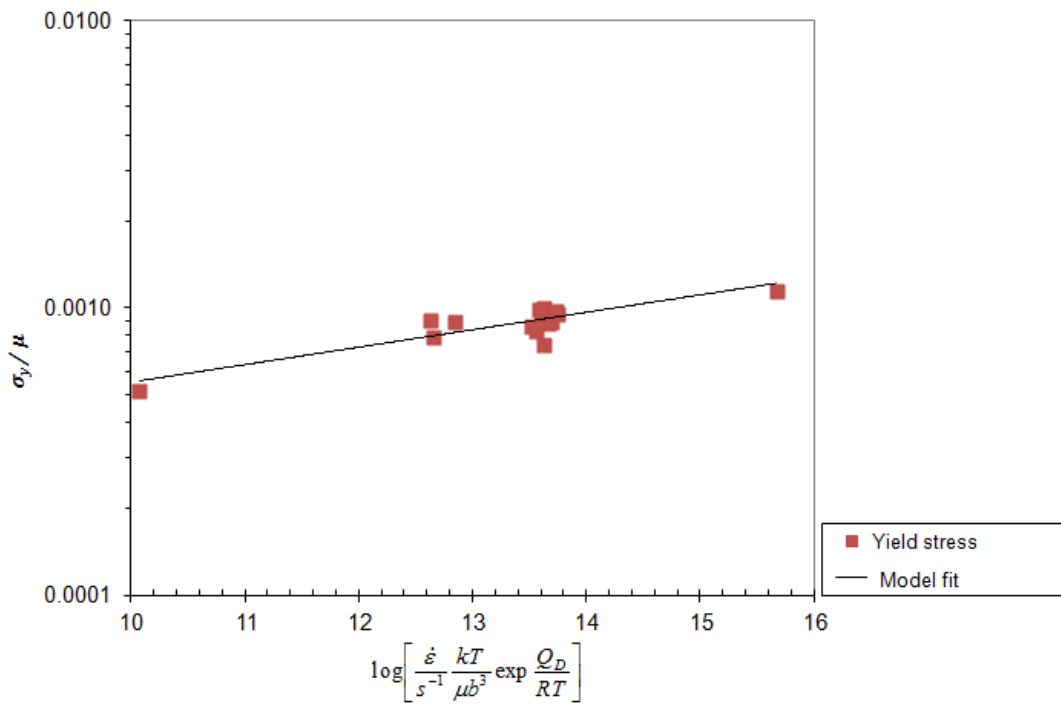
Figure 6.17 - Yield stress data a homogenization of 24 h at 600°C plotted using the constitutive model ($R^2 = 0.76$). Some data provided by Kubiak [5].
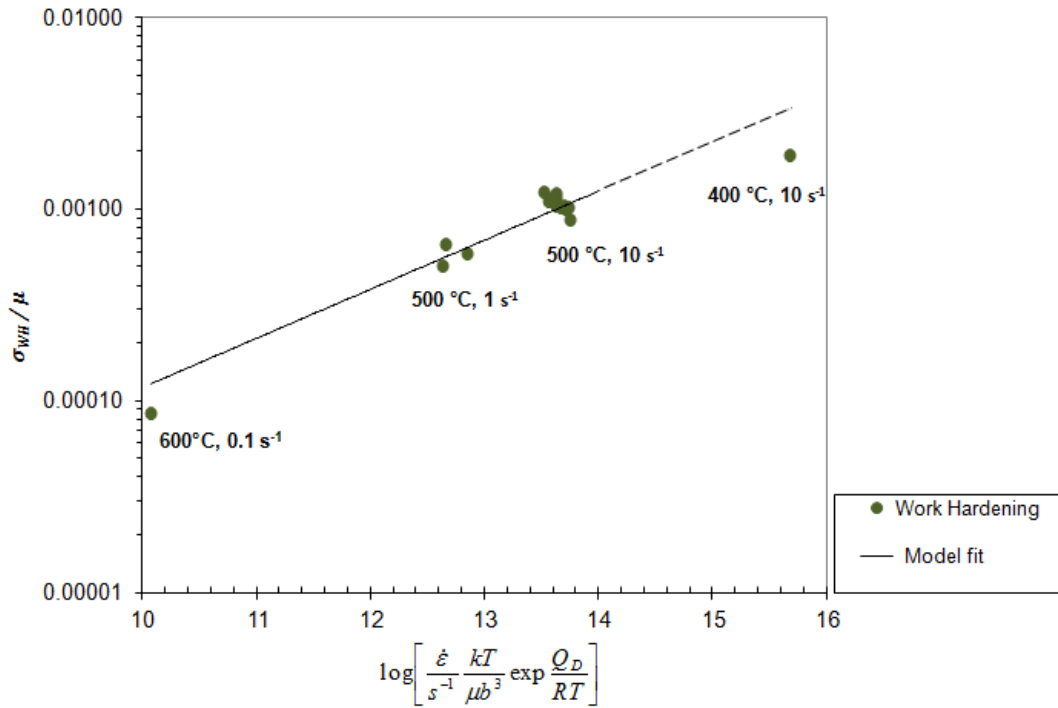
Figure 6.18 – Work hardening data ($\sigma_{flow} - \sigma_y$) for a homogenization of 24 h at 600°C plotted using the constitutive model. Some data provided by Kubiak [5].

6.4.3 Fitting the Constitutive Model

The pre-exponential constant (A) and the stress exponent (n) were derived from the linear model fit curve in Figure 6.16. The fitting parameters used by Kubiak [5] and Geng [4] were A = 1.06 x 10^{36} s^{-1} and n = 8.1. As the homogenization treatment (24 h at 600°C), deformation temperature (500°C) and strain rates (1 s^{-1} to 10 s^{-1}) of the current study are within the range of parameters used in previous work([4] [5]) a stress exponent of n = 8.1 was also used here. This value is close to the one found for the current study (n = 7.6). This work and previous work by Kubiak and Geng all present stress exponent values that are well above 3, which is out of the range of solute drag. The reason for this remains unknown and was not part of the scope of this study. In order to improve the fit of the model to the experimental results only 'A' was adjusted.

The experimental strain rates (refer to chapter 4.3.4 for details), and temperatures were used as inputs in the Kocks and Chen model. The model was fit to the smoothed experimental data using a pre-exponential value of A = 5.51 x 10^{35} s^{-1} and stress exponent n = 8.1. Various values for the pre-exponential were used and A = 5.51 x 10^{35} s^{-1} was found to follow the experimental data most closely within the steady-state region (~ 0.3 to 0.6 strain). A comparison of the model results using various fitting parameters can be seen in Figure 6.19.
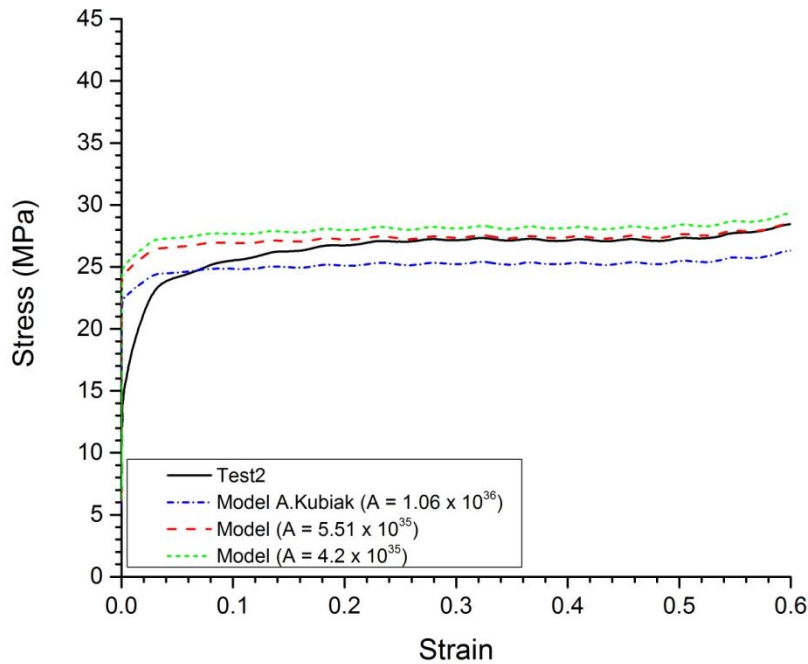
Figure 6.19 - Stress versus strain, smoothed data, and constitutive model fits using various values for A (test: homogenization of 24 h at 600°C, constant strain rate of 1 s^{-1} and deformation temperature of 500°C).

6.4.4   Effect of a Transient Strain Rate on the Flow Stress

The steady-state flow stress (flow stress) is used to describe the resistance of a material to plastic deformation at a given temperature and strain rate. In this section the effect of a transient strain rate on the flow stress is investigated along with the model's ability to capture the behavior.

The transitional strain rate tests are compared against the constant strain rate tests in Figure 6.20. The tests chosen for these figure were chosen as they are visually the average of each test set (the reader is referred to Figure 5.12 to Figure 5.16 in chapter 5.5). In general it can be seen that the transition strain rate tests have a resultant flow stress which is slightly greater than that of the 10 s^{-1} constant strain rate test. It can also be seen that there is no clear trend between the rate at which the strain rate is increased and the flow stress. The gradual test has the highest flow stress, followed by the rapid and the moderate.

The compression test results have shown that increasing the transition rate during deformation does not have a direct affect on the final steady-state flow stress. In Figure 6.20, one can see that the average flow stress for all of the tests with a final strain rate of 10 s^{-1} is constant, ranging from 36.9 to 39.2 MPa. This is a difference of less than 10%.
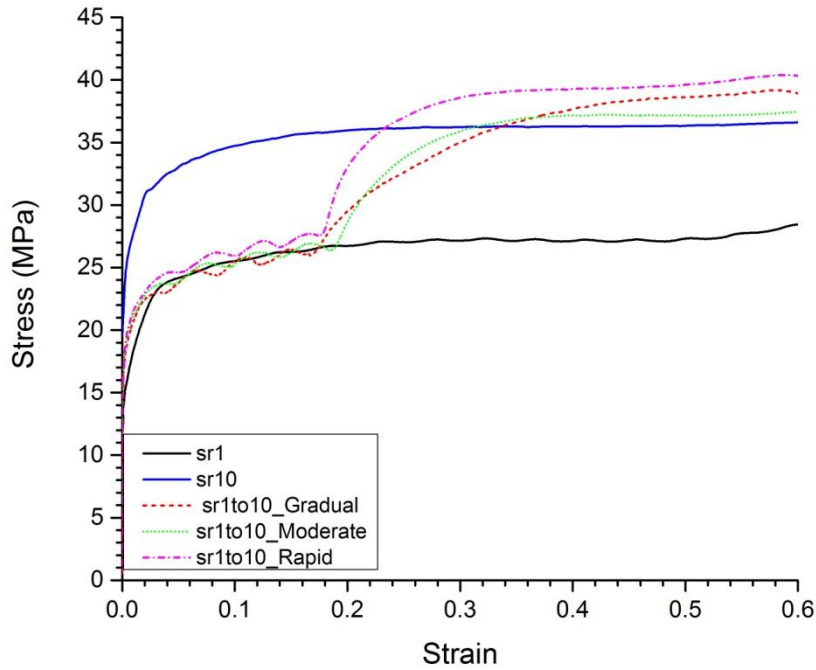
Figure 6.20 - Stress-strain curves for samples homogenized for 24 h at 600°C, deformed at 500°C at a constant strain rate ('sr1' = 1 s^{-1} and 'sr10' = 10 s^{-1}) or using a gradual (ε = 0.2 to 0.4), moderate (ε = 0.2 to 0.3)and rapid (ε = 0.2 to 0.25) strain rate transitions from 1 s^{-1} to 10 s^{-1}.
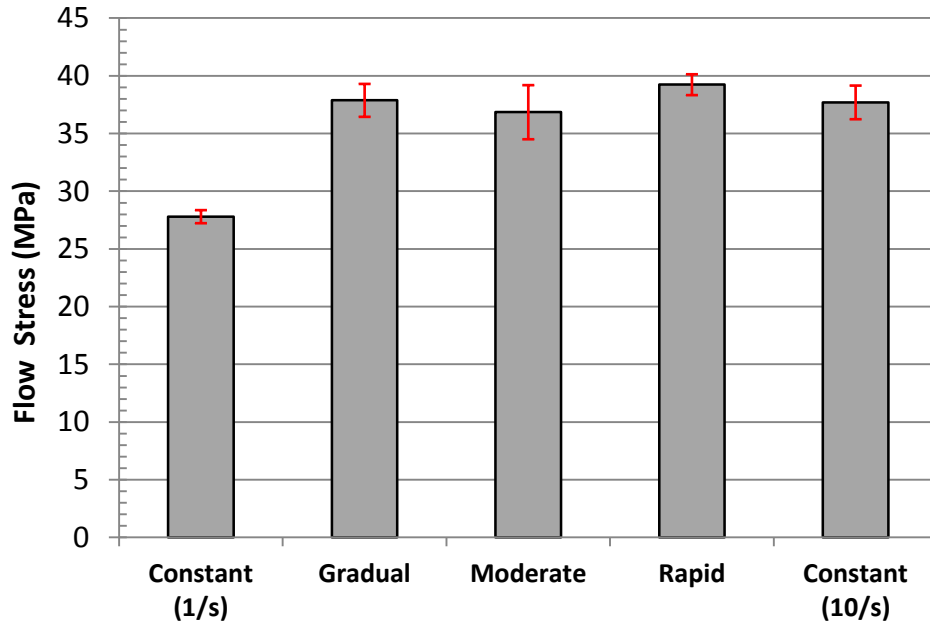
Figure 6.21 - Average steady-state flow stress values for hot compression samples homogenized for 24 h at 600°C, deformed at 500°C using constant strain rates and transitional strain rates (after the transition to a strain rate of 10 s^{-1}).

6.4.5 Applying the Constitutive Model

The Kocks and Chen constitutive model was applied to the high temperature compression experimental data using a pre-exponential constant of $A = 5.51 \times 10^{35}$ s^{-1} and a stress exponent of $n = 8.1$. The experimental temperatures and strain rates were used as inputs to the constitutive model. All of the data in this section is for samples homogenized for 24 h at 600°C and deformed at 500°C. The stress-strain graphs shown in this section display the extremes of the compression test results - meaning that the tests with the lowest flow stress and the highest flow stress are shown and compared to the model results. All of the flow stress model fit comparisons are made over a range of strain from 0.4 to 0.6. The model fit is only compared to the steady-state region of the stress-strain curves (i.e. $\varepsilon > 0.4$) as the model describes steady-state behavior and before a strain of 0.4, most tests are in a transient state.

Figure 6.22 shows the model and experimental stress-strain curves for samples deformed using a constant strain rate of 1 s^{-1}. The model fit to the experimental data is very good, reaching a flow stress of approximately 27 MPa. Figure 6.23 shows the same type of comparison except for a constant strain rate of 10 s^{-1}. The model fit for the flow stress here is not as good as for a strain rate of 1 s^{-1}, but still provides a good approximation. The experimental flow stress range here is between 36.4 MPa and 39.3 MPa, and the model flow stress range is from 34 MPa to 36 MPa.
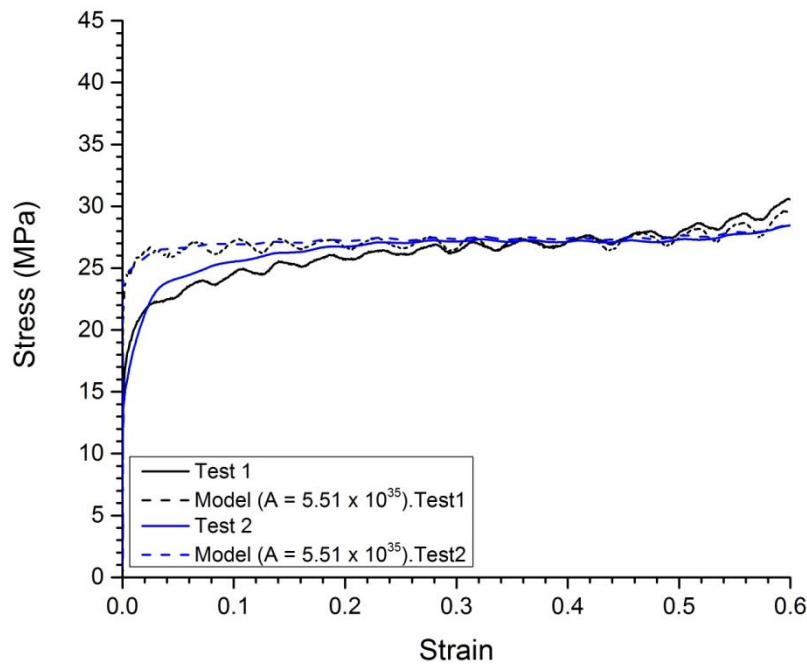
Figure 6.22 – Model comparison of stress-strain curves (using $A = 5.51 \times 10^{35}$ s^{-1} and n = 8.1) for samples homogenized for 24 h at 600°C, deformed at 500°C at a constant strain rate of 1 s^{-1}.
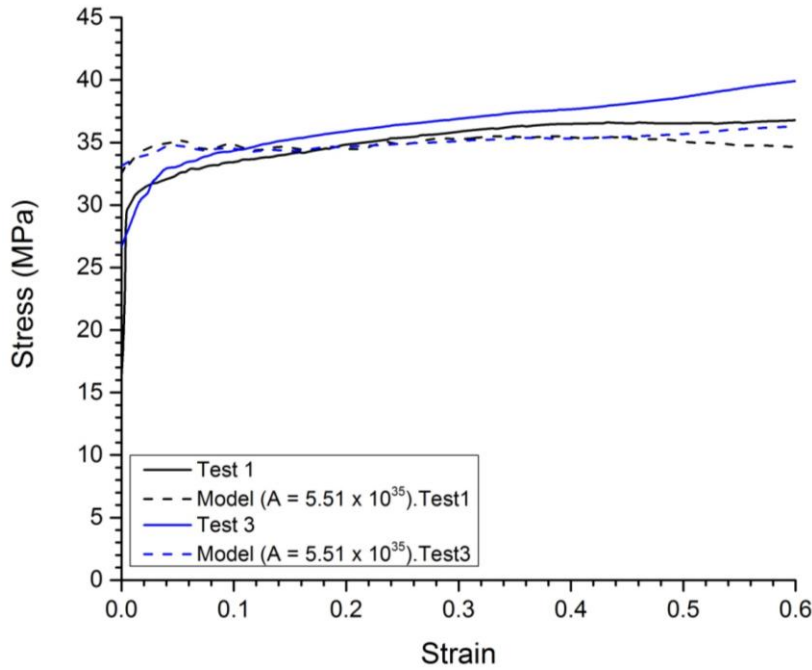
Figure 6.23 - Model comparison of stress-strain curves (using A = 5.51 x 10^{35} s^{-1} and n = 8.1) for samples homogenized for 24 h at 600°C, deformed at 500°C at a constant strain rate of 10 s^{-1}.

Figure 6.24 shows the first of 3 transient strain rate tests. This is the gradual transition (ε= 0.2 to 0.4) test from a strain rate of 1 s^{-1} to 10 s^{-1}. This test set had the largest spread in the flow stress, with a range of approximately 34.7 MPa to 40.3 MPa. The model shows a flow stress of approximately 35 MPa to 37 MPa. It should also be noted that the model under-estimates the flow stress of test 2 by approximately 5 MPa, and over-estimates the flow stress of test 3 by about 2 MPa. This effect is related to the strain rate history of the two tests (Figure 6.25). The model uses the experimental strain-rate as an input and therefore if the strain rate-strain history is different for the two samples the model predictions will be different. In this case the strain rate after a strain of 0.4 is always lower for test 2 than test 3. For example at a strain of 0.5 the strain rate for test 2 is 8.3 s^{-1} and 11 s^{-1} for test 3. The difference of approximately 3 s^{-1} (~30%) translates to a difference of ~13% in the experimental flow stress.
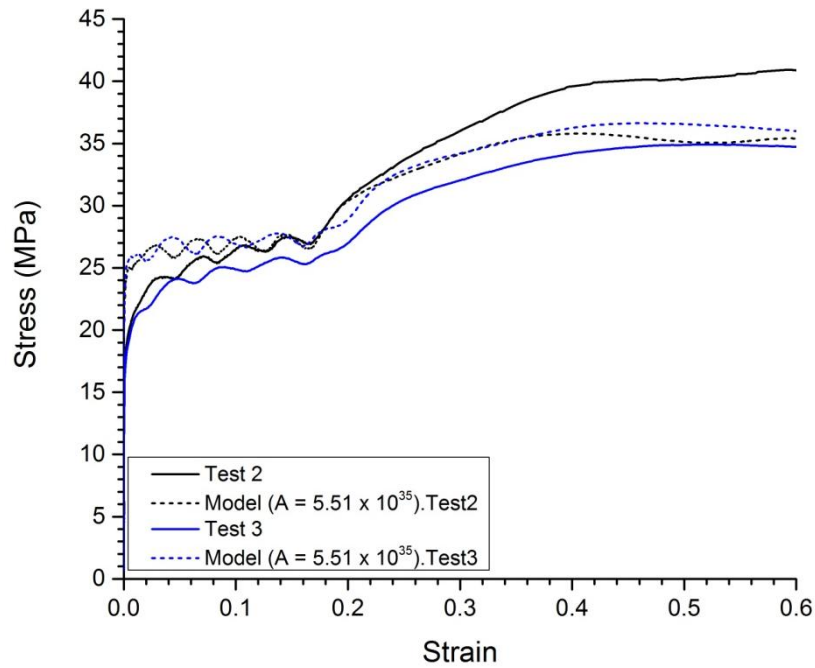
Figure 6.24 – Model comparison of stress-strain curves for (using A = 5.51 x 10^{35} s^{-1} and n = 8.1) samples homogenized for 24 h at 600°C, deformed at 500°C. Gradual (ε = 0.2 to 0.4) strain rate transition from 1 s^{-1} to 10 s^{-1}.
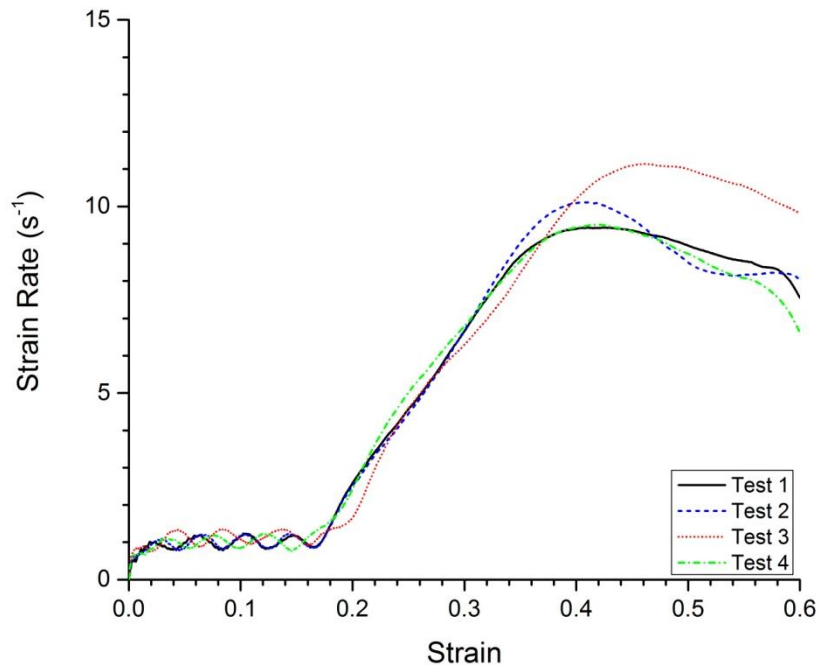
Figure 6.25 – Strain rate – strain curves for samples homogenized for 24 h at 600°C, deformed at 500°C. Gradual (ε = 0.2 to 0.4) strain rate transition from 1 s^{-1} to 10 s^{-1}.

Figure 6.26 shows the second set of transient strain rate tests. This is the moderate (ε = 0.2 to 0.3) strain rate transition test. The spread in the flow stress for this set of tests was lower as the strain rate-strain profiles for all of the tests were all very similar. For example the strain rates at a strain of 0.5 were 9.4 s^{-1} and 10.7 s^{-1} for test 1 and test 3, respectively. The experimental range in the flow stress is 35.8 MPa to 37.9 MPa, and the model flow stress for both tests is approximately 35 MPa. The two model strain rate curves collapse as strain increases as the strain rate for both of the tests approaches the same value starting at a strain of 0.5.

The third set of transient strain rate tests, rapid (ε = 0.2 to 0.25) transition, is shown in Figure 6.27. The range in the experimental flow stress here is 37.6 MPa to 40.4 MPa, and the model flow stress range is approximately 35 MPa to 36 MPa. The experimental strain-rate at a strain of 0.5 is 8.4 s^{-1} and 10.9 s^{-1} for test 2 and test 3, respectively. The difference in the strain rate and flow stress range for the rapid transition is comparable to what was seen for the moderate transition test. The model under-estimates the flow stress for test 2 and test 3 by approximately 5 MPa and 1.5 MPa, respectively.
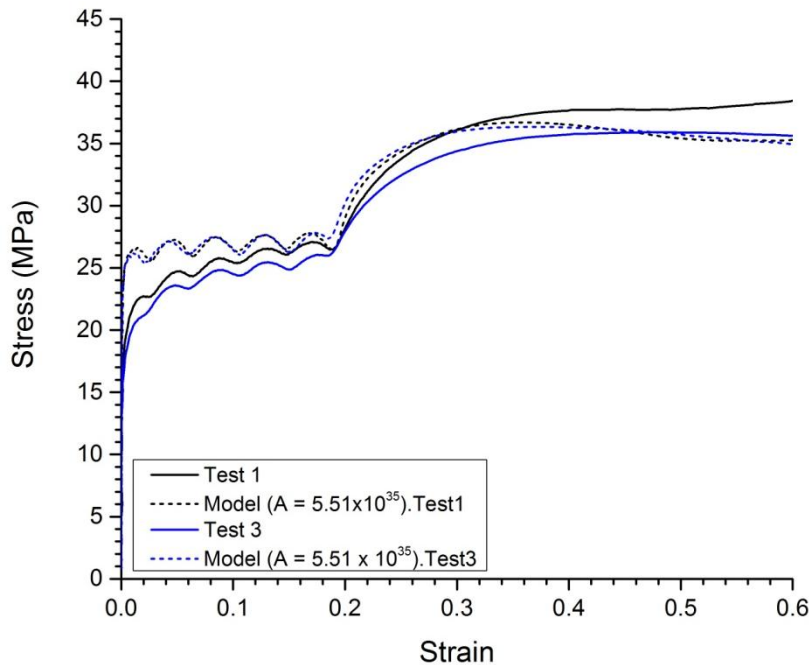
Figure 6.26 – Model comparison of stress-strain curves (using A = 5.51 x 10^{35} s^{-1} and n = 8.1) for samples homogenized for 24 h at 600°C, deformed at 500°C. Moderate (ε = 0.2 to 0.3) strain rate transition from 1 s^{-1} to 10 s^{-1}.
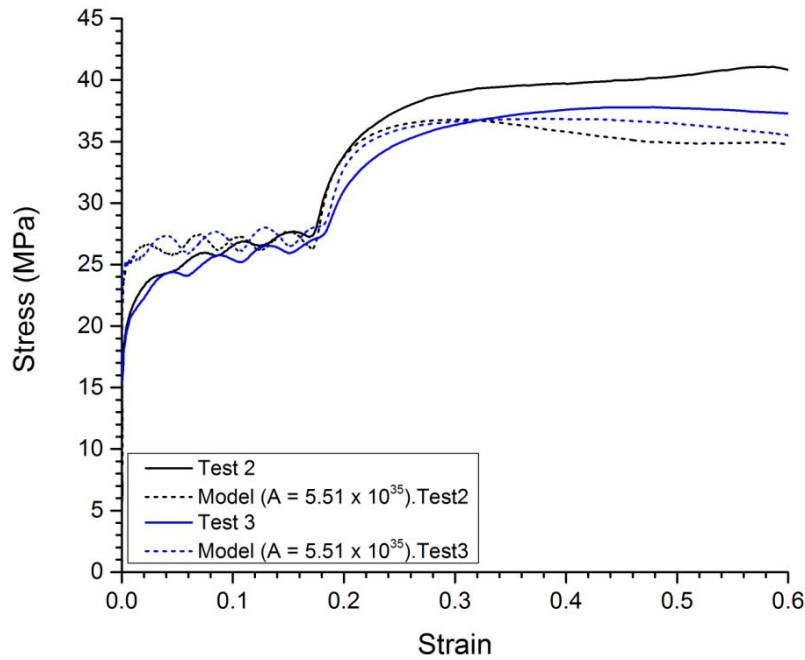
Figure 6.27 – Model comparison of Stress-strain curves (using A = 5.51 x 10^{35} s^{-1} and n = 8.1) for samples homogenized for 24 h at 600°C, deformed at 500°C. Rapid (ε = 0.2 to 0.25) strain rate transition from 1 s^{-1} to 10 s^{-1}.

Figure 6.28 shows the model's sensitivity to strain rate from 1 s^{-1} to 12 s^{-1}. The model is sensitive to small strain rates (< 2 s^{-1}). This sensitivity starts to level out at higher strain rate values. For example a strain rate of 8.0 s^{-1} gives a flow stress of 34.4 MPa, and a strain rate of 11.0 s^{-1} gives a flow stress of 35.8 MPa. An increase 37.5% (8 s^{-1} to 11 s^{-1}) in the strain rate results in an increase of 4.1% (34.4 MPa to 35.8 MPa) in the flow stress. This is a difference of 1.4 MPa which corresponds to a 0.2 MN difference in the extrusion force (the force required to extrude a material) [11] [8].
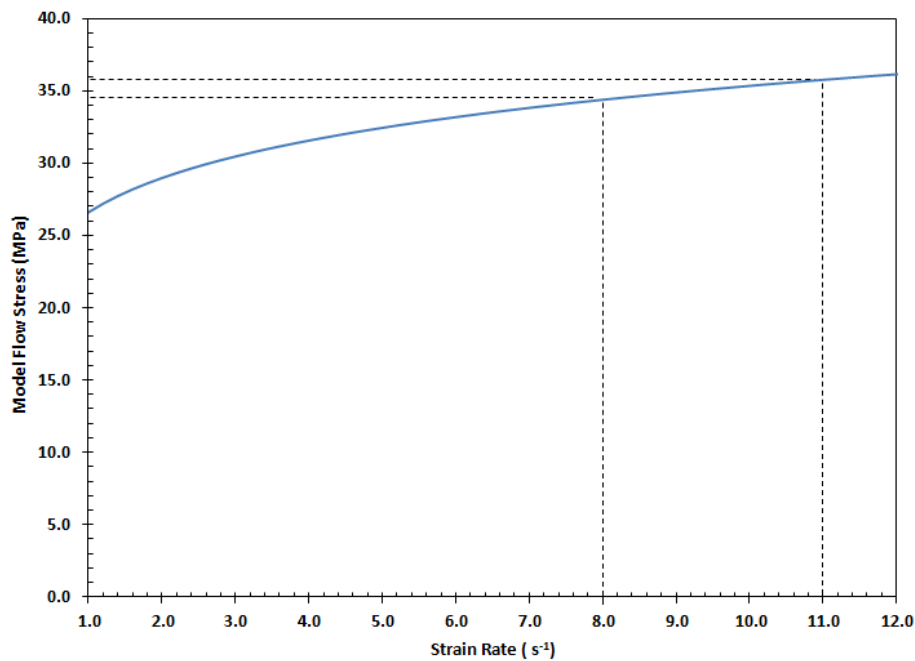
Figure 6.28 – The model flow stress sensitivity to strain rate for a deformation temperature of 500°C.

6.4.6 Summary

The Kocks and Chen constitutive model continues to provide a good approximation of AA3003 high temperature compression tests using a pre-exponential value of 5.51×10^{35} s^{-1} and strain exponent of 8.1. The model stress-strain curves did not follow the experimental curves exactly, but the model provides a reasonable approximation of the flow stress for all situations. The model did not fully capture the transient strain rate behavior because this is a steady-state model. The rapid transition test was of particular interest as this transition is closest to extrusion conditions.

Differences in the flow stress values between the experimental data and the model could be related to the strain rate data. The experimental stress-strain curves were conducted using the change in geometry of the test sample to calculate the true stress and strain, whereas the model used the experimental data such as the strain and time in order to determine the strain rate history of the test. Any errors introduced during the data smoothing could affect the calculated strain rate. Most of the difference in the flow stress values between the experiments and the model could be attributed to the strain rate history.

Caution should be taken when applying the constitutive model in situations in which a steady flow stress is not achieved, but instead some work hardening is present, as the model breaks down in regions in which there significant amounts of work hardening.

Chapter 6 discussed the results presented in chapter 5. The discussion begun with the through profile recrystallization behavior of the extrudates, and followed with a discussion on the progression of recrystallization through the profile. The effect of Zener pinning and stored energy of the system on the propensity for recrystallization was commented on. A geometric analysis on the deformation of the structure was conducted and these results were compared to the 3-D grain thickness measurements obtained from EBSD data. The effect of a transient strain rate on the steady-state flow stress of the material was also explored. Chapter 7 provides a summary of the main observations and results obtained during this investigation.

7 Summary and Future Work

Alloys such as AA3003 which are used for heat exchanger applications undergo a complex thermal processing route including casting, homogenization, extrusion and brazing. One of the main goals of such manufacturing operations is to be able to tailor the process parameters to obtain a specific microstructure profile which provides the desired material properties. This has led many aluminum producers to push for through process modeling. This investigation was part of a larger project to develop a process model for this application [3].

7.1 Summary

A systematic study of the effects of hot extrusion processing conditions on the microstructure of AA3003 was conducted. Billets were homogenized in order to obtain a range of dispersoid density, from low (24 h at 600°C) to high (8 h at 500°C). Extrusion ratios from 17:1 to 280:1 were explored using extrusion temperatures of 350°C, 400°C and 500°C and ram speeds of 2 mm/s, 8 mm/s and 32 mm/s. The extrusion trials were conducted at ARDC. The microstructure of the alloy was investigated in the as-cast, as-extruded and post-extrusion annealing states. The 3-D average grain size was determined in the as-cast state (~ 76 μm) using OM and in the as-extruded state (18.6 μm for 17:1 ER and 9.0 μm for 70:1 ER) using EBSD IPF maps.

As the dispersoid density of the material decreases the propensity for the material to recrystallize increases. All of the low dispersoid density (24 h at 600°C) samples were almost fully recrystallized. Those with a moderate dispersoid density (8 h at 550°C) were recrystallized

at low ram speeds and showed varying extents of recrystallization at a high ram speed. While those with high dispersoid density (8 h at 500°C) were all unrecrystallized, except from one sample extruded at 400°C using a ram speed of 32 mm/s and 70:1 ER. This sample, along with another, was used to investigate the constituent particle size, aspect ratio and distribution. These two samples showed unexpected recrystallization behavior -recrystallization first occurred at the boundary between the centre and ½ radius region. No link was found between the constituent particle size, distribution and density to the propensity for the region to recrystallize.

Post-extrusion annealing tests were conducted on unrecrystallized as-extruded samples in order to determine the stability of the structure against recrystallization. Post-extrusion annealing tests were conducted at temperatures of 500°C, 525°C and 550°C using holding temperatures of 1 min., 10 min., and 100 min. (except for at a temperature of 550°C). The post-extrusion annealing tests indicate that in most cases recrystallization occurs after a short heat treatment at high temperatures. Resistivity tests confirmed that there was minimal change in the chemistry of the system during annealing thereby indicating that any recrystallization that occurred is related to the stored energy of the system after deformation.

Grain size predictions using a simple mass balance approach provided good approximations of the average grain thickness at the centre of the extrudates. The predicted values were within 2% of those measured from EBSD misorientation profiles. This suggests that the technique used to characterize the through profile deformation, where large differences in grain thickness are predicted (provided recrystallization did not occur), is a viable option. The FEM model was also used to make predictions regarding the propensity for the centre of the extrudate to recrystallize, and was validated using the as-extruded and post-extrusion annealing samples. The stored energy of the system (including energy from grain boundaries) and the Zener pinning pressure were calculated. The model predictions and the experiments were in good accordance.

High temperature compression tests were conducted to study the constitutive behavior of the alloy, with emphasize on the effect of strain rate history on the steady-state flow stress. The experimental strain rate was applied to a physically-based constitutive model. The data exhibited a good correlation with the Kocks and Chen constitutive model (using $A = 5.51 \times 10^{35} \text{s}^{-1}$ and $n = 8.1$), but did not fully capture the behavior of the transient strain rate tests. This difference may be attributed to these samples being in a transient regime, instead of the steady-state regime that the model predicts. The ability to capture the transient region would be ideal as this would apply more closely to industrial extrusion conditions in which steady-state conditions are not often reached.

The main conclusions of this study are as follows:

- A fully recrystallized structure is obtained when a low dispersoid density (e.g. 24 h at 600°C) structure is extruded at high temperatures (350°C to 500°C).
    - A fine grained surface layer may be present after extrusion. It is unknown if these are from GDRX, and what the stability of this layer is.
    - The aspect ratio decreases with increasing ram speed, as does the magnitude of the grain size.

- An unrecrystallized structure is obtained when a high (e.g. 8 h at 500°C) to moderate (e.g. 8 h at 550°C) dispersoid density structure is extruded.
    - A fibrous structure (aspect ratio >10:1) is obtained through the cross section of the extrudate, with the thickness of the structure decreasing from the centre to the surface.
    - A lower extrusion ratio and ram speed result in a more stable structure (i.e. the propensity for the structure to recrystallize in further heat treatments is reduced). Although it should be noted that most conditions resulting in an unrecrystallized structure will recrystallize given more time at an elevated temperature.

- The exit temperature (a function of ram speed and extrusion temperature) was found to play a key role in whether or not a sample will recrystallize. Therefore the cooling of the sample is important in this system.

- The as-extruded grain size of unrecrystallized samples was determined using EBSD misorientation profiles and estimated using a simple mass balance. The grain size, if unrecrystallized, was found to be purely geometric and mainly dependent on the extrusion ratio.

- There was no clear relationship between the constituent particle distribution and density and the preferential nucleation sites for recrystallization.

- The Kocks and Chen constitutive model provides a good fit to the constant strain rate constitutive behavior of the alloy and an adequate fit to the transient strain rate behavior of the alloy. The inability of the constitutive model to fully capture the behavior may be due to the fact that a steady-state model is being used to describe a transient system.

7.2   Future Work

- Further characterization of the as-extruded grain structure, by EBSD, can be conducted by measuring the through thickness grain thickness of the samples using the transverse sections (this study used the longitudinal sections). This information may also be used to characterize the through thickness strain of the deformed structure provided recrystallization has not occurred.

- Post-extrusion annealing tests can be carried on to further test the stability of the unrecrystallized structures even after annealing for 10 min. at 550°C.

- The recrystallization kinetics of the system can be studied and modeled by conducting further post-extrusion annealing experiments. This will allow for further tailoring of the microstructure.

- Continue to study the effect of a strain rate history on the steady-state flow stress, especially using a shorter strain rate transition. This is highly relevant to industry as high temperature extrusion is an extreme process with large strain rate profiles through the cross-section of the extrudate.

References

[1] I. Polmear, Light Alloys: From Traditional Alloys to Nanocrystals (Fourth Edition), Butterworth-Heinemann, 2006.

[2] N. Parson and R. Ramanan, "Optimising AA3003 for Extrudability and Grain Size Control," *Extrusion Technology for Aluminum Profiles Foundation*, 2008.

[3] W. Poole, M. Wells and N. Parson, "A Through Process Model for AA3xxx Aluminum Alloys," in *Proceedings of the 13th Conference of Aluminum Alloys*, Pittsburgh, 2012.

[4] Y. Geng, "Microstructure Evolution During Extrusion of AA3xxx Aluminum Alloys," Master's Thesis, The University of British Columbia, Vancouver, 2011.

[5] A. Kubiak, "Effect of Homogenization on High Temperature Deformation Behaviour of AA3xxx Aluminum Alloys," Master's Thesis, The University of British Columbia, Vancouver, 2009.

[6] A. Dons, Y. Li, C. Marioara, A. Simensen, A. Johansen, L. Hakonsen, L. Arnberg and S. Benum, "Precipitation and dissolution of Mn-rich dispersoids during the heating of AA3xxx alloys," in *Aluminium*, 2004, pp. 583-587.

[7] M. Dehmas, E. Aeby-Gautier, P. Archambault and M. Serriere, "Interaction Between Eutectic Intermetallic Particles and Dispersoids in the 3003 Aluminum Alloy During Homogenization Treatments," *Metallurgical and Materials Transactions A,* vol. 44A, pp. 1059-1073, 2012.

[8] Y. Li and L. Arnberg, "Evolution of eutectic intermetallic particles in DC-cast AA3003 alloy during heating and homogenization," *Materials Science & Engineering: A,* vol. 347, no. 1-2, pp. 130-135, 2003.

[9] Y. Li and L. Arnberg, "Quantitative study on the precipitation behavior of dispersoids in DC-cast AA3003 alloy during heating and homogenization," *Acta Materialia,* vol. 51, no. 12, pp. 3415-3428, 2003.

[10] E. Mortsell, A. Muggerud, Y. Li and R. Holmestad, "Dispersoin Hardening Effect of Dispersoids in 3xxx Al Alloys with Varying Manganese and Silicon Contents," in *13th International Conference on Aluminum Alloys (ICAA13)*, Pittsburgh, 2012.

[11] A. Kubiak, W. Poole, M. Wells and N. Parson, "Effect of Homogenization Practice and Mn Content on the High Temperature Constitutive Behaviour of AA3xxx Aluminum Alloys," in *Proceedings of the 12th International Conference on Aluminum Alloys (ICAA12)*, Yokohama, 2010.

[12] Y. Mahmoodkhani, M. A. Wells, N. Parson, L. Grajales and W. J. Poole, "Modeling the Extrusion Process and the Microstructure Evolution for Hot Extrusion of AA3xxx Aluminum Alloys," in *ET'12: The Tenth International Aluminum Extrusion Technology Seminar & Exposition*, Miami, 2012.

[13] Q. Du, W. Poole, M. Wells and N. Parson, "Microstructural Modeling of the Homogenization Heat Treatment for AA3xxx Alloys," *J.Metals,* vol. 63, no. 7, pp. 35-39, 2011.

[14] Y. Mahmoodkhani, M. A. Wells, L. M. Grajales, W. Poole and N. Parson, "Modelling Grain Deformation during Extrusion of AA3003 using the Finite Element Method," in *13th International Conference on Aluminum Alloys (ICAA13)*, Pittsburgh, 2012.

[15] P. Babaghorbani, W. J. Poole, M. A. Wells and N. C. Parson, "The influence of initial microstructure on the recrystallization behaviour of cold-rolled AA3003," in *13th International Conference on Aluminum Alloys (ICAA13)*, Pittsburgh, 2012.

[16] R. Jorgensen and J. Macdonald, "Heat Exchanger Design," *Appliance Design,* pp. 20-23, November 2009.

[17] M. Ashby, H. Shercliff and D. Cebon, Materials: engineering, science, processing and design, Butterworth-Heinemann, 2007.

[18] H.-E. Ekstrom, "Al-Mn Brazing Sheet for Heat Exchangers," in *Virtual Fabrication of Aluminum Products: Microstructural Modeling in Industrial Aluminium Fabrication Processes*, Wiley-VCH, 2006, p. 20.

[19] J. G. Kaufman, Aluminum Alloys: Fatigue Data and the Effects of Temperature, Product Form, and Processing, ASM International, 2008.

[20] J. R. Davis, ASM Specialty handbook: Aluminum and Aluminum Alloys, ASM International, 1993.

[21] O. Ryen, O. Nijs, E. Sjolander, B. Holmedal, H.-e. Ekstrom and E. Nes, "Strengthening Mechanisms in Solid Solution Aluminum Alloys," *Metallurgical and Materials Transactions A,* vol. 37, pp. 1999-2006, 2006.

[22] J. E. Hatch, Aluminum: Properties and Physical Metallurgy, 2005: ASM International.

[23] D. G. Eskin, Physical Metallurgy of Direct Chill Casting of Aluminum Alloys, CRC Press, 2008.

[24] Q. Du, W. Poole, M. Wells and N. Parson, "Microstructure evolution during homogenization of AA3xxx alloys: Modeling and experimental results," *(Department of Materials Engineering; Vancouver: The University of British Columbia), unpublished manuscript,* 2013.

[25] E. Evangelista, "Chapter 14: Extrusion," in *Hot Deformation and Processing of Aluminum Alloys*, CRC Press, 2011, pp. 461-522.

[26] Y. Li, A. Muggerud, A. Olsen and T. Furu, "Precipitation of partially coherent [alpha]-Al(Mn,Fe)Si dispersoids and their strengthening effect in AA3003 alloy," *Acta Materialia,* vol. 60, no. 3, pp. 1004-1014, 2012.

[27] D. Alexander and A. Greer, "Particle break-up during heat treatment of 3000 series aluminum alloys," *Materials Science and Technology,* vol. 21, no. 8, pp. 955-960, 2005.

[28] D. Alexander and A. Greer, "Solid-state intermetallic phase transformations in 3xxx aluminum alloys," *Acta Materialia,* vol. 50, pp. 2571-2583, 2002.

[29] Y. Li, A. Hakonsen, D. Mortensen and T. Petterson, "Modelling the phase transformation from Al-6(Mn,Fe) to [alpha]-Al(Mn,Fe)Si phase during homogenization of AA3xxx alloys," *Materials Science forum,* vol. 519/521, pp. 297-302, 2006.

[30] A. L. Dons, "The Alstruc homogenization model for industrial aluminum alloys," *Journal of Light Metals,* vol. 1, pp. 133-149, 2001.

[31] C.-A. Gandin and A. Jacot, "Modeling of precipitate-free zone formed upon homogenization in a multi-component alloy," *Acta Materialia,* vol. 55, pp. 2539-2553, 2007.

[32] "Eddy-Current Inspection: Introduction," in *ASM Desk Editions: Metals Handbook*, ASM International, 1998.

[33] B. Raeisinia and W. Poole, "Electrical resistivity measurements: a sensitive tool for studying aluminum alloys".

[34] W. D. Callister, "Electrical Resistivity of Metals," in *Materials Science and Engineering an Introduction*, Wiley, 2007, pp. 674-676.

[35] Z. J. Lok, "Microchemistry in aluminium sheet production," (Ph.D. Thesis, Delft Univeristy of Technology), 2005.

[36] W. H. Van Geertruyden, H. M. Browne, W. Z. Misiolek and P. T. Wang, "Evolution of Surface Recrystallization during Indirect Extrusion of 6xxx Aluminum Alloys," *Metallurgical and Materials Transactions A,* vol. 36, no. 4, pp. 1049-1056, 2005.

[37] Y. Mahmoodkhani, Interviewee, *Strain rates during extrusion.* [Interview]. 2011.

[38] E. D. Sweet, S. K. Caraher, N. V. Danilova and X. Zhang, "Effects of Extrusion Parameters on Coarse Grain Surface Layer in 6xxx Series Extrusions," *Comalco Aluminum Limited,* pp. 115-126.

[39] H. Frost and M. Ashby, Deformation mechanism maps: the plasticity and creep of metals and ceramics, Pergamon Press, 1982.

[40] F. Humphreys and M. Hatherly, Recrystallization and Related Annealing Phenomena (second edition), Elsevier Ltd., 2004.

[41] H. Jazaeri and F. Humphreys, "The transition from discontinuous to continuous recrystallization in some aluminum alloys I - the deformed state," *Acta Materialia,* vol. 52, pp. 3239-3250, 2004.

[42] D. Hull and D. Bacon, "Strength of Crystalline Solids," in *Introduction to Dislocations (Fifth edition)*, Butterworth-Heinemann, 2011, pp. 205-248.

[43] H. McQueen, "Development of dynamic recrystallization theory," *Materials Science and Engineering A,* vol. 387, pp. 203-208, 2004.

[44] M. Kassner and S. Barrabes, "New developments in geometric dynamic recrystallization," *Materials Science and Engineering,* vol. 410, pp. 152-155, 2005.

[45] H. McQueen, O. Knustad, N. Ryum and J. Solberg, "Microstructural Evolution in Al Deformed to Strains of 60 at 400 C," *Scripta Metallurgica,* vol. 19, no. 1, pp. 73-78, 1985.

[46] G. Chen, G. Fu, H. Chen, W. Yan, C. Cheng and Z. Zou, "Research on hot deformation behavior of 3003 Al alloy prepared by different melt-treatment methods," *Applied Mechanics and Materials,* vol. 66, pp. 1611-1616, 2011.

[47] N. Sun, B. R. Patterson, J. P. Suni, H. Weiland and L. F. Allard, "Characterization of particle pinning potential," *Acta Materialia,* vol. 54, pp. 4091-4099, 2006.

[48] F. Humphreys, "Review: Grain and subgrain characterisation by electron backscatter diffraction," *Journal of Materials Science,* vol. 36, pp. 3833-3854, 2001.

[49] S. Wright and M. Nowell, "High-Speed EBSD," *Advanced Materials & Processes*, pp. 29-31, February 2008.

[50] A. S. Khan and H. Liu, "Variable strain rate sensitivity in an aluminum alloy: Response and constitutive modeling," *International Journal of Plasticity*, vol. 36, pp. 1-14, 2012.

[51] T. Sheppard and A. Jackson, "Constitutive equations for use in prediction of flow stress during extrusion of aluminium alloys," *Materials Science and Technology,* vol. 13, pp. 203-209, 1997.

[52] K. Tello, A. Gerlich and P. Mendez, "Constants for hot deformation constitutive models for recent experimental data," *Science and Technology of Welding and Joining,* vol. 15, no. 3, pp. 260-266, 2010.

[53] H. Rezaei Ashantiani, M. Parsa and H. Bisadi, "Constitutive equations for elevated temperature flow behavior of commercial purity aluminum," *Materials Science and Engineering A,* vol. 545, pp. 61-67, 2012.

[54] H. Hu, L. Zhen, L. Yang, W. Shao and B. Zhang, "Deformation behavior and microstructure evolution of 7050 aluminum alloy during high temperature deformation," *Materials Science and Engineering A,* vol. 488, pp. 64-71, 2008.

[55] W. Van Haaften, B. Magnin, W. Kool and L. Katgerman, "Constitutive Behavior of As-Cast AA1050, AA3104, and AA5185," *Metallurgical and Materials transactions A,* vol. 33A, pp. 1971-1980, 2002.

[56] U. Kocks and S. Chen, "Constitutive Laws for Deformation and Dynamic Recrystallization in Cubic Metals," in *7th Japan Institute of Metals International Symposium on Aspects of High Temperature Deformation and Fracture in Crystalline Materials*, Nagoya, 1993.

[57] S. Chen, M. Stout, U. Kocks, S. MacEwen and A. Beaudoin, "Constitutive Modeling of a 5182 Aluminum as a Function of Strain Rate and Temperature," 1998.

[58] J. Embury, W. Poole and E. Koken, "Some Views on the Influence of Strain Path on Recrystallization," *Scripta Metallurgica et Materialia,* vol. 27, pp. 1465-1470, 1992.

[59] J. Klepaczko, "Thermally Activated Flow and Strain Rate History Effects for some Polycrystalline F.C.C. Metals," *Materials Science and Engineering,* vol. 18, pp. 121-135, 1975.

[60] T. Furu, H. Shercliff, G. Baxter and C. Sellars, "The Influence of Transient Deformation Conditions on Recrystallization During Thermomechanical Processing of an Al-1% Mg Alloy," *Acta Metallurgica Inc.,* vol. 47, no. 8, pp. 2377-2389, 1999.

[61] "Sigmatest 2.069 Device Sheet," Foerster.

[62] A. Giumelli, M. Militzer and E. Hawbolt, "Analysis of the Austenite Grain Size Distribution in Plain Carbon Steels," *ISIJ International,* vol. 39, no. 3, pp. 271-280, 1999.

[63] N. Parson, Interviewee, [Interview]. 31 August 2012.

[64] Y. Mahmoodkhani, M. A. Wells, N. Parson, Y. Geng and W. J. Poole, "Mathematical Modelling of the Extrusion of AA3xxx Aluminum Alloys," in *Proceedings of the 12th International Conference on Aluminum Alloys (ICAA12)*, Yokohama, 2010.

[65] Q. Du, Interviewee, *Dispersoid data for various homogenization treatments.* [Interview]. 20 March 2013.

[66] E. Nes, N. Ryum and O. Hunderi, "On the Zener Drag," *Acta Metall.,* vol. 33, no. 1, pp. 11-22, 1985.

[67] Y. Mahmoodkhani and M. Wells, Interviewees, *Recrystallization Model.* [Interview]. 3 April 2013.

[68] Y. Mahmoodkhani, M. A. Wells, L. M. Grajales, W. Poole and N. Parson, "Presentation: Modelling Grain Deformation during Extrusion of AA3003 using the Finite Element Method," in *13th International Conference on Aluminum Alloys (ICAA13)*, June 7, 2012.

[69] Q. Du and A. Jacot, "A two-dimensional microsegregation model for the description of microstructure formation during solidification in multicomponent alloys: Formulation and behaviour of the model," *Acta Materialia*, vol. 53, pp. 3479-3493, 2005.

[70] "Vision PE & Vision Lite 6.0 User Guide," CLEMEX Technologies Inc., 2009, pp. 40-41.

[71] S. K. Chaudhury, "Homogenization," in *ASM Handbook: Casting*, ASM International, 2008, pp. 402-403.

[72] J. Mackenzie, "Second Paper on Statistics Associated with the Random Disorientation of Cubes," 1958.

[73] T. Pettersen, B. Holmedal and E. Nes, "Microstructure Development during Hot Deformation of Aluminum to Large Strains," *Metallurgical and Materials Transactions A*, vol. 34A, pp. 2737-2744, 2003.

Appendices

Appendix A

A.1 Summary of Compression Test Results

This appendix summarizes the high temperature compression test results for the various sets of conditions. All tests were performed as described in chapter 4.3. The extrusion temperature was 500°C, and the homogenization treatment was 24 h at 600°C. Tests were performed using a strain rate of 1 s^{-1}, 10 s^{-1} and transition tests from 1 s^{-1} to 10 s^{-1} using a range of strain transitions. Data such as the temperature and the measured strain rate were collected at a strain of 0.5 for all tests. This data can be found in Table A. 1 to Table A. 5. The yield strength was characterized by the 0.2 percent offset method.

Table A. 1 – High temperature compression results summary for a constant strain rate of 1 s⁻¹.

Test ID	Strain rate (s⁻¹)	Transition	Temp. (°C)	Measured strain rate (s⁻¹)	ρ_{before} (nΩm)	ρ_{after} (nΩm)	$\Delta\rho$ (nΩm)	Change (%)	σ_{flow} (MPa)	σ_y (MPa)
Test 1	1	--	489	1.0	46.7	45.9	-0.8	-2	28.2	17.0
Test 2	1	--	493	0.8	47.5	46.1	-1.4	-3	27.4	15.0
Average	--	--	*491*	*0.9*	*47.1*	*46.0*	*-1.1*	*-3*	*27.8*	*16.0*
Standard deviation	--	--	*2.8*	*0.1*	*0.57*	*0.14*	*0.42*	*1*	*0.57*	*1.41*

Table A. 2 – High temperature compression results summary for a constant strain rate of 10 s⁻¹.

Test ID	Strain Rate (s⁻¹)	Transition	Temp. (°C)	Measured Strain Rate (s⁻¹)	ρ_{before} (nΩm)	ρ_{after} (nΩm)	$\Delta\rho$ (nΩm)	Change (%)	σ_{flow} (MPa)	σ_y (MPa)
Test 1	10	--	504	11.6	46.7	46.0	-0.7	-1	36.6	14.0
Test 2	10	--	505	10.2	47.1	46.1	-1.1	-2	36.4	15.6
Test 3	10	--	505	12.8	47.2	46.0	-1.2	-3	38.5	17.1
Average	--	--	*505*	*11.5*	*47.0*	*46.0*	*-1.0*	*-2*	*37.2*	*15.6*
Standard deviation	--	--	*0.6*	*1.3*	*0.26*	*0.06*	*0.26*	*1*	*1.16*	*1.55*

Table A. 3 – High temperature compression results summary for a gradual transition (0.2 to 0.4 strain).

Test ID	Strain Rate (s⁻¹)	Transition	Temp. (°C)	Measured Strain Rate (s⁻¹)	ρ_{before} (nΩm)	ρ_{after} (nΩm)	$\Delta\rho$ (nΩm)	Change (%)	σ_{flow} (MPa)	σ_y (MPa)
Test 1	1 to 10	0.2 to 0.4	497	8.3	47.0	45.8	-1.2	-3	38.6	17.7
Test 2	1 to 10	0.2 to 0.4	497	8.9	47.5	46.1	-1.4	-3	40.3	18.8
Test 3	1 to 10	0.2 to 0.4	496	11	47.0	46.1	-0.9	-2	34.7	18.1
Test 4	1 to 10	0.2 to 0.4	497	8.7	47.6	46.1	-1.5	-3	37.9	17.9
Average	--	--	*497*	*9.2*	*47.3*	*46.0*	*-1.3*	*-3*	*37.9*	*18.1*
Standard deviation	--	--	*0.5*	*1.2*	*0.32*	*0.15*	*0.26*	*1*	*2.34*	*0.45*

Table A. 4 - High temperature compression results summary for a moderate transition (0.2 to 0.3 strain).

Test ID	Strain Rate (s⁻¹)	Transition	Temp. (°C)	Measured Strain Rate (s⁻¹)	ρ_{before} (nΩm)	ρ_{after} (nΩm)	$\Delta\rho$ (nΩm)	Change (%)	σ_{flow} (MPa)	σ_y (MPa)
Test 1	1 to 10	0.2 to 0.3	498	9.4	47.1	46.1	-1.0	-2	37.9	18.1
Test 2	1 to 10	0.2 to 0.3	496	9.8	47.6	46.1	-1.5	-3	37.2	18.3
Test 3	1 to 10	0.2 to 0.3	500	10.7	47.3	45.9	-1.4	-3	35.8	16.6
Test 4	1 to 10	0.2 to 0.3	497	10.5	47.5	46.1	-1.4	-3	36.5	16.9
Average	--	--	*498*	*10.1*	*47.4*	*46.1*	*-1.3*	*-3*	*36.9*	*17.5*
Standard deviation	--	--	*1.7*	*0.6*	*0.22*	*0.10*	*0.22*	*1*	*0.90*	*0.85*

Table A. 5 - High temperature compression results summary for a rapid transition (0.2 to 0.25 strain).

Test ID	Strain Rate (s⁻¹)	Transition	Temp. (°C)	Measured Strain Rate (s⁻¹)	ρ_{before} (nΩm)	ρ_{after} (nΩm)	$\Delta\rho$ (nΩm)	Change (%)	σ_{flow} (MPa)	σ_y (MPa)
Test 1	1 to 10	0.2 to 0.25	497	8.4	47.1	46.3	-0.8	-2	39.7	18.5
Test 2	1 to 10	0.2 to 0.25	498	8.4	47.4	46.0	-1.4	-3	40.4	18.7
Test 3	1 to 10	0.2 to 0.25	496	10.9	47.2	46.0	-1.2	-3	37.6	18.4
Average	--	--	*497*	*9.2*	*47.2*	*46.1*	*-1.1*	*-3*	*39.2*	*18.5*
Standard deviation	--	--	*1.0*	*1.4*	*0.15*	*0.17*	*0.31*	*1*	*1.46*	*0.15*

Appendix B

B.1 As-Cast Grain Size Analysis: Clemex Routine

The following is an example of the routine used for the as-cast grain size analysis. This routine is based from a Clemex routine [70]. Figure B. 1 shows screen shots of some of the routine steps described below.

Step	Action\\ description
001	Gray Threshold \\Selects the grain boundaries from the background. BLP1 range 0..223 \\The particle color range is assigned to "blue" (BLP1)
002	Trap 15x15, BPL1 -> None \\Selects any items less than 15x15 pixels (i.e. approximately 1.5 μm by 1.5 μm) and moves them to an unspecified plane "NONE"
003	Invert BPL1 => BPL2 \\BPL1 is inverted onto BPL2. This detects the grains in BPL2.
004	Zone CIRC to End => BPL2
005	Square Grid 1x1 => BPL3 \\A frame is generated in BP3. Overall Grid Dimensions 2007 x 1498 pixels 1062 x 793 μm
006	Transfer (BPL2 SEL BPL3) => None \\The features in BPL2 which are intercepted by BP3 are cleared. This eliminates incomplete particles.
007	Object Measures (BPL2) -> OBJM1 \\The ASTM grain size measurement is performed on individual grains. Aspect Ratio Circular Diameter Spherical Diameter Area ASTM E112-96

End of Field
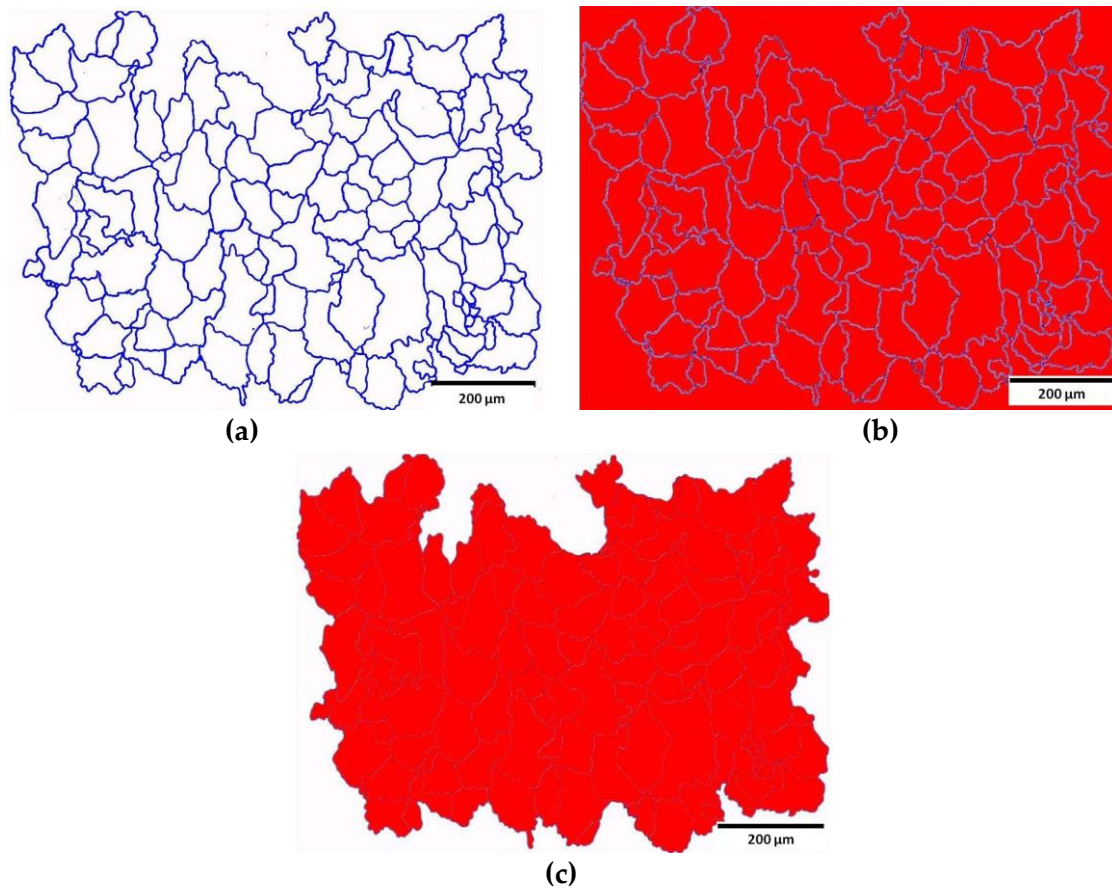
Figure B. 1 -- Location 3 screen shots of the grain size routine steps: (a) step 002, (b) step 004, and (c) step 007.

B.2 As-Cast Grain Size Analysis: Clemex Routine Parameter Sensitivity

The trap size used in the routine was 15 x 15 pixels, which corresponds approximately to 1.5 x 1.5 μm, this resulted in a lot of dust, pen marks and dents in the scanned transparency images being counted as grains. In order to eliminate these erroneous points any points which were equivalent to or less than the size of a pen point, approximately 5.5 μm, were sorted out of the grain distribution data. Figure B. 2 shows and example of the erroneous data introduced during the tracing and scanning steps of the grain boundaries. By accounting for this erroneous data and eliminating it, the overall distribution was adjusted as shown in Figure B. 3. The overall distribution is not affected.
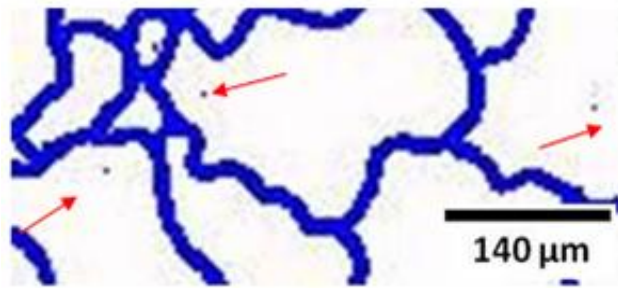
Figure B. 2 - Example of points being introduced during the tracing and scanning steps, of the grain size measurement analysis.
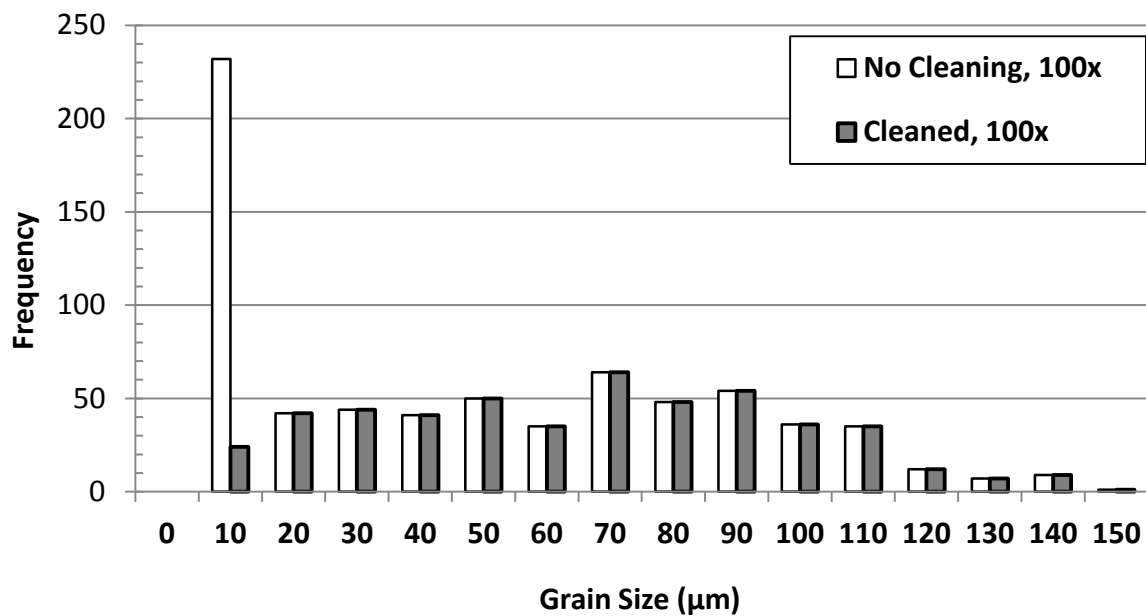
Figure B. 3 - Grain size distribution for location 1 (i.e. Centre) before and after data post-processing.

B.3 Constituent Particle Measurements: Clemex Routine

This section of the appendix will discuss specifics of the procedure used to obtain a quantitative analysis of the constituent particles such as: size, aspect ratio area fraction and number density using the Clemex software and routine. First the samples were prepared as described in chapter 4.5.6. Figure B. 4 shows a micrograph of the centre of the 70:1 sample homogenized for 8 h at 550°C, extruded using a ram speed of 8 mm/s at a temperature of 350°C at 500x magnification and the corresponding transparency with the traced constituent particles that was used for further analysis.

(a)   **(b)**

Figure B. 4 - (a) 500x micrograph of the centre of the 70:1 sample homogenized for 8 h at 550°C, extruded using a ram speed of 8 mm/s at a temperature of 350°C, etched using 0.5% HF for 60 s, (b) transparency tracing of the constituent particles (dark regions) of (a).

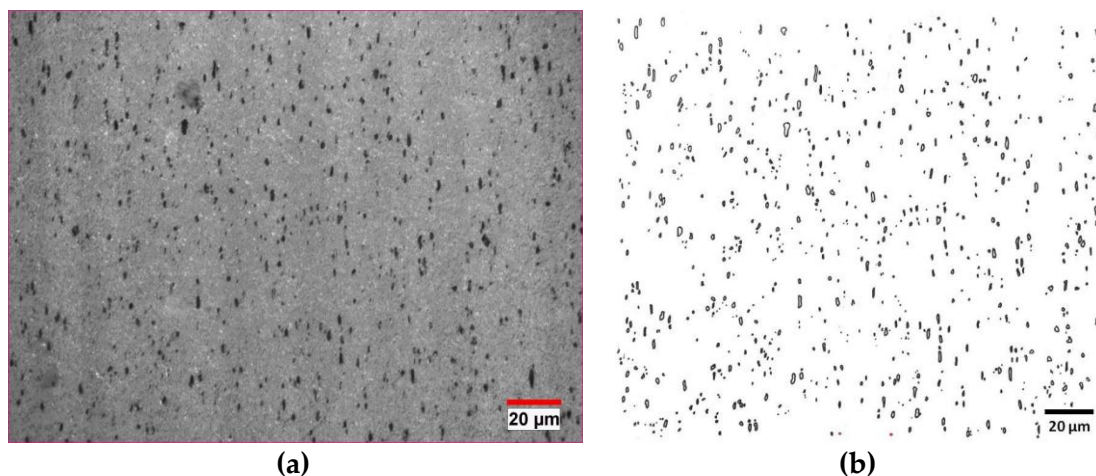Figure B. 4(b) was scanned and imported into the Clemex software. The image was calibrated to the corresponding magnification (at a magnification of 500x the calibration is approximately 0.1 µm/pixel) and the following routine, shown below, was run. Subroutines that come built in to the Clemex software were used for determining the area percent, count and aspect ratio. Figure B. 5 shows screen shots of some of the routine steps.

Step	Action\\ description
001	Gray Threshold \\Selects the black particles from the white background
	BLP1 range 0..128 \\The particle color range is assigned to "blue" (BLP1)
	BPL2 range 128..255 \\The background color range is assigned to "red" (BLP2)
002	Trap 7x7, BPL1 -> None \\Selects any items less than 7x7 pixels (i.e. approximately 0.7 µm by 0.7 µm) and moves them to an unspecified plane "NONE"
003	Fill => BPL1 \\Fills the particles
	Fill border objects: YES \\Fills in the highlighted items
004	Relative Measures -> RELM1 \\Calculates the area percentage of the phases (i.e., BPL1, BPL2) with respect to the total area covered by the field of analysis
	Area Percent
	BPL1
	BPL2
	Relative to Field
005	Field Measures (BPL1) -> FLDM2 \\Counts the number of separate filled items
	Count

006   Object Measures (BPL1) -> OBJM3 \\Measures the aspect ratio of the filled items, and is defined as the length of the longest feret (length) over the length of the shortest feret (width)

Aspect Ratio

End of Field

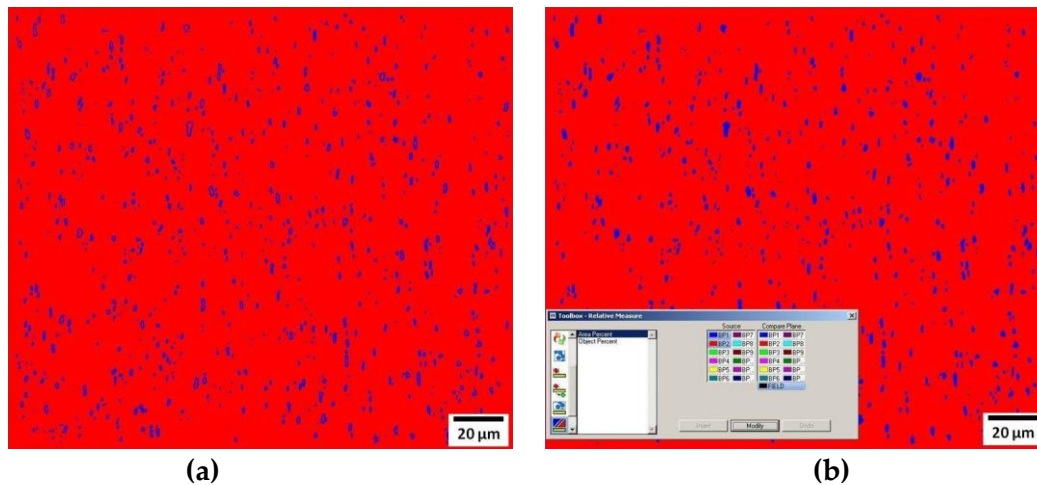(a)   (b)

Figure B. 5 - Screen shots of the constituent particle routine steps for 70:1 sample homogenized for 8 h at 550°C, extruded using a ram speed of 8 mm/s at a temperature of 350°C at the centre: (a) step 001, and (b) step 004.

B.4 Constituent Particle Measurements: Clemex Routine Parameter Sensitivity

In step 002 of the Clemex routine, shown in the previous section, one defines a minimum particle size. The influence of this defined space, 7x7 pixels, on the final analysis was investigated. The same routine was run with a pixel limit of 2x2 (i.e. approximately 0.2 μm by 0.2 μm) and the results were compared to that of the previous analysis. By looking at Table B. 1 to B. 3, one can see that there was no change in the trends for the mean aspect ratio, count and area fraction (all values determined by the routine), and only a small change in the values (<10%). The largest difference was found in the number of points counted (Table B.2). This is to be expected as by using a lower pixel limit more erroneous points such as dust or scan defects may have been introduced into the data set. The difference in the aspect ratio was minimal with a change of less than 2.5% for all location (Table B. 1). The Fv/r ratio (Table B.3), which is the ratio between the average equivalent area for a particle over the average circular radius, saw a change of approximately 20%. The values reported in chapter 5.3.4 use a defined space of 7x7 pixels.

Table B. 1 - Aspect ratio sensitivity.

Trap limit (pixels)	7 x 7	2 x 2	% Difference
Centre	2.11	2.06	-2.4
1/2 radius	1.90	1.88	-1.1
Sub-surface	1.93	1.90	-1.6
Surface	1.79	1.79	0.0

Table B. 2 - Count sensitivity.

Trap limit, pixels	7 x 7	2 x 2	% Difference
Centre	631	679	7.1
1/2 radius	608	644	5.6
Sub-surface	743	808	8.0
Surface	685	727	5.8

Table B. 3 - Fv/r ratio sensitivity.

Trap limit (pixels)	7 x 7	2 x 2	% Difference
Centre	2.4	2.0	-20
1/2 radius	2.6	2.1	-21
Sub-surface	2.3	1.9	-19
Surface	2.4	1.9	-19

Appendix C

C.1 EBSD Data Clean-Up: Procedure Details

This appendix shows the details of the cleaning procedure used for cleaning the EBSD data to produced IPF maps.

Run information:

Operator: Administrator
Calibration: 0.615114 0.662408 0.692949
Working Distance: 11.000000

Number of points: 904401
Number of good points: 904400

Dimensions:
X Min: 0.00 microns
X Max: 950.00 microns
Y Min: 0.00 microns
Y Max: 950.00 microns
Step: 1.00 microns

Average Confidence Index: 0.34
Average Image Quality: 852.07
Average Fit [degrees]: 2.13

Phases:
Aluminum

Clean-up procedure:

Rotation (RD 0.0°, TD 0.0°, ND 90.0°)
Grain CI standardization:
      Min. grain size of: 2 pixels
      Grain tolerance angle: 2
      Single iteration
Filter
      CI index > 0.1
Grain dilation
      Same settings as Grain CI standardization
      Grain removal amount: 168137/904401 = 18.6%
Grain boundaries

High angle: 15 to 180 degrees
CI index > 0.1
Maps profile vector
Show pt to pt misorientation

C.2 Grain Thickness Measurements from EBSD Maps: Sensitivity Analysis

The EBSD data that was post-processed in excel was processed using an equivalent minimum grain size to that of the one used when cleaning the IPF maps. For example for a 1 μm step-size used during the run, the minimum grain size during "cleaning" was set to 2 pixels (i.e. a minimum grain size of 2 μm was utilized). For the excel post-processing a minimum grain thickness of 2 μm was used. By using this minimum grain thickness boundary condition the average grain thickness for a 70:1 ER sample homogenized for 8 h at 500°C, extruded at 500°C using a ram speed of 8 mm/s is 7.3 μm. If the data is analyzed, in Excel, such that the minimum grain thickness is 1 μm and 3 μm the average grain thicknesses are 6.9 μm and 7.9 μm, respectively.

If during the clean-up step of the EBSD data processing the minimum grain size had been set to 3 pixels, rather than 2 pixels, the resulting average grain thickness would be slightly different. The average grain thicknesses would be 7.3, 7.6 and 8.2 μm for a respective Excel post-data processing of minimum grain size of 1, 2 and 3 μm. A summary of the sensitivity analysis of the 2-D grain thickness for the 70:1 ER sample homogenized for 8 h at 500°C, extruded at 500°C using a ram speed of 8 mm/s can be seen in Table C. 1.

Table C. 1 – 2-D grain thickness sensitivity analysis for a 70:1 ER sample homogenized for 8 h at 500°C, extruded at 500°C using a ram speed of 8 mm/s.

Excel post-processing	1 μm	2 μm	3 μm	*Standard deviation*
EBSD Clean-up				
2 μm	6.9	7.3	7.9	*0.50*
3 μm	7.3	7.6	8.2	*0.46*
Standard deviation	*0.28*	*0.21*	*0.21*	